Finite Element Analysis of Compact Reinforced Composite substructure to a bucket foundation and offshore windturbine

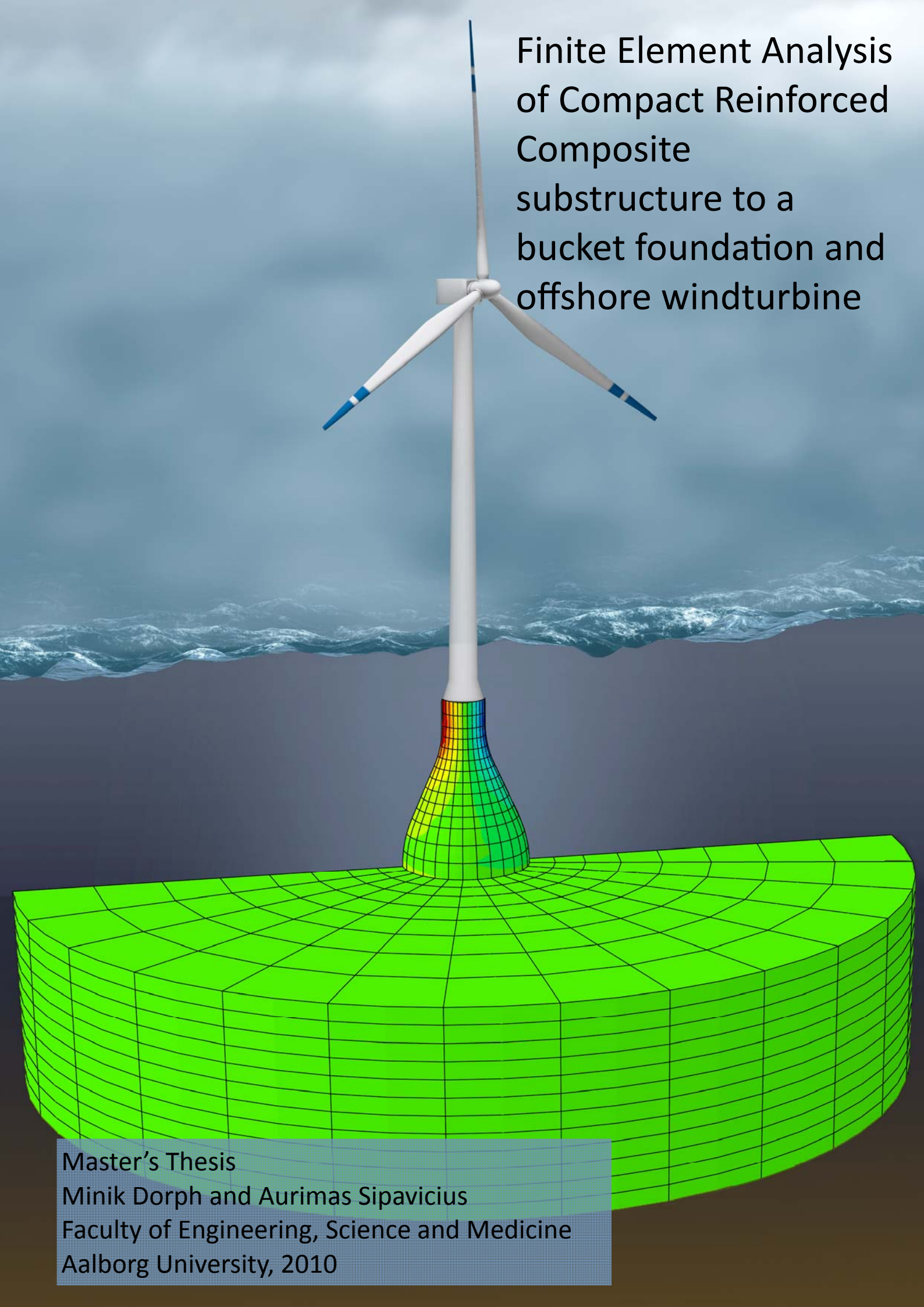

Master's Thesis

Minik Dorph and Aurimas Sipavicius
Faculty of Engineering, Science and Medicine
Aalborg University, 2010

Aalborg University
Faculty of Engineering, Science and Medicine
School of Engineering

Title:

Finite Element Analysis of Compact Reinforced Composite substructure to a bucket foundation and offshore windturbine

Theme:

Design and analysis of advanced/special structures

Master's thesis:

01.02.2010 - 10.06.2010

Author:

Minik Dorph
Aurimas Sipavicius

Supervisor:

Lars Andersen

Number printed : 4

Number of pages: 139

CD enclosed: 4

PREFACE

This master's thesis is a documentation for the Civil Engineering and is made at Aalborg University the Faculty of Engineering, Science and Medicine, the School of Engineering.

The theme of the 4rd semester candidate programme is *Design and analysis of advanced/special structures*. The title of the project is *Finite Element Analysis of Compact Reinforced Composite substructure to a bucket foundation and offshore windturbine* and prepared in the period of February 1st 2010 - June 11th 2010.

A CD with .cae-files for Finite Flement models and this thesis in pdf-format is enclosed.

The reference system that are used in the report is written as [*no., Page number*] and in the bibliography, at the end of the report, the whole information for the references can be seen.

Minik Dorph

Aurimas Sipavicius

SUMMARY

In nowadays the offshore windturbines with a bucket foundation are widely used all over the world, usually they are all made of steel. A steel material is used for the transition piece between the bucket foundation and the tower, welded brackets are used to connect them. The two main problems for this kind of connection is fatigue at the welded zone and corrosion.

The aim of the project is to model a substructure for the offshore wind turbine with a bucket foundation utilizing FEA and The material Compact Reinforced Composite will be applied. The substructure will be made as a shell structure. Therefore instability as well as material failure has to be examined. Since there are no known analytical solution of prebuckling load to the substructure, a verifacation study has been performed for other types of shell structures with known analytical solution for prebuckling load. As a verification study, the buckling load of a dome, a cylinder and a bucket foundation are found by an analytical approach. These results has been compared with the results of FEA to check the validity of the computational model before it is applied for the analysis of the substructure. The verification study showed that a good agreement with the analytical result and FEA result has been obtained. Since the focus is on the structural response of the substructure the tower is disregarded in FEA. Because the substructure is axisymmetric, only half of the substructure is modeled with the soil and thereby the computational time is reduced. Hence, a buckling analysis of the substructure is carried out by means of FEA, and a nonlinear material model is implemented. The nonlinear material that is applied is Concrete Damaged Plasticity. The hydraulic pressure that were applied to the substructure is based on linear wave theory. There was done an assumption of the drag pressure distribution and the limit of this assumption was that the hydraulic pressure distribution could not be checked when the wave surface was in the trough. Instead the hydraulic pressure distribution was checked when the wave surface was on the crest. A wind load is applied as well. The substructure will is shaped as a bottle neck. In the preliminary design 5 different shapes of the substructures analysis are performed regarding the load-carrying capacity when elastic material is used. In the preliminary design it was discovered that the hydraulic pressure distribution had a minimum impact to the section forces and to the instability, whereas the wind load was critical to the substructure. Two substructures with a single and two layers of rebar reinforcements has been proposed. From the linearized prebuckling analysis it was discovered that there was no buckling risk of the proposed substructures and that the material failure was the design criterion. Since shell structures are never geometrical perfect a linearized prebuckling mode was utilized as a geometrical imperfection for the substructures. A nonlinear analysis was performed for the substructures with geometrical imperfection. The analysis showed that the substructures were not sensitive for geometric imperfection.

The outcome of the report is that it is believed that it is possible to make a substructure to the offshore windturbine when utilizing Compact Reinforced Composite.

RESUME

I dag er havbaseret vindturbiner med en bøttefundament almindeligt anvendt over hele verden, som regel er de alle lavet af stål. En stål materiale er anvendt til overgangsstykke mellem bøttefundament og tårnet, disse samles med svejsede beslag. De to vigtigste problemer for den samlingsform er risiko for udmattelse i den svejsede zone samt korrosion.

Formålet med dette projekt er at modellere en overgangstykke for en havbaserede vindturbine med en bøttefundament v.h.a. FEA hvor Compact Reinforced Composite anvendes. Overgangstykket vil blive lavet som en skal-konstruktion. Derfor så skal ustabilitet samt materiale brud undersøges. Da der er ingen kendte analytiske løsning til beregning af foldning for overgangstykket, så er der udført efterprøvnings undersøgelse for andre type skal-konstruktioner med kendte analytiske løsninger. Til dette formål er der undersøgt en kuppel, en cylinder og en bøttefundament til at finde den kritiske foldning v.h.a. analytiske løsninger. Disse resultater er sidenhen blivet sammenlignet med resultater baseret på FEA for at kontrollere gyldigheden af de beregningsmæssige model, før det anvendes til analyse af overgangstykket. Efterprøvnings undersøgelsen viste, at der var god overensstemmelse med de analytiske løsninger samt FEA resultater.

Da der er fokuseret på den strukturelle respons af overgangsstykket ses der bort fra tårnet i FEA. Da overgangstykket er aksesymmetrisk samt jorden, så er det muligt at modellere kun halvdelen, dermed kan den beregningsmæssige tid reduceres i FEA. En foldnings analyse af overgangsstykket foretaget v.h.a. FEA, og en ikke-lineær materiale model er implementeret. Den ikke-lineær materiale der anvendes er Concrete Damaged Plasticity. Det hydrauliske tryk der vil blive anvendt til overgangsstykket er baseret på en lineær bølge teori. Der er blivet gjort antagelse om strøm trykfordelingen (Drag pressure distribution) og dette antagelse kan ikke benyttes når bølge overfladen er i bølgedalen. I dette projekt bliver den hydraulisk tryk fordeling anvendt når bølge overfladen er på bølgetop. En vind kraft er også anvendt som last. Overgangsstykket vil have en form som en flaske hals. I den indledende undersøgelse hvor der er anvendt lineær elastisk materiale er der analyseret 5 forskellige geometrier. Deres strukturelle respons er undersøgt. I den indledende undersøgelse blev det afklaret at den hydrauliske trykfordelingen havde en minimal indflydelse på snitkræfterne og for foldnings ustabilitet. Derfor er vindlasten den mest kritiske last for overgangsstykket. To overgangsstykker med en enkelt og to lags armeringslag er blevet foreslået.

Ved den lineær foldnings undersøgelse blev det afklaret at der ikke var nogen foldnings risiko for de foreslåede overgangsstykker og at derfor var materiale brud design kriterium. Da skal-konstruktioner aldrig er geometriske perfekte er en lineær foldningsform blevet anvendt som en geometrisk imperfektion for overgangsstykket. En ikke-lineær analyse blev udført for overgangsstykket med geometrisk imperfektion. Analysen viste at overgangsstykket ikke var

følsomme overfor geometriske imperfektion.

Resultatet af rapporten er, at det menes at det er muligt at foretage en overgangsstykket til havbaseret vindturbine ved benyttelse af Compact Reinforced Composite.

CONTENTS

LIST OF FIGURES

LIST OF TABLES

CHAPTER 1

INTRODUCTION

The aim of the project is to model a substructure for an offshore wind turbine with a bucket foundation utilizing FEA. The substructure will be made of a shell structure by utilizing Compact Reinforced Composite. Therefore instability as well as material failure has to be examined. Hence, a buckling analysis of the substructure is carried out by means of FEA, and a nonlinear material model is implemented. The substructure will be shaped as a bottle neck, and analysed how substructures with different geometries perform regarding the load-carrying capacity. The hydraulic pressure that is going to be applied to the substructure is based on linear wave theory.

As a verification study, the buckling load of a dome and a cylinder will be found by an analytical approach. These results are compared with the results of FEA to check the validity of the computational model before it is applied for the analysis of the substructure.

When building offshore windturbines in shallow waters there are different types of foundations that can be applied. The aim of the offshore windturbine foundation is to take and carry the bending moments, horizontal and vertical forces from the wind, waves and self weigth and transfer them to the soil. The way the forces are transfered through the structure to the soil are either having single interface, monopod structures, or several interfaces, multipod structures, with the soil. The interface between the support structure and the soil can be made utilizing piles, caissons or direct foundation. Few examples of in nowadays used foundations for an offshore windturbine are given in Figure 1.1 and Figure 1.2.

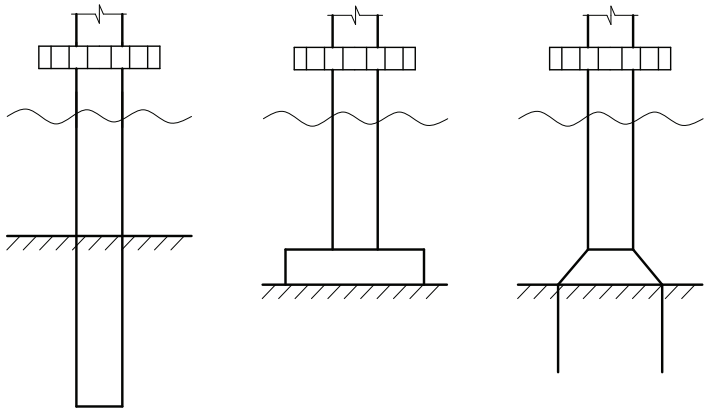

(a) Monopile. (b) Gravity based foundation. (c) Bucket foundation.

Figure 1.1: Monopod support structures for offshore windturbines.

Monopod support structures are used for offshore windturbines in shallow waters, up to 30 m. Monopiles in Figure 1.1a are used widely, the good thing is that its simple and light. The opposite from monopile is gravity foundation see Figure 1.1b its much heavier, the resistance of overturning relies on its self weight, it is cheap to install, but can be susceptible to scour. One of the most widely used foundation types in nowadays is the bucket foundation see Figure 1.1c, its effectiveness, inexpensive price for installing, easy removing makes it very unique.

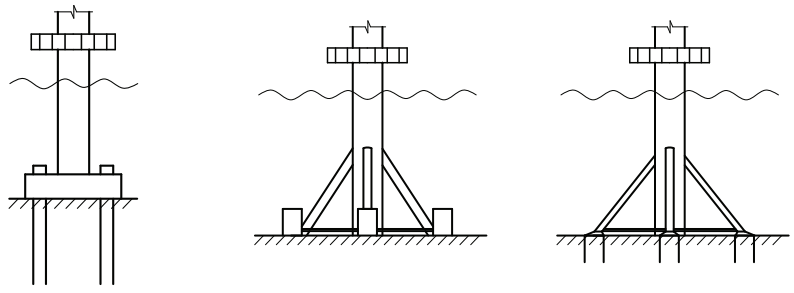

(a) Multipile. (b) Gravity based foundation. (c) Caisson based multipod.

Figure 1.2: Multipod support structures for offshore windturbines.

Multipod support structures are designed for offshore windturbines built in deeper waters when compared with monopods (>30 m). The essence of how it works is almost the same as monopods. The installation is expensive and very difficult to remove [28]. Because the water depth that is going to be considered in this project is 20 m the bucket foundation will in this project utilized and because the benifits that are mentioned earlier. In the following a description of an excisting offshore windturbine with bucket foundation will be presented and why a new substrubture solution to a offshore windturbine is implemented discussed. In this project the offshore wind turbine with bucket foundation will be considered and this can be seen with different parts in Figure 1.3,

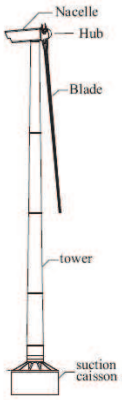

(a) Parts of wind turbine [29].

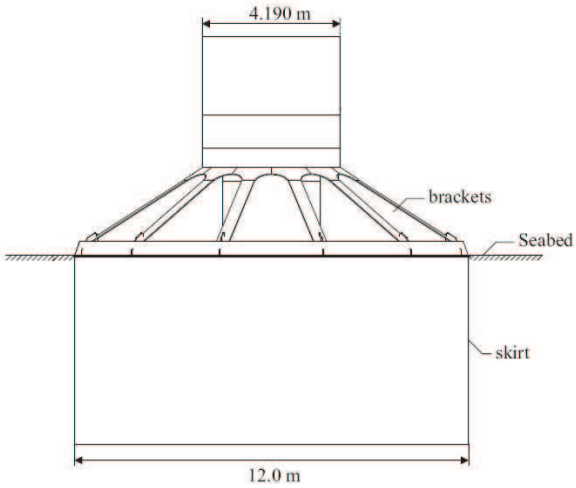

(b) Magnification of the bucket foundation [29].

Figure 1.3: Offshore wind turbine.

The offshore windturbine consist of nacelle, hub, blade and a tower with a boat landing. The transition piece between the tower and bucket foundation is made of steel. The connection between the transition piece and bucket foundation are made with brackets as shown in Figure 1.3b. The brackets are welded together. The offshore windturbine that is going to be considered produces 5 MW.

1.1 Wind turbine with bucket foundation and Mobile Met Mast

In Figure 1.4b the offshore windturbine with a Mobile Met Mast that is a monopod bucket foundation designed as a support structure for a met-mast can be seen [14]. Nowaday the tower and the bucket foundation of the windturbine has a substructure made of steel and the connections are welded together. An example of the substructure and the bucket foundation that are welded together can be seen in Figure 1.4c. The bucket foundation is a cylindrical shell with a closed end and open in the other end. This consist of a skirt and a lid in the closed end. The bucket foundation has been applied in the Oil and Gas industry for the oil platforms where vertical loads are dominant, where as in the offshore windturbine the horizontal loads are dominant and the vertical load is relatively small. The fatigue is the biggest problem for the substructure made of steel with welded connections because of cyclic loads from the wind and waves.

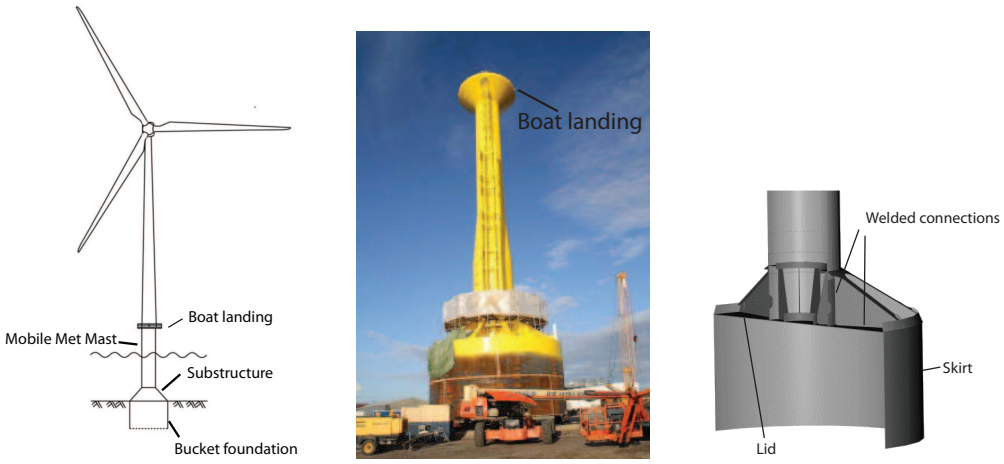

(a) Wind turbine [14]. (b) Mobile met mast [14]. (c) Bucket foundation with substructure [27].

Figure 1.4: Offshore wind turbine with bucket foundation.

The bucket foundation is suited for water depth of 20-30 m. In order to instal the bucket foundation to the seabed, the soil has to be either sand, clay or silt [28].

1.2 New substructure made of Compact Reinforced Composite

To avoid welded connections at the substructure, a new substructure solution where a shell structure is applied presented in this project. In recent decades the ultra high performance concrete, UHPC has been developed, with high compression and tensile strength of the material this has become an alternative solution to the steel. The UHCP has been applied to

offshore wind turbine foundations as a transition piece betweem the bottom tower section and the driven monopile, more than 570 units have already been installed [21, p. 863-869]. The material that is going to be used for the new substructue is Compact Reinforced Composite, CRC. In Figure 1.5a the placement of the new substructure in the offshore windturbine can be seen and this can be seen this will be the new transition piece between the tower and bucket foundation. In Figure 1.5b a magnification of the new substructure can be seen and as it can be this will be doubly curved, where it will consist of a constant radius, concave line, straight line and a convex line. These geometric parameters will be optimized so the critical section forces are minimized.

It is chosen to have a constant radius of the first part between the boat landing and the mean water level, so the stairs to the boat landing can be placed. As it can be seen the shape of the substructure that is going to be analysed looks like a bottle neck and is hollow, therefore this will be a shell structure. The shape look like a bottle necked because the radius of the bucket foundation and tower have different magnitudes.

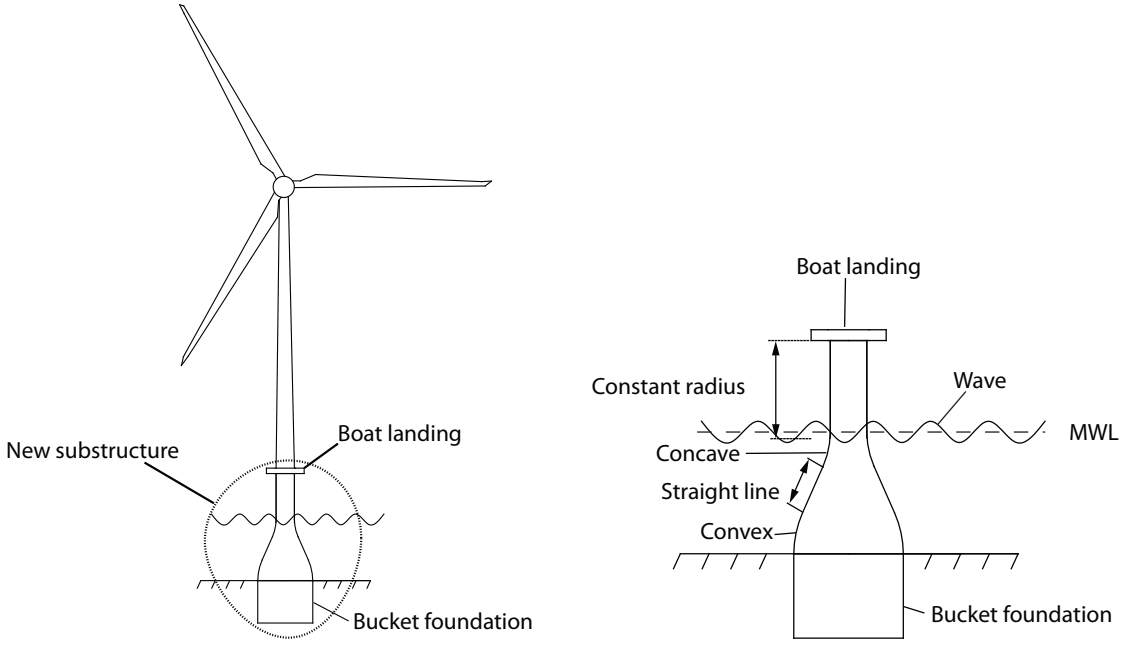

(a) Wind turbine with new substructure.

(b) Magnificafication of the substructure.

Figure 1.5: Offshore wind turbine with new substructure.

A hollow new substructure can be seen from the isoparametric view In Figure 1.6a. This has a vertical axis in the centerline of the substructure. A top view of the new substructure can be seen Figure 1.6b and it is convex shaped.

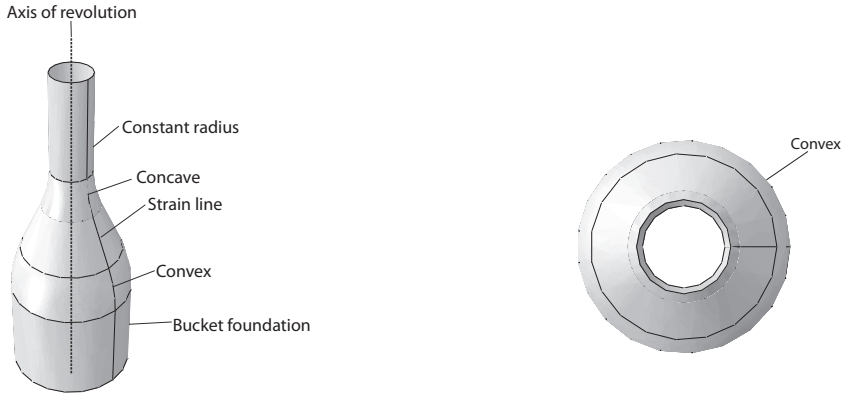

(a) Isoparamteric view of the new substructure.

(b) Top view of the new substructure.

Figure 1.6: Isoparametric and top view of the new substructure.

By using the new concept of the substructure there will be less connections between the bucket foundation and the substructure when compared to the existing Mobile Met Mast, where the possibility of fatigue exist.

the rebar layer that will be invistegated in this project can be seen in Figure 1.7. A substructure with one and two rebar layers will be examined. The rebar layers will be determined by using maximum section forces found in the substructure by elastic analysis.

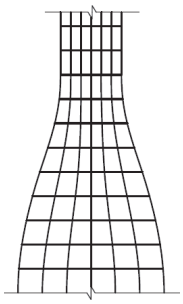

Figure 1.7: Rebar layer for the new substructure.

There are 5 different shapes of the new substructure that will be examined where elastic material is considered. The 3 geometric parameters the concave line, the straight line and the convex line will be optimized, so the shape with the smallest section forces will be used for the final design where a nonlinear material model is applied. A possible way of connecting substructure and bucket foundation is shown below in Figure 1.8.

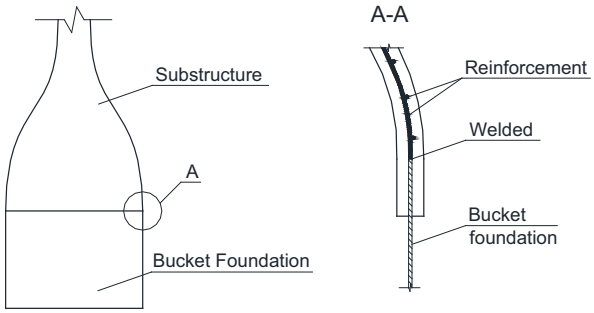

Figure 1.8: Connection between of Bucket Foundation and Substructure

As it can be seen the rebar layer for the substructure could be welded together with the bucket foundation. But this will not further be invistigated in this project.

Dimensions and weight of the wind turbine

The dimensions and weight of the wind turbine that are going to be applied in this project can be seen in Table 1.1

Table 1.1: Properties of the wind turbine.

Property	*Value*
Hub height	90 m
Weight nacelle+rotors	410 t
Weight tower	300 t
Platform	40 t

Water depth and hub height

The water depth that is going to be applied in this project is 20 m from the seabed and up to the mean water level, MWL. The hub height is defined to be from the platform as shown in Figure 1.9. The height from the MWL to the platform is determined to be 15 m.

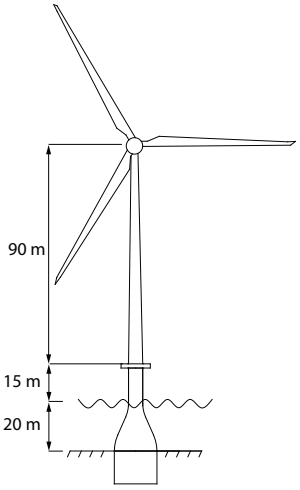

Figure 1.9: Water depth and Hub height.

Bucket foundation dimensions

The geometry dimensions of the bucket foundation that is going to be used in this the geometries are given in Figure 1.10 and the dimensions are shown in Table 1.2

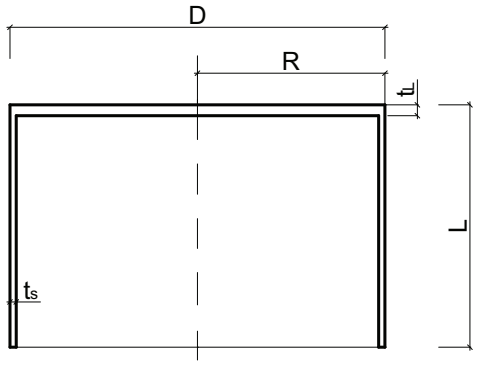

Figure 1.10: Bucket geometry.

Table 1.2: Bucket geometry parameters.

R	L	t_s	t_L
$[m]$	$[m]$	$[m]$	$[m]$
9	14	0.04	0.2

Substructure dimensions

The main dimensions of the substructure that is going to be applied in this project is shown in Figure 1.11. The height from the seabed to the platform is 35 m. The diameter of the tower at the platform is defined to be 6 m.

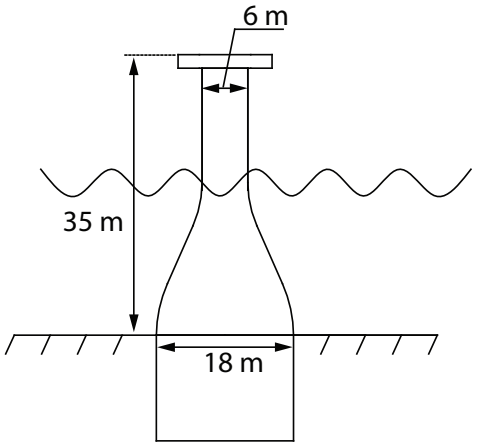

Figure 1.11: Dimensions of the substructure considered in this project.

1.3 Installation proces of the bucket foundation

A short description of the installation proces of the bucket foundation will now be introduced. The installation of the bucket foundation has two phases. The first phase is penetration into the soil due to self weight of the structure and this can be seen in Figure 1.12a. The bearing capacity of the bucket foundation is as follows, the tip of the skirt has a tip resistance, while earth pressure to the skirt gives the bearing capacity of the bucket foundation. So the penetration depth depends on the skirt thickness, the soil strength and the self weight of the

structure. The second phase of the installation is due to suction of the bucket foundation. When suction of the bucket foundation is started, a suction water flow is generated and the effective stresses are reduced around the tip of the skirt and the penetration resistance, this causes nearly a piping failure [25].

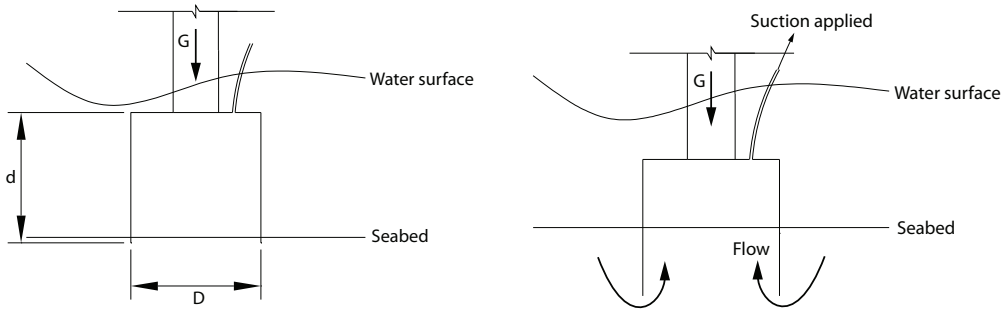

(a) Penetration due to self weight. (b) Penetration due to suction.

Figure 1.12: Installation of bucket foundation.

The magnitude of the sunction that should be applied is determined by subtracting the bearing capacity of the soil with the self weight of the structure. From the suction a downward force is generated in combination with the selfweight [27, p. 10].

1.4 Loads acting on the offshore windturbine

A offshore wind turbine will be subjected to dynamic excitation from the waves on the structure, the wind on the blades and the interaction between the blades and the tower when the blades rotate [25]. These forces will transmitted as relatively large moment to the lid of the bucket foundation where this will be obtained by the soil through the bucket foundation. Even though forces are dynamic these will be treated as static forces in this project. When designing an offshore windturbine for soil stability, geotechnical engineers considers the forces applied to the top of the bucket foundation as shown in Figure 1.13a. For a offshore wind turbine located in a water depth of 20 m the horisontal resulting force from wind and wave will approximately be 30 m above seabed level [28]. The vertical resulting force will act approximately as shown. The contributions from the horizontal forces from the wind on the blades, the tower and the resulting force from the waves can be seen in Figure 1.13b. The total horizontal force from the wave is found from wave the pressure distribution as shown in Figure 1.13b. The loads that are going to considered in this project is the wind force from the blades F_{wind}, the self-weight of the offshore wind turbine and finally the hydraulic pressure distribution acting on the substructure and these are shown in Figure 1.13d. The soil stability of the offshore wind turbine will not be considered in this project, where as the stability of the substructure will be considered. The hydraulic pressure distribution will be based on linear wave theory.

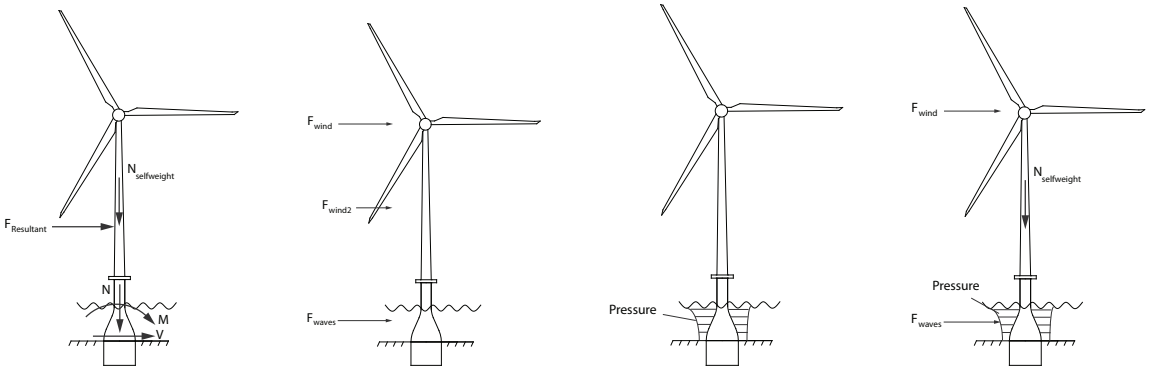

(a) Resultant forces on windturbine and resultant forces on the foundation.

(b) Forces from the wind and the waves.

(c) The pressure distribution from the waves.

(d) Loads applied in the project.

Figure 1.13: Loads on the offshore windturbine.

In Table 1.3 the wind force from the blades that is going to be used in this project can be seen.

Table 1.3: Wind force based on [25].

Property	*Value*
F_{wind}	2 MN

Since there are no extreme data from the waves that is given in this project the wave period that is going to be applied can be seen in Table 1.4

Table 1.4: Wave period based on [25].

Property	*Value*
T	10 s

Since extreme data from waves are not given in this project, the magnitude of the total horizontal force from the waves will be calculated and compared with the expected total horizontal force from waves to be 2 $\pm$ 1 MN for a monopile [25].

Loads acting on the new substructure

Since only the substructure and the bucket foundation with the soil will be modelled in FEA, the loads are going to be transferred to the substructure as shown in Figure 1.14. The wind load is transferred to the boat landing level, and the moment contribution will as well be applied in the boat landing level. The self-weight from the nacelle and rotors, weight of tower and platform will be added as pressure distribution in the boat landing level in the FEA analysis.

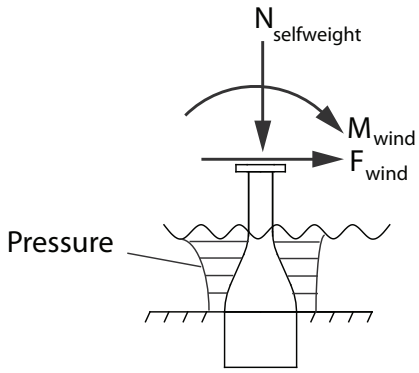

Figure 1.14: Forces in the substructure.

Load considerations

There are two critical situations where the new substructure should be invistigated for, the first one is during the installation of the new substructure and the second one is for the ultimate limit state, ULS. The substructure and the bucket foundation will be subjected to internal pressure during installation as presented in Section 1.3, but this will not be considered in this project. The ULS will be considered for the substructre. The loads are given as design values, while during the analysis the material properties will have characteristic values. The impact from ice loads will not be considered, even though this can cause instability of the substructure by impact and that the overturning moment can be increased so the bucket foundation in addition from the wave, current and wind load is extra loaded so it can cause instability of the soil [16]. The ship impact is as well disregarded in this project even though the loading mechanism is similar from the ice impact. Tidal variation has not been considered, even though it is known that it would increase the wave pressure or total horizontal force. In Abaqus the load is quasistatic, it is increased incrementally. During the life time of the offshore wind turbine, the entire structure will be subjected to the saltwater. Therefore cracks on the substructure are not allowed, due to the fact that the salt water gives corrosion to the rebar causing internal stresses and damages the matrix material of the CRC. Time dependet effect such as creep, shrinkage, temperature and load history will not be considered in this project. Due to the fact this is a shell structure the instability as well as material failure has to be examined. Hence, a buckling analysis of the substructure is carried out by means of FEA, and a nonlinear material model is implemented.

1.5 Expected section forces in the substructure

In this project the considered substructure is equivalent to a closed clamped axisymmetric cross-section of a tubular beam and this can be seen in Figure 1.15a. Due to the horizontal wind load, self weight and the moment from the wind load the expected section forces can as well be seen.

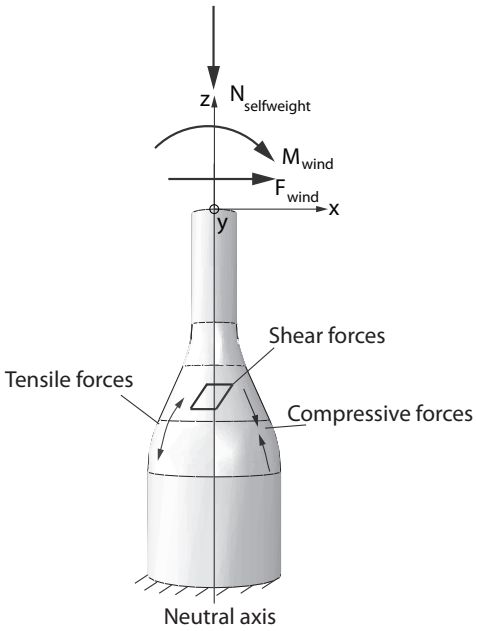

(a) The new substructure equivalent to a clamped tubular beam.

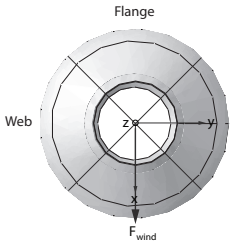

(b) Flange and web of the substructure beam.

Figure 1.15: The new substructure equivalent to a clamped tubular beam.

Because this is a closed axisymmetric profilen, the shear center and the center of mass will be at the same position and therefore the bending and torsion is decoupled [36, p. 17]. It is known from beam theory that the shear stress distribution for the elastic isotropic homogenous cross-section from the shear force looks as in Figure 1.16 [32, p. 64].

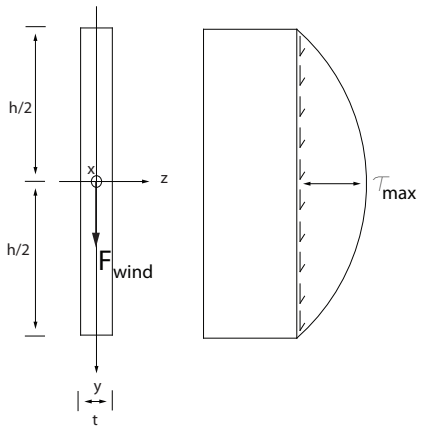

Figure 1.16: Shear stress-distribution from shear force for a solid cross-section [32, p. 64].

As it can be seen the shear stress distribution will be parabolic and will be maximum in the neutral axis of the cross-section. And the shear stresses will be zero in the edges. In Figure 1.15b the tubular beam is divided every quarter of the cross-section. Where the flanges of the closed tubular beam are placed at the top and bottom of the quarter of the cross-section. While the webs of the tubular beam are placed at the sides of the quarter of the cross-section. Therefore it is expected that the shear stress concentration will occur in the webs of the tubular beam due to the fact that the shear stress distribution will be the same as for the solid cross-section. This is an approximation, but it illustrates the overall mechanical

behaviour. The shear stress distribution can be found by Grashof's formula. Where the normal stress distribution is given by Navier's formula. The tensile forces will be found at the top flange while the compression forces will be concentrated at the bottom flange.

When these forces/stresses are expected, the choice of material consideration can be done. For the isotropic material, such as the steel there will be no problem to obtain these forces. The CRC will be orthotropic due to the reinforcing bars, and the shear strength will primarily be provided by the matrix material, when it cracks there will also be contribution from the rebars where they will be cutted and these can be seen in Figure 1.17a when this is subjected to a shear force. The rebar will contribute to the shear stiffness but only to a limited extent regarding shear stiffness see Figure 1.17b. If the shear force is big, the thickness of the shell structure has to be increased.

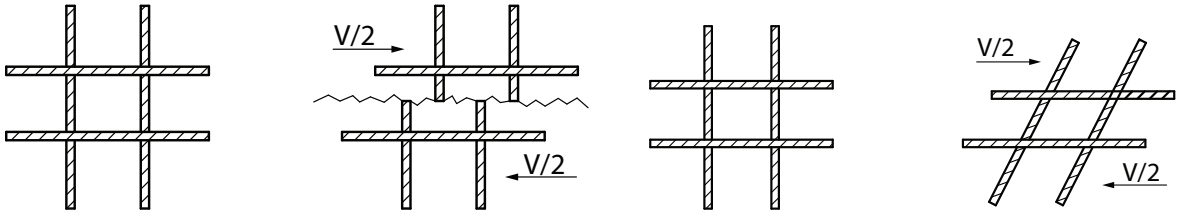

(a) Shear strength. (b) Shear stiffness.

Figure 1.17: Rebar contribution to the shear stiffness and shear strength.

The substructure will be considered as a thin walled tube if $t500 \leq D$, where t is the thickness and D is the radius REFERENCE. So the thickness of the shell and the amount of the rebar layer that will be utilized will be found in this project. In Section 9 the section force respons can be seen when hydraulic pressure, wind load and self weight of the offshore wind turbine are applied.

CHAPTER 2

ULTRA HIGH PERFORMANCE CONCRETE

2.1 Comparisons of conventional concrete and ultra high performance concrete

This section will be based on , and [13] if nothing else is mentioned.

In the following the conventional concrete and ultra high performance concrete, UHPC, will be compared to describe their basic differences.

Before introducing these matrix material, a general description of the concrete will be presented. Concrete contains water, cement, gravel and rocks, therefore the concrete is a brittle material. The concrete has a cohesion and friction. The concrete is characterized by having a high compression strength, while the tensile strength is small. Due to the fact that the tensile strength is small, this problem is solved by adding an extra material that has a bigger tensile strength, for exampel the rebar.

First the matrix material of conventional concrete and UHPC will be compared in microscale by looking at Figure 2.1. In Figure 2.1a the conventional conrete matrix material is shown, here the cement can be seen with the particle size of 10 μm. In Figure 2.1b the matrix material can be seen with cement and ultrafine particles, which can be a microsilica with particle size of 0.1 μm. In Figure 2.1c the matrix material can be seen with aggregate and steel fibres of 0.4 x 12 mm.

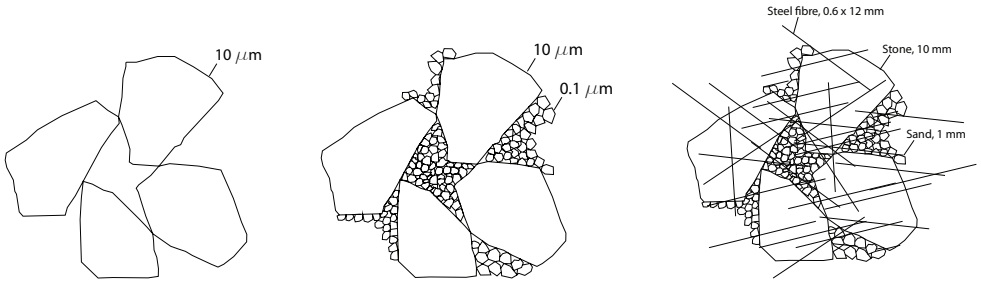

(a) Matrix material with cement.

(b) Matrix material with cement+ultrafine particles.

(c) Matrix material with stone, sand and fibre reinforcement.

Figure 2.1: Conventional concrete and UHPC [12].

When looking at microscale the difference between the conventional concrete and UHPC is that the UHPC has a very strong and dense binders added with dispersants/plasticizers.

The binders are created from hydrated fine particles - cement and ultrafine particles such as microsilica or fly ash. For conventional concrete with poor dispersants / fine particles the constituent is sensitive to local squeezing-out of water, which causes friction blocking and impede movement between neighbouring particles and this is shown in Figure 2.2a. In UHPC this is prevented by applying binders with ultrafine particles added with dispersants, where the matrix material becomes viscous, lubricant, homogenous and liquid. With the lubricant behaviour of the material more stone, sand and fibres can be added and the matrix material can be seen in Figure 2.2b.

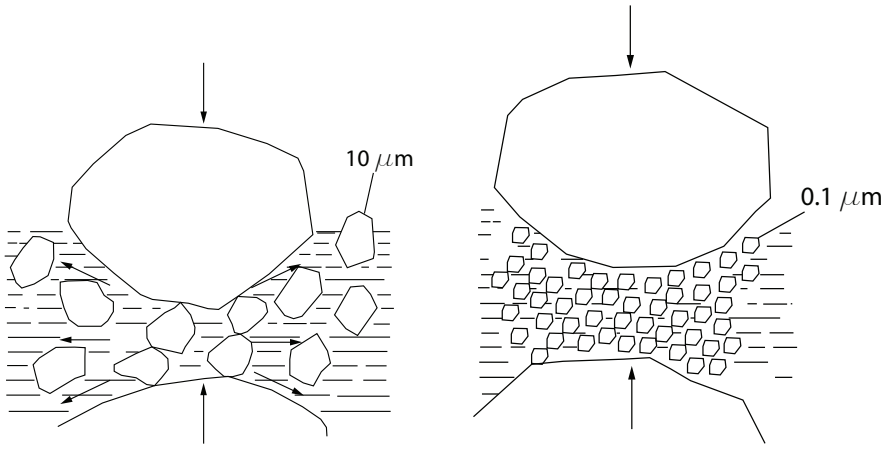

(a) Conventional local squeezing out of fluid.

(b) UHPC ultrafine particle acts as viscous lubricating oil.

Figure 2.2: Locking surface and lubrication from ultrafine particles [12].

When increasing the ultrafine particles in the matrix material for the UHPC, the w/c-ratio is deacreased substantially and very fine pore structure will be established.

In the following the compression strength of the conventional concrete and UHPC will be shown as a function of microsilica and fibre content. In Figure 2.3a the compression strength of the concrete can be seen as a function of microsilica content. For the conventional concrete, where poor dispersants are used, the compression strength decreases when the microsilica content increases. This is due to inhomogenity of the material caused by friction blocking. For the UHPC homogenous packing between microsilica particles and packed cement particles exist. This is possible because good dispersants and dense binders are used in the matrix material, therefore when the microsilica content is increased the compression strength of the constituent will increase.

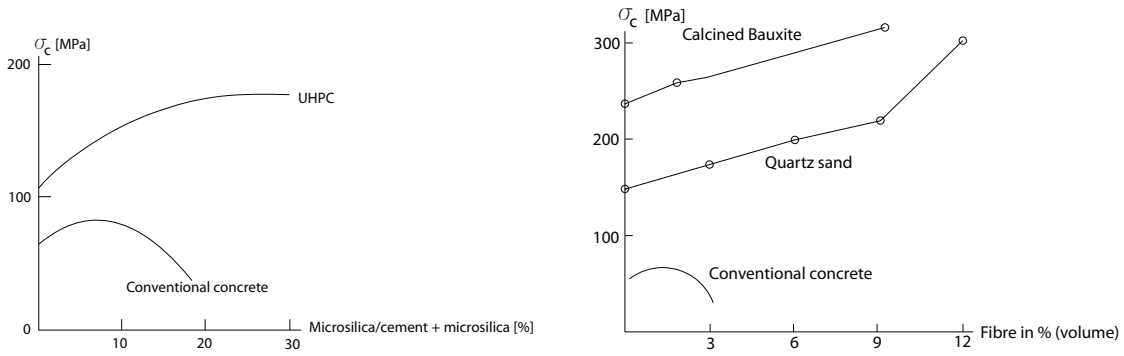

(a) Compression strength function of microsilica content.

(b) Compression strength function of fibre content.

Figure 2.3: Compression strength of conventional concrete and UHPC function of fibre and microsilica content [12].

In conventional concrete only up to 1-2 % of fibre content can be added into the matrix material and if the fibre content is increased further dense material can not be created. Therefore the material quality becomes poor and the compression strength decreases and this is depicted in Figure 2.3b. For the UHPC 6-12 % fibre content of the volume can be added due to the good dispersants, and the fixation between the rebar and matrix material is also improved, where the constituent and the rebar can deform together. It can also be seen that the highest compression strength is achieved when finer material, such as bauxite sand is used, when compared to coarser quartz sand.

In Figure 2.4a the typical crack pattern is shown for the conventional concrete, the crack occurs in the cement paste due to the fact that the aggregate is much stronger than the cement paste. In Figure 2.4b the crack pattern for the UHPC is depicted and the crack occur for both the aggregates and cement paste. This happens because the cement paste is stronger than the aggregate.

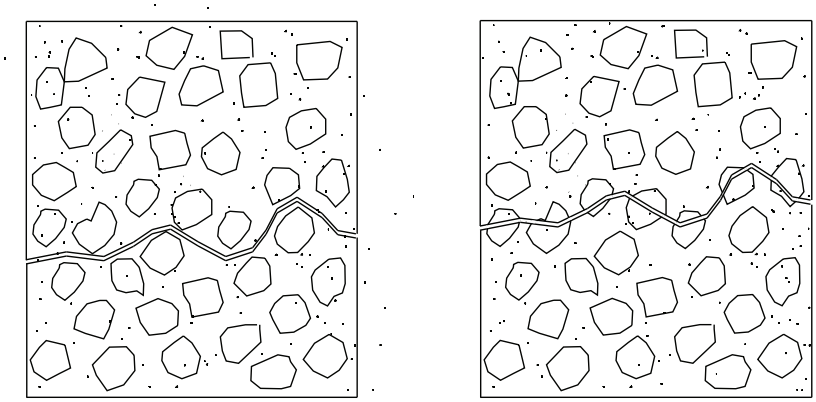

(a) Conventional conrete crack pattern.

(b) UHPC crack pattern.

Figure 2.4: Crack patterns for the conventional concrete and UHPC.

Concept of CRC

In the following the concept behind the Compact Reinforced Composite, CRC, will be presented. When using CRC for structures, the brittleness number is used for the entire structure, global structure, and local place of the structure. A high bearing capacity is characterized by a low brittleness number and the material is insensitive to internal stresses and small cracks. A high brittleness number is characterized by low bearing capacity and the material is sensitive to internal stresses and cracks. So the brittleness number has to be kept as little as possible globally and locally in the structure that is been looking at. The brittleness number is given by

$$B = \frac{\varepsilon_t L}{\Delta} \approx \frac{f_t^2 L}{GE} \text{ or } B \approx \frac{f_t^2 D}{GE} \tag{2.1}$$

Where G is the fracture energy and is given by

$$G = f_t \Delta \tag{2.2}$$

where Δ is the deformation of the fracture zone in m, and f_t is the tensile strength in N/m^2. As it can be seen ε_t, G and E are material parameters, where L and D are characteristic quantities e.g. size of the structure, particle size of ultrafine particles, diameter of fibres and diameter of the reinforcement [11, p. 6]. The ductility is given by

$$D = \frac{\Delta}{\varepsilon_t L} \approx \frac{GE}{f_t^2 L} \text{ or } D \approx \frac{GE}{f_t^2 D} \tag{2.3}$$

as it can be seen this is reciprocal to the brittleness number. In the following a brittle material and a ductile material behaviour are illustrated in a load displacement curve response. There exist two different strength: yielding strength and ultimate/failure strength. When yielding strength has occured, inelastic behaviour is started. In Figure 2.5a a example of brittle material is shown where the yielding strength and failure strength are equal and there only exist elastic response before failure occur. In Figure 2.5b an example of stress strain relation for a ductile material is shown, where there is hardening after yielding strength has been reached. After the peak load is reached there is a softening of the material then failure occurs [37, p. 15].

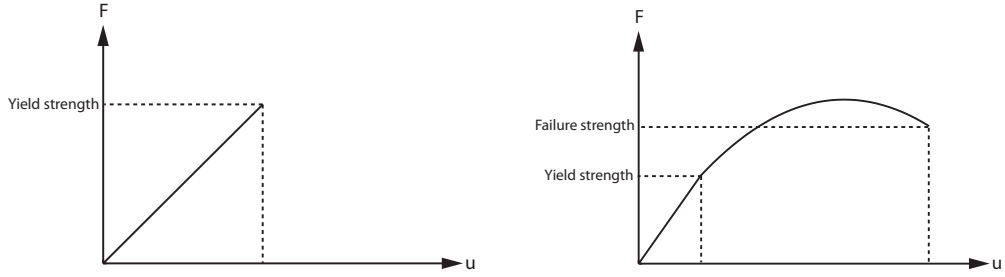

(a) Brittle material. (b) Ductile material.

Figure 2.5: Load displacement curves for brittle and ductile material.

The principal behind the design procedure for CRC is to look at the global structure size L and local material size D such as the diameter of rebar, fibres, aggregates and particles size so these combined together gives a low brittleness number for the structure. The illustration of different material mixing can be seen in Figure 2.6, where a rectangular cross-section is shown. A fibre reinforced concrete can be seen in Figure 2.6a, here the cement paste has high brittleness number so this is lowered by adding fibres with a diameter D. In Figure 2.6b a concrete with rebar can be seen, the diameter of the rebar D is huge so this increases the local brittleness number and therefore cracks occur. This can be prevented by giving the matrix material a local ductility around the rebars by choosing the diameter, amount and type of fibres that gives ductility corresponding to the rebar and this is shown in Figure 2.6c. In CRC the matrix material is given a ductility of the order of 100 times that of the binder by applying fibres and particles [12].

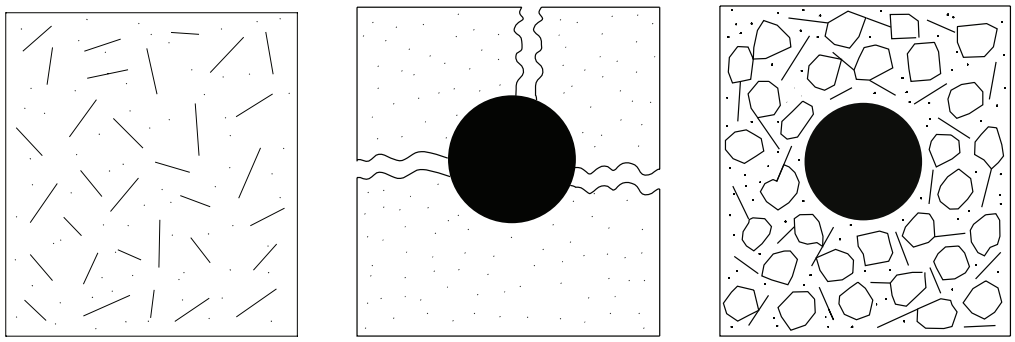

(a) Concrete with fibre reinforcement.

(b) Brittle concrete with rebar reinforcement.

(c) Ductile concrete with fibre and rebar reinforcement.

Figure 2.6: Cross-section of a rectangular beam [12].

So in the design proces of CRC, the brittleness number is kept as low as possible locally and globally. In Figure 2.7a the material ductility as a function of volume concentration of particles is shown. By increasing the ultrafine particles into the pure concrete paste the ductility of the matrix material is increased exponentially.

The fracture energy can as will be increased by applying fibres into the constituent and this is illustrated as a function of fibre content in Figure 2.7b. As it can be seen it increases linearly. When the matrix material is subjected to tensile forces and there occur huge tensile strains some of the fibres will be extracted from the matrix material, by this respons the fracture energy, G is increased. Furthermore the fibres should not break over when they are subjected to tensile forces, otherwise they would not effectively contribute to increase the fracture energy [10].

For conventional concrete without fibre content, the fracture energy is about 0.1 kN/m, as it can be seen the fracture energy is increased more than a factor of 100 for a matrix material with 12 % of fibre content.

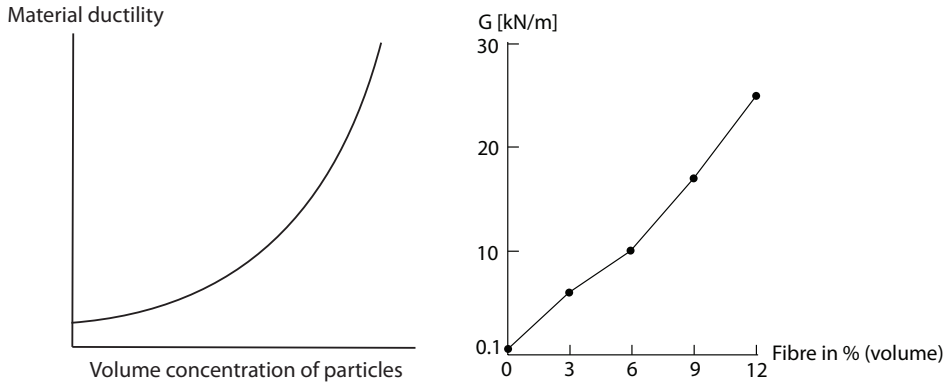

(a) Material ductility. (b) Failure energy.

Figure 2.7: Concrete improvement with increasing particle of fibre content [12].

Due to the mixture of the matrix material there can be closely spaced rebars where a distance of 10-15 *mm* can be used between rebars. And due to the low porosity of the matrix material, a cover layer of only 10-15 *mm* is only demanded. In CRC due to the fact that the binders, plasticizers and fibres gives a effective fixation for the rebar in the matrix material and by having a very close spacing between rebars, the tensile strain failure of the matrix material is increased substantially. This gives tensile "strain hardening", where the matrix material becomes very flexible when subjected to tensile forces. By combining these materials huge crack propagations are prevented until near the yielding of rebars. Reinforcement such as wires or cables with a tensile strength of 2000 MPa can be used in CRC, due to the fact that these have relatively huge tensile straining. Since closely spaced rebars can be used, the material behaves like a composite material and is orthotropic.

The concept of CRC is to have large fracture energy, not only the fibres contribute to increase the fracture energy, by having closely spaced rebars the cracks are distributed globally to the structure and thereby the fracture energy is increased further. Where as in conventional concrete a single local failure zone exist in the structure [10].

CRC can resist concentrated forces, that is why this is named compact. The rebars that can be applied to the CRC do not have to be prestressed.

In Table 2.1 the property differences between the conventional concrete and UHPC are shown.

Table 2.1: Comparing conventional concrete with new UHPC [12].

	Conventional concrete	New Concrete/UHPC		
		Matrix material		CRC
		0-2 % fibre	4-12 % fibre	
σ_c [MPa]	80	120-270	160-400	160-400
σ_t [MPa]	5	6-15	10-30	100-300
ρ [kg/m^3]	2500	2500-2800	2600-3200	3000-4000
E [MPa]	50	60-100	60-100	60-110
G [N/m]	150	150-1500	5000-40000	$2 \cdot 10^5 - 4 \cdot 10^6$
w/c	0.3-0.6	0.1-0.15		
Frost resistance	moderate/good	frost proof without air entraintment		
Corrosion resistance	moderate/good	corrosion save with 10-15 mm of cover layer		

Uniaxial compressive strength

In Table 2.1 the uniaxial compression strength for the CRC and the UHPC with fibre content with 4-12 % is the same and that these have a factor 5 times higher compression strength than the conventional concrete.

Uniaxial tensile strength

It can be seen in Table 2.1 that the uniaxial tensile strenght for the CRC is 10 times higher than for the UHPC with 4-12 % of fibre content and that the tensile strength for the CRC is 60 times higher than the conventional concrete.

Young's modulus

The Young's modulus for the UHPC and CRC have similar values and have higher values than the conventional concrete.

Fracture energy

In Table 2.1 the fracture energy is higher for the CRC when compared with UHPC and particularly when compared with the conventional concrete.

When comparing the w/c-ratio between UHPC, CRC and conventional concrete, the amount of water that has to be used for UHPC and CRC is much lower. The frost and corrosion resistance for the UHPC and CRC are excellent when compared with conventional concrete. A cover layer of 10-15 mm for the UHPC and CRC is enough due to the low porosity of the matrix material. For example a cover layer of only 10 mm is applied for CRC decks in the Great belt even though the life demand for the bridge is 100 years [8]. Where as for the conventional concrete, a cover layer of about 50 mm has to be applied for aggressive enviroment. In the following the concept of CRC is summed up.

Design strategy of CRC

The design strategy for the CRC is based on fracture mechanics and following are considered [11]

- High concentration of fine strong and stiff fibres are mixed into the matrix material. This increases the tensile stresses and strains
- To further increase the ultimate tensile strains of the matrix material effective fixation to the bars are achieved. Then the matrix material and the rebars deform together
- A small brittleness number is achieved by looking at the global and local ductility

CHAPTER 3

MATERIAL MODELS FOR CONCRETE AND STEEL

3.1 Introduction of material models for concrete, steel and soil

In the following the material models of concrete and steel will be presented. There are two material models for concrete that could be applied to model a reinforced concrete in FEA. These are the Concrete Smeared Cracking, CSC, and the Concrete Damaged plasticity, CDP. These material models describe the hardening and softening behaviour of the concrete. The material model of steel is chosen to be Von Mises. First the overall introduction for the models will be described, and after that a more detailed description will be presented for one of the models of concrete that is applied in this project.

Concrete smeared cracking

Following overall material behavior for the concrete smeared cracking will now be introduced [1, chap. 18.5.1].

- Can be applied to plain concrete
- Can be used to model a reinforced concrete
- Do not model stiffness degradation in compressive state
- Intended for monotonic loading under low confining pressures
- Cracking is the most important aspect of the model
- Associated flow and isotropic hardening is applied for the yield/failure surface
- Simple yield/failure surface

Concrete damaged plasticity

Next the overall presentation of the Concrete damaged plasticity now be introduced [1, chap. 18.5.3].

- Can be applied to plain concrete

- Can be used to model a reinforced concrete
- Model inelastic behavior for the concrete in compressive and tension state
- Intended for monotonic, cyclic, dynamic loading under low confining pressure
- Different degradation in elastic stiffness in tension and compression
- Non-associated flow is applied
- Stiffness recovery effect during the cycling loading
- The initial yield stress in compression is factor 10 or more higher than the initial yield stress in compression

As it can be seen in the material model for CDP is more advanced than the CSC, where this model is simple and computional faster, due to a more simpel model. The CDP can be used for the structures subjected to dynamic excitation, which the substructure will be. Therefore the CDP will be applied in this project, due to that the material model is more advanced.

Von Mises

The material model for the steel will be Von Mises and in Figure 3.1a this can be seen in deviatoric plane. As it can be seen this is a circle. In Figure 3.1b the meridian plane is shown and this is constant. In Figure 3.1c a typical stress-strain relation for the steel rebar is depicted as (a). This is linear elastic and isotropic before yielding is reached. After that there is hardening and when the peak stress has been reached softening appears. After softening there is failure. In this project the stress-strain relation for the steel is modelled as an elastic-perfectly plastic material and this is depicted in Figure 3.1c as (b). When this is simplified into elastic-perfectly plastic this corresponds to the material model of Von Mises.

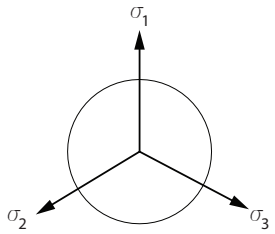

(a) Von Mises in deviatoric plane [33].

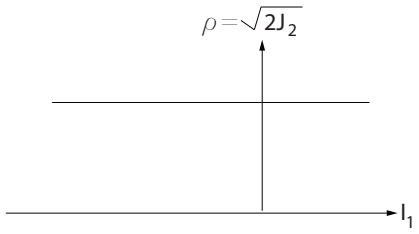

(b) Von Mises in meridian plane [33].

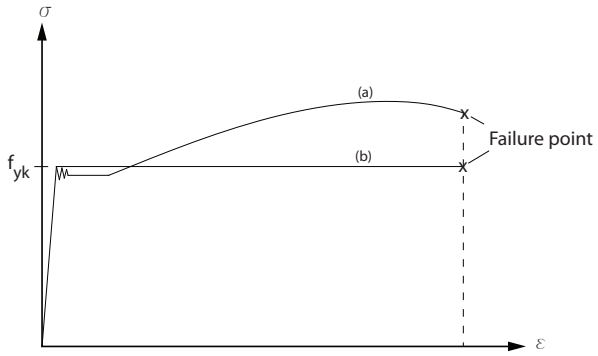

(c) Stress-strain relation for the rebar [26].

Figure 3.1: Material model of steel.

3.2 Concrete Damaged Plasticity

This section is based on [1, chap. 18.5.3], [6, chap. 4.5.2] and [30] if anything is not mentioned.

The model is a continuum plasticity based model for concrete. The model assumes two main failures and these are the tensile and compressive cracking of the concrete material.

The evolution of the yield or failure surface is defined by the hardening parameter $\tilde{\varepsilon}^{pl}$ that contains

$$\tilde{\varepsilon}^{\mathbf{pl}} = \begin{bmatrix} \tilde{\varepsilon}_t^{pl} \\ \tilde{\varepsilon}_c^{pl} \end{bmatrix}$$

where $\tilde{\varepsilon}_t^{pl}$, and $\tilde{\varepsilon}_c^{pl}$ are defined as tensile and compressive equivalent plastic strain. The strain rate decomposition is assumed to be

$$\dot{\varepsilon} = \dot{\varepsilon}^{el} + \dot{\varepsilon}^{pl} \tag{3.1}$$

where, $\dot{\varepsilon}$, is the total strain rate, $\dot{\varepsilon}^{el}$, is the elastic strain rate, $\dot{\varepsilon}^{pl}$, is the plastic strain rate.

3.2.1 Uniaxial loading response of a plain concrete

The uniaxial compressive and tension response of the model can be seen in Figure 3.2. The uniaxial compressive response for the plain concrete in stress-strain curve can be seen in Figure 3.2a. Before reaching the initial yield stress, $-\sigma_{co}$ the material is elastic. There is hardening of the material until the ultimate stress σ_{cu} is reached. When plasticity occurs the material gets irreversible. After the ultimate stress the material softens. The uniaxial tension

response for plain concrete in stress-strain curve is shown in Figure 3.2b. The concrete is elastic until the failure stress σ_{to} is reached. After that the concrete material gets micro-cracks where it is represented macroscopically by softening in stress-strain curve and the loads/stresses will be then transfered to the reinforcement, when the stresses have reached zero stresses.

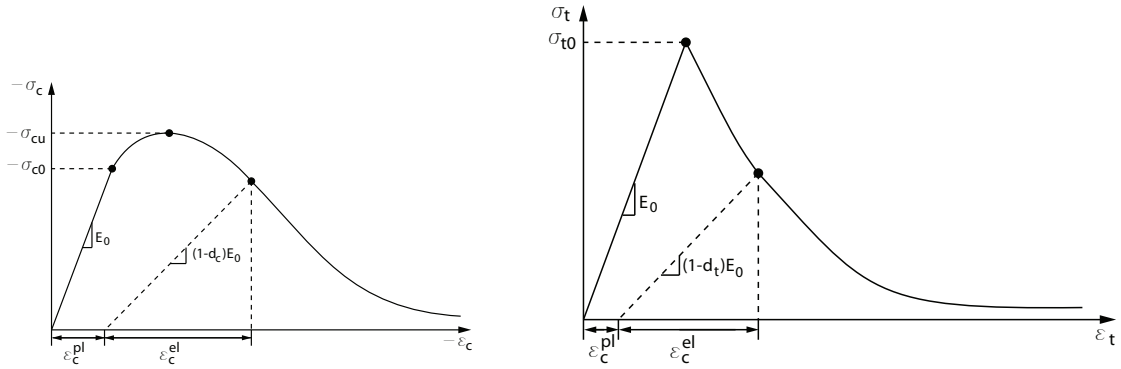

(a) Uniaxial compressive response of concrete.

(b) Uniaxial tensile response of concrete.

Figure 3.2: Uniaxial compressive and tension response of concrete [1].

As it can be seen in Figure 3.2 the elastic stiffness has degraded in terms of a scalar degradation variable d, when there is unloading after the material becomes plastic and this holds both for the tensile and compressive response.

$$E = (1 - d)E_0 \tag{3.2}$$

The stiffness degradation d, is a function of the stress state. For the uniaxial compressive and the uniaxial tensile loadings the damage parameters are d_t, and d_c. Therefore the degradation for the elastic stiffness for the uniaxial compressive loading is given by

$$E = (1 - d_c)E_0 \tag{3.3}$$

and this elastic degradation can be seen in Figure 3.2a. The degradation of the elastic stiffness for the uniaxial tensile loading is given by

$$E = (1 - d_t)E_0 \tag{3.4}$$

In Figure 3.2b the degradation can be seen when unloading after the plasticity has occured, and this is shown with dotted lines. The degradation variables are the functions of the following

$$d_t = d_t(\tilde{\varepsilon}_t^{pl}, \theta, f_i); 0 \leq d_t \leq 1 \tag{3.5}$$

$$d_c = d_c(\tilde{\varepsilon}_c^{pl}, \theta, f_i); 0 \leq d_c \leq 1 \tag{3.6}$$

where the subscripts t and c refer to tension and compression. $\tilde{\varepsilon}_t^{pl}$ and $\tilde{\varepsilon}_c^{pl}$ have been defined above. $\dot{\tilde{\varepsilon}}_t^{pl}$ and $\dot{\tilde{\varepsilon}}_t^{pl}$ are the equivalent plastic strain rate. θ is the temperature, which are disregarded in this project. f_i are other predefined field variables. If the damage variable is zero there is no degradation to the elastic stiffness. On the other hand if it is 1 it represents total loss of strength.

In *Abaqus* when defining the stress-strain curves for compressive and tensile response, the plastic strains has to be defined as an input. The stresses are functions of

$$\sigma_t = \sigma_t(\tilde{\varepsilon}_t^{pl}, \dot{\tilde{\varepsilon}}_t^{pl}, \theta, f_i) \tag{3.7}$$

$$\sigma_c = \sigma_c(\tilde{\varepsilon}_c^{pl}, \dot{\tilde{\varepsilon}}_c^{pl}, \theta, f_i) \tag{3.8}$$

The stress-strain relation under uniaxial tensile and uniaxial compressive is for E_0 initial undamaged stiffness

$$\sigma_t = (1 - d_t)E_0(\varepsilon_t - \tilde{\varepsilon}_t^{pl}) \tag{3.9}$$

$$\sigma_c = (1 - d_c)E_0(\varepsilon_c - \tilde{\varepsilon}_c^{pl}) \tag{3.10}$$

The effective tensile and compressive cohesion stresses is given by

$$\bar{\sigma_t} = \frac{\sigma_t}{1 - d_t} \tag{3.11}$$

$$\bar{\sigma_c} = \frac{\sigma_c}{1 - d_c} \tag{3.12}$$

The equations (3.11) (3.12) states that this is only the undamaged area which withstands the external loads. Next the stress-strain relation for the continuum mechanics introduced. The stress-strain relation, or the constitutive relation is given by scalar damaged elasticity

$$\sigma = (1 - d)D_0^{el} : (\varepsilon - \varepsilon^{pl}) = D^{el} : (\varepsilon - \varepsilon^{pl}) \tag{3.13}$$

where D_0^{el} is the initial undamaged stiffness of the material, $D^{el} = (1 - d)D_0^{el}$ is the degraded elastic stiffness, d is the scalar stiffness degradation parameter, and ranges from 0 to 1, where 0 is the undamaged stiffness and 1 is the fully damaged stiffness. The stiffness degradation is isotropic. The damage is associated with crushing and cracking of the material. For damaged continuum mechanics the effective stress is defined as

$$\bar{\sigma} = D_0^{el} : (\varepsilon - \varepsilon^{pl}) \tag{3.14}$$

The Cauchy stress is then calculated by

$$\sigma = (1 - d)\bar{\sigma} \tag{3.15}$$

As it can be seen in (3.15) the Cauchy stress is related to the effective stress through the scalar degradation relation. If the material is undamaged, for $d = 0$ then (3.15) equals the Cauchy stress.

3.2.2 Uniaxial tensile loading response of the plain concrete

In *Abaqus* the tensile response of the plain concrete is modelled by using tension stiffening. The tension stiffening can be applied by either using postfailure stress-strain relation and fracture energy cracking criterion. In this project the postfailure stress-strain relation is used. The tension stiffening models the load transfer between the rebar and concrete.

In *Abaqus* the input for the tension stiffening is given by as absolute value of the total strain, ε_0, minus the direct strain at cracking, which is the failure strain, ε_f, and this is given by

$$\varepsilon_{TS} = \varepsilon_0 - \varepsilon_f \tag{3.16}$$

In Figure 3.3 an example of an tension stiffening development is shown.

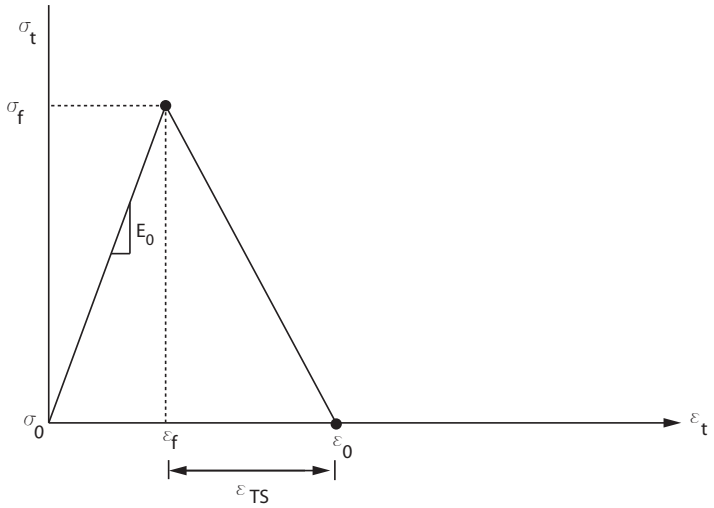

Figure 3.3: Tension stiffening.

It can be seen that the material is linear elastic until the ultimate tensile strength is reached, after that there is softening of the concrete. During the softening the forces from the concrete is transfered to the rebars and when the stresses reaches zero, for the failure strain ε_f for the concrete, this means that the tension load is completly transfered to the rebar.

3.2.3 Multiaxial behaviour

In the following the multiaxial behaviour is described and this is presented in plane stress. In Figure 3.4 the multiaxial response is depicted and the failure surface is shown.

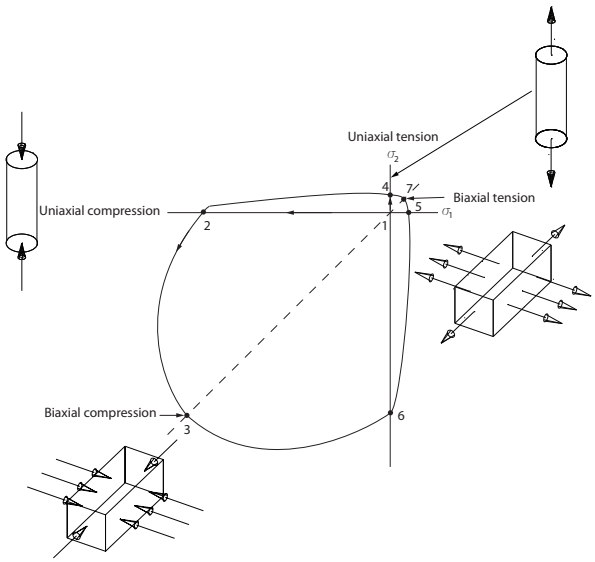

Figure 3.4: Yield surface in plane stress.

If the stresses are respectively in the axis of σ_1, or σ_2 these are either pure compressive stress or tensile stress. If the stresses are in the dashed line, these are in either pure biaxial compressive stress or biaxial tensile stress state. Then there are different combinations of stresses, one of them is combination of the uniaxial compressive stress and uniaxial tensile stress which is shown from point four to two and from six to five. Then there is a combination of the biaxial compressive stress and uniaxial compressive stress from point two to three and from three to six. Then there also are combination of the biaxial tensile stresses and uniaxial tensile stresses between four to seven and from seven to five.

3.2.4 Yield surface of the model

The yield (failure) surface is controlled by the hardening variables $\tilde{\varepsilon_t^{pl}}$ and $\tilde{\varepsilon_c^{pl}}$. In terms of the effective stresses the yield criterion becomes in the effective stress space

$$F(\bar{\sigma}, \tilde{\varepsilon^{pl}}) \leq 0 \tag{3.17}$$

or

$$F = \frac{1}{1-\alpha}\left(\bar{q}3\alpha\bar{p} + \beta(\tilde{\varepsilon}^{pl})\left\langle\hat{\bar{\sigma}}_{max}\right\rangle - \gamma\left\langle\hat{\bar{\sigma}}_{max}\right\rangle\right) - \bar{\sigma_c}(\tilde{\varepsilon}_c^{pl}) \tag{3.18}$$

this is a modified Mohr-Coulomb failure function with

$$\alpha = \frac{(\sigma_{b0}/\sigma_{c0}) - 1}{2(\sigma_{b0}/\sigma_{c0}) - 1}; 0 \leq \alpha \leq 0.5 \tag{3.19}$$

$$\beta = \frac{\bar{\sigma}_c(\tilde{\varepsilon}_c^{pl})}{\bar{\sigma}_t(\tilde{\varepsilon}_t^{pl})}(1-\alpha) - (1+\alpha) \tag{3.20}$$

$$\gamma = \frac{3(1 - K_c)}{2K_c - 1} \tag{3.21}$$

Where $\hat{\bar{\sigma}}_{max}$ is the maximum principal effective stress, σ_{b0}/σ_{c0} is the ratio of initial equibiaxial compressive yield stress to initial uniaxial compressive yield stress. K_c is the ratio of the second stress invariant on the tensile meridian q_{tm} to that on the compressive meridian, q_{cm} at initial yield for any given value of the pressure invariant p such that the maximum principal stress is negative $\hat{\sigma}_{max}$. $\bar{p}$ is the hydrostatic pressure given by

$$\bar{p} = -\frac{1}{3} trace(\bar{\sigma}) \tag{3.22}$$

$\bar{q}$, is the Mises equivalent effective stress and this is given by

$$\bar{q} = \sqrt{\frac{3}{2}(\bar{S} : \bar{S})} \tag{3.23}$$

where, $\bar{S}$, is the effective stress deviator and is given by

$$\bar{S} = \bar{\sigma} + \bar{p}I \tag{3.24}$$

In Figure 3.5 the yield surface in the deviatoric plane is illustrated. The failure criterion for the damaged plasticity can be seen for $\alpha = 0.08$, and $\alpha = 0.1212$, and for the default value for $K_c = \frac{2}{3}$. The deviatoric plane for the Mohr-Coulomb is also shown. If it is compared to Mohr-Coulomb criterion, which is a hexagon, the models are similar, due to the fact that the CDP model is a modified Mohr-Coulomb. The models are isotropic materials, so the distance from the zero point from the principal coordinate system to the corners of the deviatoric planes along the axis of the principal stress s are the same for all corners. The modified Mohr-Coulomb can be seen in Figure 3.6 in the meridian plane where the compressive and tensile meridian are shown. The tensile meridian and the compressive meridian increases linearly, when these are subjected to compressive hydrostastic stress, until they reach the deviatoric stress. But if the hydrostatic load is tensile, due to the fact that the concrete has a small tensile strength, the failure surface is reached relatively much faster when compared with the compressive hydrostatic loading.

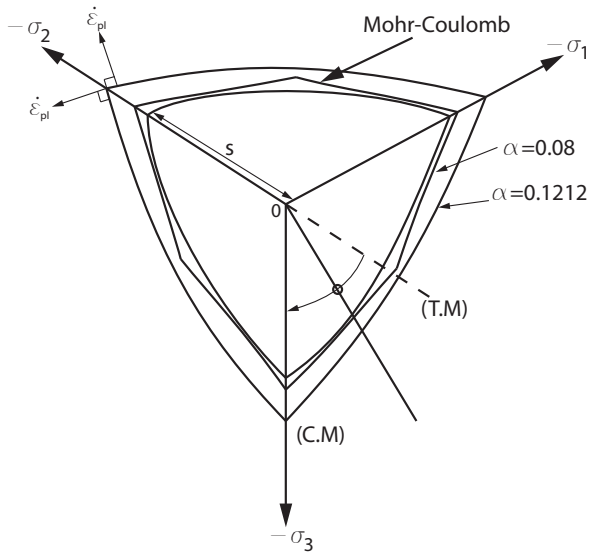

Figure 3.5: Mohr-Coulomb and modified Mohr-Coulomb.

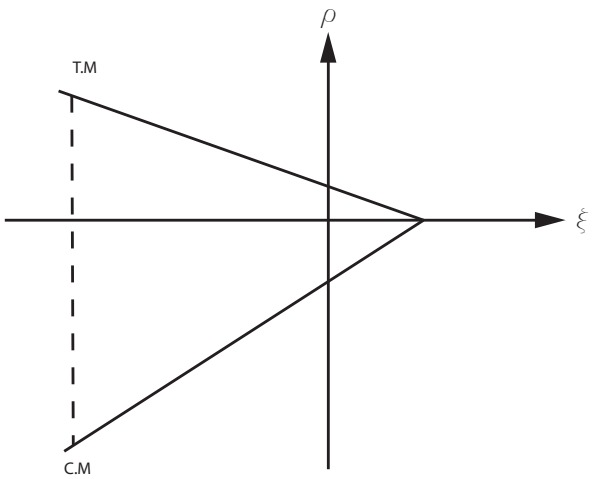

Figure 3.6: Modified Mohr-Coulomb in meridian plane.

When looking at the failure surface of the modified Mohr-Coulomb and Mohr-Coulomb in Figure 3.5 the corners are espicially critical due to the fact that the plastic potential $\dot{\varepsilon}_{pl}$, can not ambigously be determined when using associated flow, $F = F$. Therefore a nonassociated flow potential is applied for this purpose where hyperbolic Drucker-Prager function G, is applied $F \neq G$.

3.2.5 Flow potential

The plastic flow potential in CDP is modelled by applying Drucker-Prager hyperbolic function G and this is given by

$$G = \sqrt{(\varepsilon\sigma_{to}tan(\psi))^2 + \bar{q}^2} - \bar{p}tan(\psi) \tag{3.25}$$

where

- ψ is the dilatation angle measured from the p-q plane
- σ_{to} is the uniaxial tensile stress at failure
- ε is a parameter that defines the rate at which the function approaches the asymptote

In effective stress space the plastic potential is defined by

$$\dot{\varepsilon}^{pl} = \dot{\lambda}\frac{\partial G(\bar{\sigma})}{\partial \bar{\sigma}} \tag{3.26}$$

where

- $\dot{\lambda}$ is the nonnegative plastic multiplier

The hyperbolic Drucker-Prager failure or yield surface in deviatoric plane can be seen in Figure 3.7.

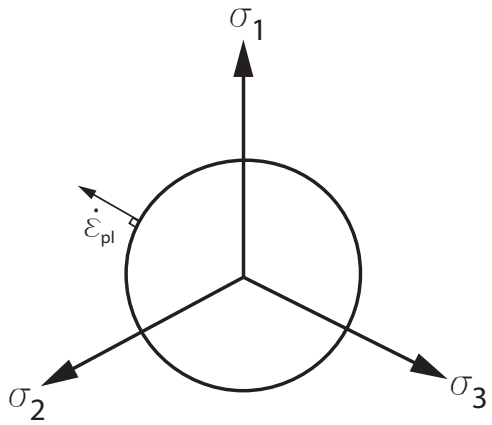

Figure 3.7: Hyperbolic Drucker-Prager in deviatoric plane.

In the figure the plastic potential can be defined all over the failure surface, due to the fact that the surface is circular. in Figure 3.8 the Drucker-Prager failure criterion can be seen in p-q-plane, and this is some sort of a meridian plane.

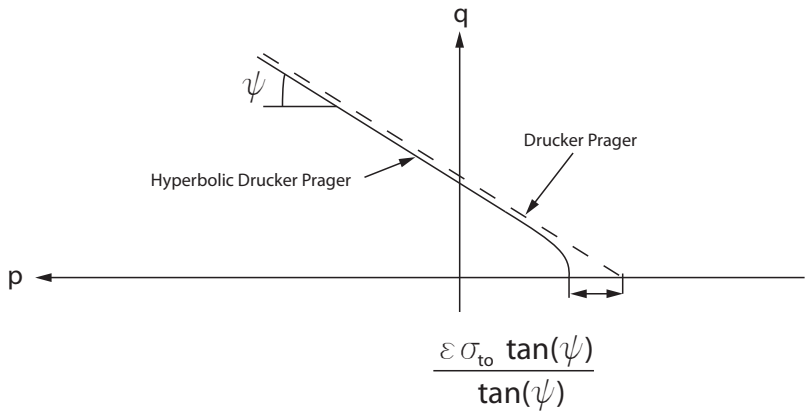

Figure 3.8: Hyperbolic Drucker-Prager and Drucker-Prager in meridian plane.

It can be seen that the hyperbolic Drucker Prager is curved when the mean stress is low, when it is increased the meridian plane gets similar to the ordinary Drucker Prager. For relatively high mean stress the inclination of the line is defined by the dilation angle, ψ.

3.3 Mechanical properties of ultra high performance concrete

In the following mechanical properties of the UHPC that will be applied in this project presented. The stress-strain relations that are presented can directly be used as input in *Abaqus* and during the analysis characteristic values will be utilized in this project. The mechanical property of the UHPC can be seen in Table 3.1

Table 3.1: Mechanical properties of the UHPC [31].

Property	*Parameter*	*Value*
Compressive strength	σ_c	155 MPa
Tensile strength	σ_t	12.5 MPa
Yield stress	σ_f	114 MPa
Young's modulus	E	82.426 MPa
Young's modulus	E	40.000 MPa
Poisson's ratio	ν	0.23
Dilation angle	ψ	34.43^o
Density	ρ_c	$3200kg/m^3$

Instead of using Young's modulus of 82.426 MPa, a lower value of 44.000 MPa will be applied in this project [24].

Uniaxial compressive stress-strain relation

The uniaxial compressive stress-strain relation can be seen in Table 3.2. The plastic strains are shown.

Table 3.2: Uniaxial compressive stress-strain relation for UHPC [31].

σ_c	ε_{pl}
$[MPa]$	$[-]$
114	0
155	0.0002
112	0.00015
57	0.0029
20	0.0042
0	0.053

Uniaxial tensile stress-strain relation

The uniaxial tensile stress-strain relation can be seen in Table 3.3.

Table 3.3: Uniaxial tensile stress-strain relation for UHPC [31].

σ_t	ε_{pl}
$[MPa]$	$[-]$
12.5	0
12	0.0002
0	0.002

Instead of using Table 3.3 for the uniaxial tensile response another fibre reinforced UHPC with Young's modulus of 44 GPa and with 6 vol. % steel fibres will be applied based on [24] and this can be seen in Table 3.4.

Table 3.4: Uniaxial tensile stress-strain relation for UHPC [24].

σ_t	ε_{pl}
$[MPa]$	$[-]$
10	0.02
5.4	0.15
2.1	0.4
0	0.97

When comparing Table 3.3 and 3.4, the last table has a more longer plastic strains and therefore is more ductile.

Cover layer and rebar spacing

In the following the minimal cover layer and the rebar spacing that is going to be applied in this project is shown in Table 3.5.

Table 3.5: Cover layer and rebar spacing applied in this project.

Cover layer	Rebar spacing
$[mm]$	$[mm]$
15	15

3.4 Soil

Soil Condition

The soil condition that is going to be used in this project is chosen to be undrained clay, the soil properties can be seen in Table 3.6. The undrained clay will only be considered as an elastic material.

Property	*Parameter*	*Value*
Young's modulus	E	75 MPa
Poisson's ratio	ν	0.49
Density	ρ	$1800 kg/m^3$

Table 3.6: Soil properties for the undrained clay.

The soil stability is disregarded in this project since the focus is the stability of the substructure. So the soil in this project will be regarded as elastic material. Furthermore the earthpressures acting on the bucket foundation are disregarded. The interaction, friction, between the soil and the bucket foundation is as well not modelled, instead tie constraints will be applied. For further information about tie constraint see Section 6.3.5.

CHAPTER 4

BUCKLING OF SHELL STRUCTURES

In the following buckling of shell structures will be described. As a verification study for linerized prebuckling analysis utilizing FEA a concrete dome structure and cylinder shell and a bucket foundation made by steel will be analysed for linearized prebuckling analysis and the result will be compared with analytical solution, to check if there is agreement. The substructure will also be analysed for linearized prebuckling analysis. The concrete dome and the cylinder and bucket foundation will be considered at shell structures. In order to be defined as shell structures following guidelines are applied. For reinforced concrete shells the thickness to radius ratio is of about 1/200. For the substructure this will be used as a guideline since this will be a Compact Reinforced composite since the equivalent homogenous thickness is not known. For metallic shells the thickness to radius ratio is of about 1/300 [20, p. 12]. For shell structures it has to be checked if the buckling strength is much lower than the material strength. Therefore the design analysis of the shell structures should be checked for buckling analysis and static analysis. Furthermore the substructure is subjected to a wavepressure during the lifetime and internal pressures during installationproces, which can cause instability for the substructure. The negative internal pressure from the installation proces is not considered in this project due to limited time. A shell structure may undergo prebuckling, buckling and postbuckling deformation and this is sensitive to geometrical and loading imperfections. The geometrical imperfection corresponds to deviation of the middle surface from the perfect ideal shape of the shell structure. While loading imperfection is deviation of the magnitudes or direction of the loads [20]. In this project only the geometrical imperfection will be considered.

Due to the fact that there is no analytical solution for the prebuckling load for the particular substructure, the design approach will be based on FEA. The optional situation would be to find a analytical prebuckling load solution of the substructure and compare the result to FEA. Instead there has been done verifacation study of a dome structure, cylinder structure and bucket foundation, where analytical solution for prebuckling loads are known and these results have been compared with the result from the FEA of the structures. A buckling instability can be local or global. The buckling occurs in compressive parts of the structure. When buckling occurs there will be loss of global stiffness, and strain energy will be released and this is given by

$$U = \int_V \frac{1}{2}\sigma : \varepsilon dU \tag{4.1}$$

Where the strain energy is considered for the volume of the structure. In this project, time depended loading such as the wind and waves are considered to be static loadings. Due to the waves has amplitude the substructure could undergo oscillation, this could cause flutter, which is a elastic instability due to fluid mechanics from the waves and this is not considered in this project [20, p. 345].

Shells are never geometrical perfect by production, therefore a arbitrary critical imperfection will be introduced to the substructure. The linearized prebuckling analysis is a linear analysis. While postbuckling analysis is to check how the substructure responds to introduced imperfections and this is nonlinear analysis.

In this project it is chosen to check the linearized-eigenvalue prebuckling of the substructure and to invistigate if the linearized prebuckling load is more critical than the material failure. And if it is not the case a prebuckling mode will be applied as geometric imperfections and there will be performed material failure analysis, static analysis. If the linearized prebuckling load is critical a postbuckling analysis of the structure with imperfection will be performed. Ideal structures can loose their stabilities in one following types

- Bifurcation of equilibrium
- Limitation of equilibrium

In the following the overall description of these instabilities presented.

4.1 Introduction to instabilities

Bifurcation of equilibrium

A straight slender elastic column subjected to axial compressive force is used to illustrate the bifurcation of equilibrium. The load as a function of the axial displacement is shown in Figure 4.1a, when the column is loaded incrementally from 0 to 1 it reaches a critical point that is the bifurcation point. Until that the material is linear. From that point the path that will be choosen from the structure will correspond to minimum of total energy of the system. When the axial shortening is linearly proportion to the applied load this will be defined as the primary path and this is unstable due to the fact that when there is a small pertubation, this will bring the column to a bent position. If the path instead is from 1 to 3, this corresponds to the secondary path, where the column will acquire bent form and get lateral and axial deformation, this deformation is known as buckling. For this particularly column this is called as the Euler buckling load [20].

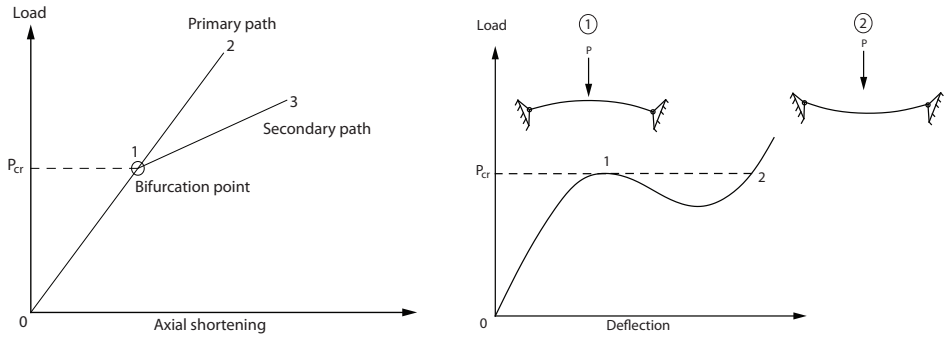

(a) Bifurcation of a column.

(b) Snap through of an shallow arc.

Figure 4.1: Instability of ideal structures.

Limitation of equilibrium

For the limitation of equilibrium the characteristic structures which carries the transverse loading mainly by compressive axial forces is the shallow arc and shallow shells. The shallow arc will be used as an example and can be seen in Figure 4.1b. One well known limitation of equilibrium instability is the snap-through buckling. The characteristic of the snap-through load-displacement curve is continous and has maximum and minimum points, and the critical load corresponds to one of these maxima. The shallow arc has restraint ends in the boundary conditions and is loaded with a vertical concentrated force in the middle of the arc and the displacement is as well taken from this point. When the load is increased incrementally from 0 to 1, the deflection will increase in the middle of the arc and this is shown in Figure 4.1b, at the maximum point 1 the arc will buckle and will deform reverse as shown in Figure 4.1b. This corresponds to that the load displacement path, goes directly to point 3 as shown with dotted lines. When the arc has snap-through buckled the compressive forces will be transformed into tensile forces. As shown for the snap-through buckling there exist no bifurcation points [20].

4.1.1 Linearized prebuckling analysis in FEA

Since only half of the substructure is going to be analysed in the linearized prebuckling analysis only the symmetric boundary condition is checked. As discussed in Section 1.5 the substructure is equivalent to a closed axisymmetric profile and therefore the bending and torsion are decoupled, and the loads are symmetric so there will occur no torsion of the substructure therefore the antisymmetric boundary conditions are not checked in this project.

In the linearized-eigenvalue prebuckling analysis the substructure will have no geometrical imperfection. In the linearized-eigenvalue prebuckling analysis the load for which the model stiffness matrix becomes singular is found, so the problem has nontrivial solution and the general form is given by

$$K^{MN} v^M = 0 \tag{4.2}$$

where K^{MN} is the tangent stiffness matrix when the load is applied, v^M is the nontrivial displacement solution i.e. the buckling mode [2]. In *Abaqus* following solution for the linearized prebuckling analysis is implemented

$$(K_0^{MN} + \lambda_i K_\Delta^{MN}) v_i^M = 0 \tag{4.3}$$

where K_0^{MN} is the stiffness matrix to the base state where the preloads, P^N is included. K_Δ^{MN} is the differential initial stress and load stiffness matrix from the incremental loading pattern Q^N. λ_i is the eigenvalue, v_i^M is the eigenvectors or eigenmmodes for buckling mode shapes. M and N are the degree of freedom of the whole model and i refers to the ith buckling mode [2]. The critical prebuckling load is therefore given by

$$P^N + \lambda_i Q^N = 0 \tag{4.4}$$

The linearized prebuckling analysis is used to find the critical buckling load of the stiff structure. The prebuckling modes v_i^M that are found from the linearized-eigenvalue prebuckling analysis are normalized vectors, and they do not represent actual magnitudes of deformations at critical loads. These are normalized so the ith maximum displacement components $U_{max,i}$ that has a magnitude of 1. In the linearized prebuckling analysis negative

eigenvalues are excluded since they have no physical meaning. Here is an example of why the negative eigenvalues are excluded in the linearized prebuckling analysis. In Figure 4.2 an example of a column that is simply supported at both ends shown where a compressive force P is applied and one end. If the negative eigenvalue is found for the load, it means that the prebuckling load P is in the opposite direction. This has no physical meaning because buckling only occurs in compressive forces and not in tensile forces.

Figure 4.2: Prebuckling of a column.

4.2 Geometrical imperfections from prebuckling modes

In order to check the nonlinear response of the substructure a geometric imperfection will be introduced. The geometry imperfections that can be applied in *Abaqus* are from the linearized prebuckling modes. It is always assumed that the lowest prebuckling modes gives the most critical prebuckling loads, in any case the geometrical imperfection can be introduced for the substructure in *Abaqus* as a linear combination of the prebuckling modes scaled with a associated scale factor to find the critical combination. In this project the 1st prebuckling mode is only utilized. The geometrical imperfection in *Abaqus* is given by

$$\Delta x_i = \sum_{i=1}^{M} w_i v_i^M \tag{4.5}$$

where w_i is the associated scale factor and is given by

$$w_i = \frac{u_{imp,i}}{U_{max,i}} \tag{4.6}$$

where $u_{imp,i}$ is the magnitude of imperfection that will be introduced in m. Usually the lowest prebuckling mode is going to be given with the largest scale factor. The magnitude of the pertubation is going to be a few percent of the shell thickness in this project. However the response of the substructure and the dome structure will be checked for increasing geometrical imperfection.

For non-linear analysis of the dome with a geometric imperfection, a *Static - General* method which is a $Newton - Rapson$ solver and *Static - Riks* which is a *arc*-length solver

will be compared to check if there are any differences in computational time. The difference between these solvers can be seen in Figure 4.3. When the incremental load is increased and the maximum load has been reached in the force-displacement curve, the *Static - General* method stops the analysis. While the *Static - Riks* method can analyse the unstabile response as shown.

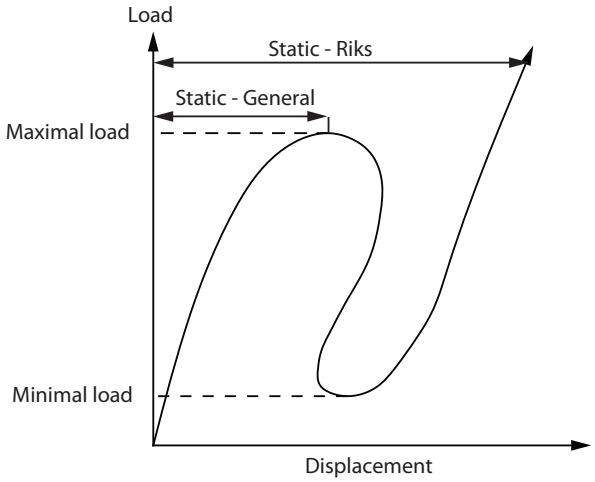

Figure 4.3: *Static - General* and *Static - Riks*.

The critical buckling load is reached when the negative eigenvalue emerges in the numerical analysis or when the strain energy has decreased. For the *Static - Riks* method a Load Proportionality Factor, LPF will be given at each increment, so when the instability occurs there will be negative eigenvalue that can be seen in the message file (.msg). The LPF is a scalar factor that is multiplied to the reference load vector and this is given by.

$$P_{total} = P_g + LPF(P_{ref} - P_g) \tag{4.7}$$

Where P_g is the dead load and P_{ref} is the reference load. When using *Riks*-method the instability manifest itself in a global load-displacement. The *Non-linear geometry* option is going to be used, so the significant geometry changes can be involved.

Approach to prebuckling and postbuckling analysis in FEA

The overall approach for the prebuckling analysis and non-linear analysis will be in *Abaqus*

- Linearized-eigenvalue prebuckling analysis by using the function *Linear pertubation:Buckle*. Here a displacement field for the prebuckling mode of the model saved to an result file (.fil) [5]
- Choosing random prebuckling modes as a linear combination of imperfection for the substructure by using the command in the input-file **IMPERFECTION* [5]
- A performance of the non-linear analysis of the structure with a geometric imperfection where the critical load is found

In general every time a load case is changed, a new prebuckling analysis has to be performed. The parameters that can be used to change the magnitude of the prebuckling eigenvalues are

- Thickness of the substructure
- The shape of the substructure
- The material of the substructure
- Load case

In FEA following parameters can change the values of prebuckling eigenvalues are

- Thickness of the substructure
- The shape of the substructure
- The material model
- Element type
- Mesh discretization
- Load case

CHAPTER 5
FINITE ELEMENTS FOR THE SOIL AND STRUCTURE

In the following the elements that are applied in this project described. Continuum element is applied for the soil, while curved shell element are applied for the substructure and bucket foundation.

5.1 Introduction to solid elements

The element type for the soil is chosen to be $C3D20R$. Where C stands for continuum, 3D for 3 dimensional, 20 for 20 nodes and R for reduced integration. In the following why this type of element is chosen from the element library in *Abaqus* described.

In Figure 5.1 a 3D continuum element that consists of 3 degrees of freedom at each node shown, and these are the translational degrees of freedom as shown. In the figure the global coordinate system (x,y,z) can also bee seen.

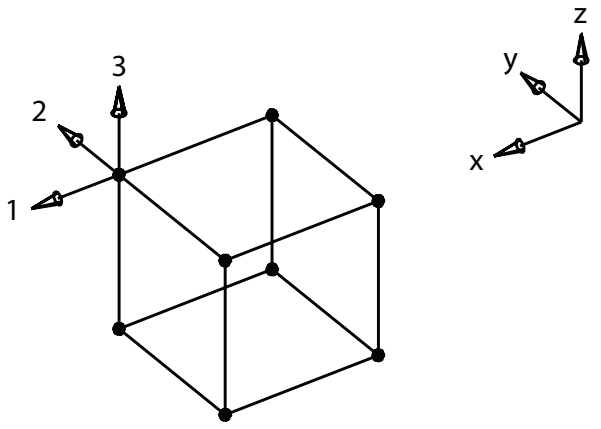

Figure 5.1: Degrees of freedom for 3D continuum element.

In Figure 5.2a the 20 nodes of the element can be seen and in Figure 5.2b the integration points for the element can be seen for the face that is on the bottom. This element consist of the 9 integration points at each face.

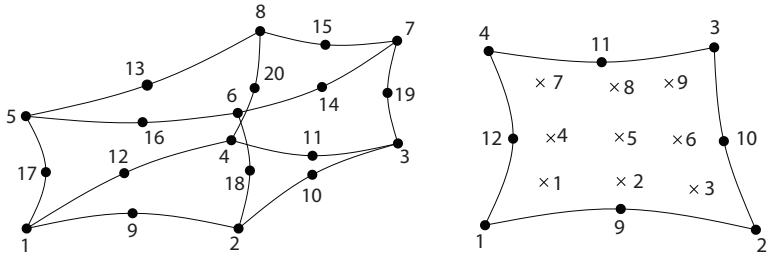

(a) Nodes of the C3D20R.

(b) Integration points for the C3D20R.

Figure 5.2: Nodes and integration points for the C3D20R element [3].

When using solid-elements following considerations should be taken into account. First linear elements will be described and then the quadratic elements will be described.

Linear element

According to [7, chapter 4.1] there are some restrictions which should be considered when working with linear, fully integrated and reduced integrated elements when they are subjected to bending moments. This problem is called shear locking. Even though that there is no bending in soil, why shear locking occurs will be described. Full integration refers to the number of Gauss points required to integrate polynomials terms. In Figure 5.3 a small piece of a material which is subjected to a pure bending is considered and the deformation is shown. As it can be seen to the right the material has deformed in a constant curve, where the sides remain orthogonal to each other at the corners. Out of the plane the lines remain straight lines.

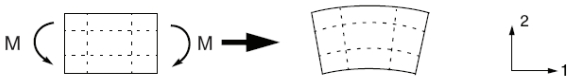

Figure 5.3: A material subjected for pure bending.

For linear fully integrated and reduced integrated elements following respons occurs due to pure bending moment. For the first case the situation can be seen in Figure 5.4.

Figure 5.4: Fully integrated element subjected to pure bending.

In Figure 5.4 it can be seen that there are no curvature of the material. The integration points are placed where the dotted lines crosses together. The corners are no longer orthogonal which suggests that shear stresses σ_{12} exist in the integration points. This do not happen for the real material because the material is subjected only to pure bending. Instead the upper line have extended suggesting that there exist tension σ_{11}. The bottom line has been compressed where there is a compression σ_{11}. Assuming that the length of the dotted lines have small displacement there are no transverse stresses σ_{22}. Because the edges can not curve shear deformation is created from the strain energy and thereby shear stresses σ_{12}. So the overall deflection is small because the element is too stiff to deform. Although the elements works perfectly in direct or shear loads.

For the linear reduced integration element there is no deformation at all and this can be seen in Figure 5.5.

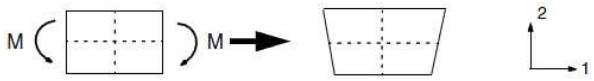

Figure 5.5: Reduced integrated element subjected to pure bending.

The dotted lines have not deformed nor changed length, this means that there exist no stresses at all. In addition there exist no strain energy from the element distortion because it can not resist this type of deformation mode and therefore it has no stiffness in this mode.

In general if a quadratic material unit element is subjected to a shear load at the top corner edge to the right, it will deform as shown with dotted lines.

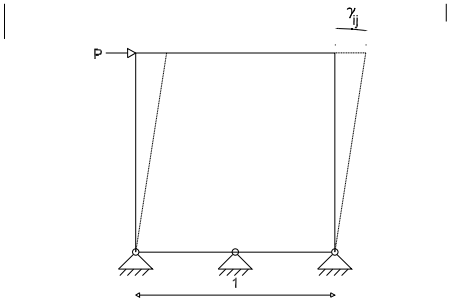

Figure 5.6: Distortion of a quadratic element.

The dimensions of the edges are unchanged but the angle between the edges are no longer perpendicular. This type of deformation is called distortion, this is also defined as angular strain by

$$\gamma_{ij} = 2 \cdot \epsilon_{ij} \tag{5.1}$$

where ϵ_{ij} is the shear strain.

Quadratic element

For the Quadratic fully and reduced integration elements the response is different than the linear elements. For the quadratic fully integrated element it can bend as the material element behavior shown in Figure 5.3. However there can also exhibit some locking in distortion and bending stress. For the quadratic reduced integrated elements there are no problem at all as long as the finer mesh is applied in the width and length direction. Therefore these elements are generally the best solution for most stress-displacement analysis. But care should be taken when the analysis is with large-displacement involving large strains and in some type of contact analysis.

5.2 Reinforced concrete shell by FEA

In the following the curved shell element that is applied in the project going to be presented and for the modeling of the substructure and bucket foundation a curved shell element will be utilized. First a general approach how the displacements are defined described for an curved shell-element. Afterwards the curved shell-element that is applied in this project presented.

When using shell elements there are some considerations which should be taken into account, and these will now be presented. In Figure 5.7 the degrees of freedom for the shell element is shown and this has six degrees of freedoms at each node, and these are the translational degrees of freedom and rotational degrees of freedom. The rotational degree of freedom in the plane θ_3 is called the drilling degree of freedom and this is shown in the figure. Sometimes the drilling dof is not included. The translational degrees of freedoms in the plane v_1 and v_1 are shown. The translational degree of freedom out of the plane is given by v_3. The rotational degrees of freedoms out of the plane are give by θ_1 and θ_2. In curved shell element the membrane and bending forces are coupled together.

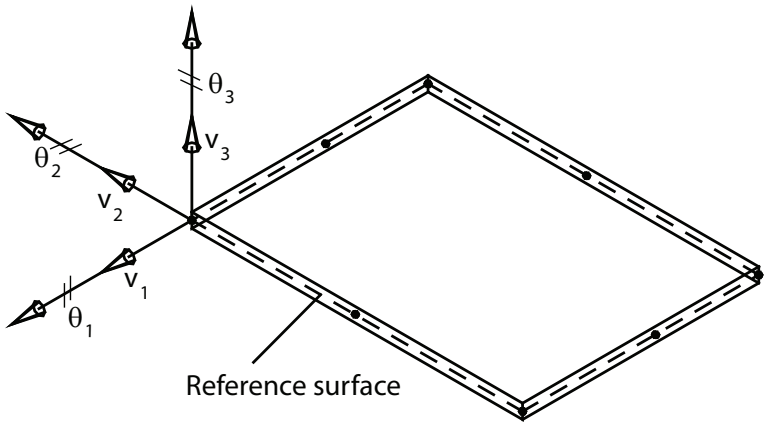

Figure 5.7: Curved shell elements with degrees of freedoms and 8 nodes.

In the figure the reference surface is also showed as dashed lines, the reference surface is defined by the nodes. All the kinematic quantities, including the elements area, the mechanical response by specifying the thickness, material direction, orientation of the surface, rebar layers, *Abaqus* will determine the equivalent section properties in that surface. If nothing else is mentioned, the reference surface will be defined as midsurface in this project.

There are two types of shell elements in *Abaqus/CAE* which can be applied, these are the thin shell element and the thick shell elements. The kinematic relations of the thin shell elements are based on Kirchoff theory, while the kinematic relations of the thick shells are based on Reissner-Mindlin theory. In general the thin shell elements neglect the shear flexibility, while the thick shell elements include the shear flexibility.

5.2.1 Introduction to curved shell-element

Firstly a 20 noded continuum element can be seen in Figure 5.8a and this have 3 degrees of freedom, dof, at each node and these are (u, v, w). If the substructure, the bucket foundation and the soil were modeled by using continuum element infinite numbers of dof in the model would have been applied and this is computational expensive. To avoid this instead curved shell element will be applied to the substructure and bucket foundation.

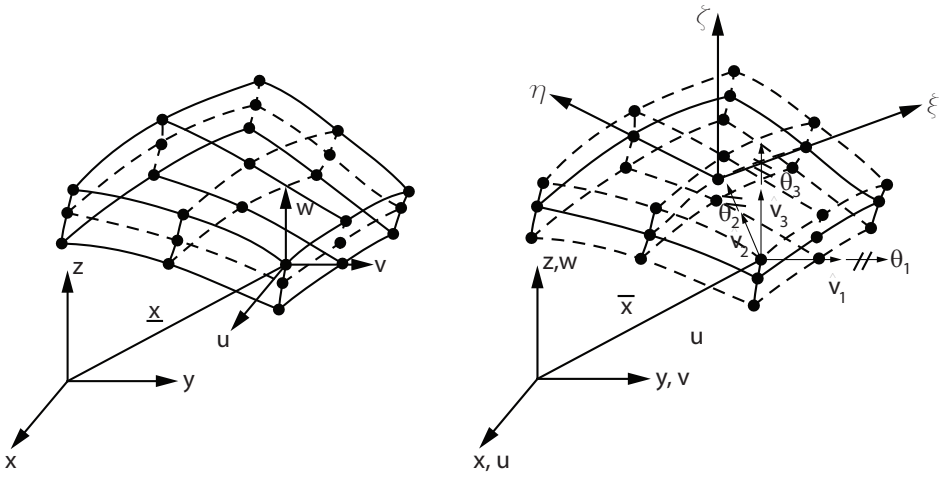

(a) 3D-continuum element with dof. (b) Curved shell element.

Figure 5.8: Mindlin-Reissner element versus shell element.

In Figure 5.8b a curved shell element with 5-6 dof at each node is shown, and these are (u, v, w, θ_1, θ_2, θ_3) and these are defined in the midsurface. Furthermore the isoparametric coordinate system (ζ, η, ξ) is shown in the midsurface where ζ and η are in the plane of the shell element and ξ normal to the surface. ζ, η and ξ are homogenous coordinates i.e. they are normalized to the interval $[-1; 1]$. All dof are defined in the midsurface, therefore the amount of nodes are reduced significantly when compared to a 20 noded continuum element. The coordinates on the mid-plane from the global coordinate system (x, y, z) can be described by

$$\bar{x_i} = \bar{x_i}(\xi, \eta) = \sum_{k=1}^{n} x_i^k f^k(\xi, \eta) \tag{5.2}$$

where x_i^k are the node coordinates of the n nodes. $f^k(\xi, \eta)$ are the two-dimensional Langrangian shape functions that will also be used to interpolate the displacement field, this leading to an isoparametric element. The coordinates at an arbitrary point is found by

$$x_i = x_i(\xi, \eta, \zeta) = \sum_{k=1}^{n} \bar{x_i}(\xi, \eta) + \zeta \frac{t}{2} \hat{V}_{3i}^k) \Rightarrow \tag{5.3}$$

$$x_i = x_i(\xi, \eta, \zeta) = \sum_{k=1}^{n} f^k(\xi, \eta)(x_i^k + h(\zeta)\hat{V}_{3i}^k) \tag{5.4}$$

where $\hat{V}_{1i}$ is the approximate unit normal to the mid-plane. $\hat{V}_{1i}^k$ is the value of $\hat{V}_{1i}$ at node number, k. $\hat{V}_{2i}$ is the approximate unit normal to the mid-plane. $\hat{V}_{2i}^k$ is the value of $\hat{V}_{2i}$ at node number, k. $\hat{V}_{3i}$ is the approximate unit normal to the mid-plane. $\hat{V}_{3i}^k$ is the value of $\hat{V}_{3i}$ at node number, k.

$h(\zeta) = \zeta \frac{t}{2}$ is the thickness shape function, where t is the homogenous thickness that is constant over the element. Displacement at an arbitrary point is therefore found by

$$u_i(\xi, \eta, \zeta) = \bar{u_i}(\xi, \eta) + \zeta \frac{t}{2}(-\theta_1(\xi, \eta)\hat{V}_{2i}(\xi, \eta) + \theta_2(\xi, \eta)\hat{V}_{1i}(\xi, \eta)) \Rightarrow \tag{5.5}$$

$$u_i(\xi,\eta,\zeta) = \sum_{k=1}^{n} f^k(\xi,\eta)(u_i^k + h(\zeta))(-\theta_1^k \hat{V}_{2i}^k + \theta_2^k \hat{V}_{1i}^k) \tag{5.6}$$

where $\hat{V}_{1i}$, $\hat{V}_{2i}$ and $\hat{V}_{3i}$ form an orthogonal basis. u_1^k, u_2^k, u_3^k, θ_1^k and θ_2^k are variables in the kth node. The displacements and rotations are defined above and are described in the mid-plane of the shell-element. With these the the strains can be found. Then by applying kinematic relation the stresses will be found with a given constitutive model.

Curved shell element in Abaqus

For the shell sections following modeling technique for the reinforced concrete is applied in *Abaqus*. A shell structure has a significantly smaller dimension in the thickness direction than the other two dimensions. Following shell sections is used.

- Homogenous shell sections

Homogenous shell sections, are defined by a shell thickness, a section Poisson's ratio, rebar layers and a given material model from the reference surface of the shell element.

From the element library in *Abaqus* S8R-element is chosen, in the following why this type of shell-element is chosen described. The structures that are going to be analysed in this project are mainly curved structures, therefore it is preferable to apply a curved shell-element in this project, for this purpose $S8R$ fulfills the criterion. In the S8R- shell element the bending and the membrane forces are coupled together.

- S8R, 8-noded doubly curved thick shell, where reduced integration is used and quadratic interpolation is applied

Shear locking

When linearized prebuckling analysis of the dome and substructure are going to be performed the deformation of the shell elements will be out of plane due to the prebuckling modes. In Figure 5.9a a Mindlin plate with reduced integration is shown and this is subjected to pure bending, it responds properly when looking at a small qudratic element because this has not deformed. When looking at Mindlin plate with full integration and this is subjected to a pure bending as shown in Figure 5.9b, there will be no bending of the element, due to distortion of the element, there will be shear locking of the element [18, p. 325-328].

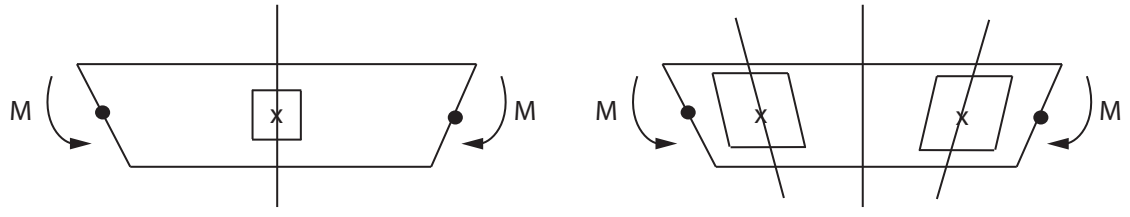

(a) Mindlin plate with reduced integration.

(b) Mindlin plate with full integration.

Figure 5.9: Mindlin plates with reduced and full integration.

5.3 Local coordinate system for the shell-element

In this project a rebar layer for the dome structure with a spherical coordinate system (R, T, P) and for the substructure with a cylindrical coordinate system (R, T, Z) will be introduced. These coordinate systems are defined in Appendix A. The rebar layer in the dome will have a constant spacing while the substructure will have an angular spacing. The rebar layers are defined in a combination with the global coordinate system and the local coordinate system for the shell element. In general a local coordinate system in shell element exist with the following axis (1,2,n), where n is a normal to the reference surface. The local coordinate system is given by the right-hand rule. Stresses and strains will be defined in a local coordinate system. A positive normal direction n is defined as the face SPOS, while the negative direction of the normal n is defined as face SNEG. A positive and negative directions are also used to designate the top and the bottom of the surface then specifying the offsets of the reference surface from the midsurface.

5.4 Defining rebar layer in shell-section

In the following the rebar layer definition in the shell element will be introduced. The geometry for the rebars is defined as layers of uniformly spaced reinforcing bars in shell elements. Whatever this is a contant spacing or an angular spacing, the rebar layers are treated as a smeared layer with a constant thickness, t, equal to the area of each reinforcing bar A divided by the reinforcing bar spacing s, $t = A/s$, and it stiffened in the longitudinal rebar direction. The smeared rebar layer is illustrated in Figure 5.10.

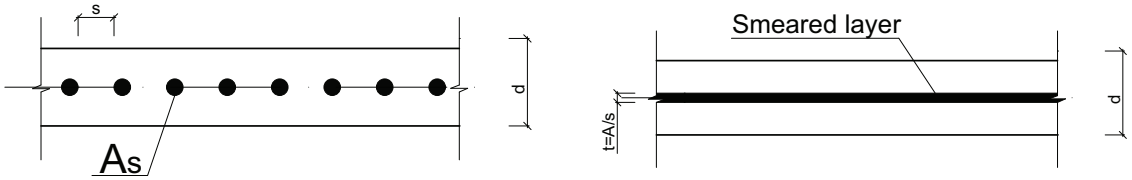

(a) Actual rebar definition in section.

(b) Smeared layer in section, in *Abaqus*.

Figure 5.10: Rebar definition.

The geometry of a rebar is always defined in the local coordinate system.

5.4.1 Rebar layer with constant spacing

The rebars with constant spacing are going to be applied for the dome structure in Section 6.1. An example of a rebar layer for a shell element can be seen in Figure 5.11a with constant spacing where the local coordinate system $(1, 2, n)$ coincides with the global coordinate system (R, T, P). In general the rebars will have the orientation of an angle α_R and it is measured on the midsurface of the shell. This particular example has a rebar layer orientation of 0^o, it can be seen in Figure 5.11. The rebar layer position is defined with the distance of h_1 from the midsurface in n direction. The thickness of the shell element h is defined in the section property and not by the nodes. When a rebar has been assigned the material becomes orthotropic in one or more directions.

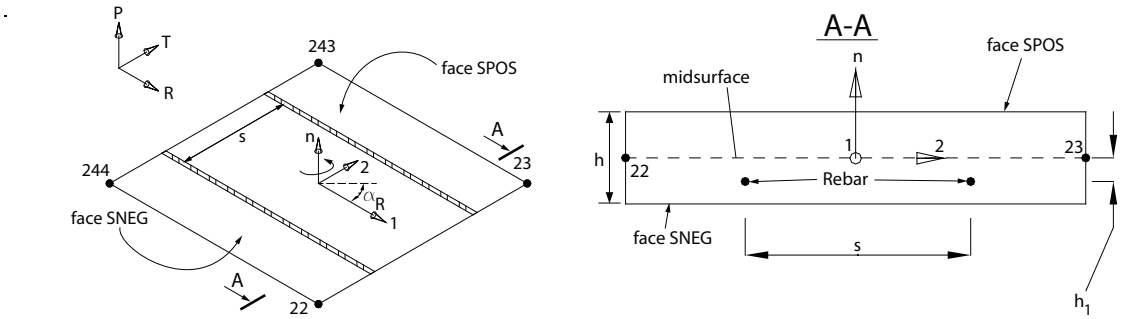

(a) Shell element with local coordinate system and rebar layer.

(b) Section A-A, rebar layer.

Figure 5.11: Rebar layer in shell element.

5.4.2 Rebar layer with angular spacing

The rebar layer that is going to be applied for the substructure is shown in Figure 1.7. How it is applied in the substructure will be presented in the following. The rebar layer arrangement with the local coordinate system (1, 2, n) can be seen in Figure 5.12. The rebar in the direction of 2 will be defined as meridional rebar and the rebar in the direction of 1 will be defined as circumferencial rebar. A rebar layer is defined in the model with an angular spacing in *Cylindrical coordinate system*. Meridional rebar is defined with the angular spacing α, the circumferential rebar is defined with the angular spacing β, it can be seen in Figure 5.12. The arc length between two individual meridional rebar can be calculated using expression

$$L = \alpha r \tag{5.7}$$

where L is the arc length, α is the angular spacing between meridional rebars, r is the radius at the particular place where the rebar is defined. In the same way the arc length betweeen two individual circumferential rebar is calculated by

$$L = \beta r \tag{5.8}$$

where, β is the angular spacing between circumferential rebars. With the definition of the local coordinate system (1, 2, n) the rebar layer direction, α_R, for the meridional rebar corresponds to 90^o, while the direction of the rebar layer for the circumferencial rebar is 0^o.

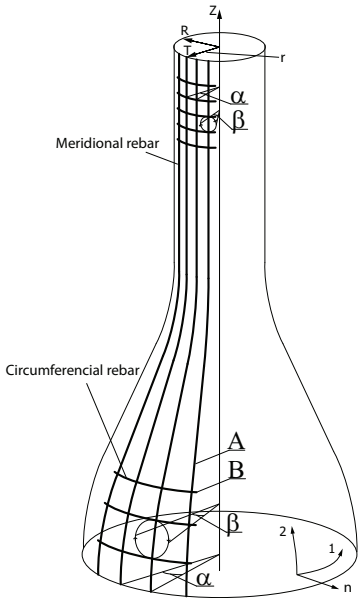

Figure 5.12: Rebar layer in substructuret model.

In Figure 5.13 a magnification of the rebar layer from Figure 5.12 can be seen.

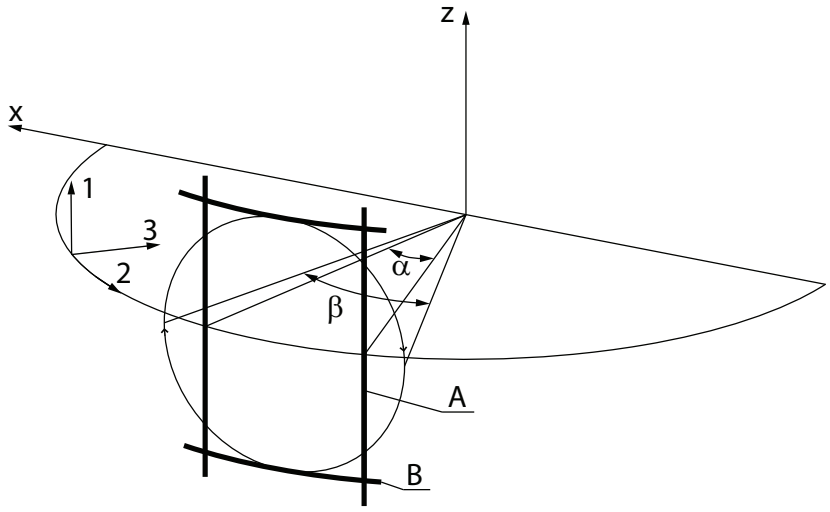

Figure 5.13: Definition of the rebar.

Isoparametric and skew rebars can be used in three dimensional shell and membrane elements. It should be noticed that rebars can not be applied in triangular shells or membranes [1, chap. 2.2.4]. This is one of the reasons why the elements will be kept as quadratic. In Figure 5.14a an example of isoparametric rebars that are aligned along the mapping of constant isoparametric lines in the element is shown. When an element contains rebar as shown in the figure and this is not distorted, each opposite edges will be parallel and the direction of the rebar will not change. However if an element is distorted as shown in Figure 5.14b all the edges will not be parallel and the rebar directions are different at each integration points within an element. The dashed line presents the rebars.

If the edges of the element containing the rebar are not parallel, the number of actual rebars with this spacing passing through one edge will be different than the number passing through the opposite edge.

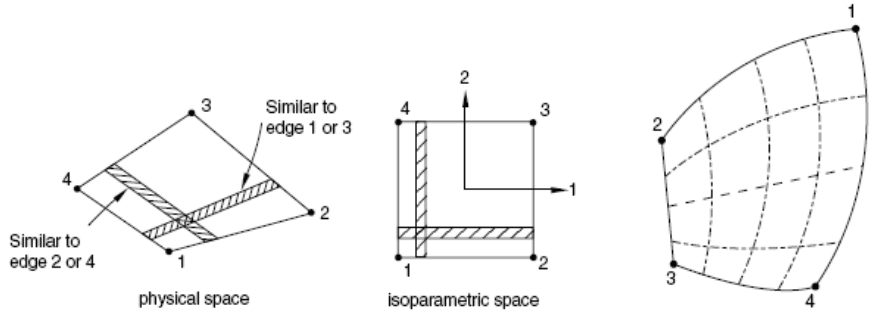

(a) Isoparametric rebar in an undistorted three dimensional shell or membrane element.

(b) Rebar layer.

Figure 5.14: Distorted rebar layer [chapt. 2.2.4][1].

5.4.3 Integration points for the S8R-element

In this project shell sections integrated during the analysis will be applied in the linearized prebuckling analysis and to the non-linear analysis. Even though that there is no plasticity in the linearized prebuckling analysis the integration during analysis is used in *Abaqus*. When the integration before analysis was checked the rebar layer could not be defined in the linearized prebuckling analysis, therefore the integration during analysis chosen.

Integration through the thickness

The numbering of sections point through the thickness are consequently started with point one. Section point one is at the bottom surface if Simpson's rule is used, and if Gauss quadrature is applied the point is closest to the bottom surface. The bottom surface is the SNEG face. In *Abaqus/CAE* the limit of section points through the thickness is 15 points for Gauss quadrature. In Figure 5.15, the number of section points for 7, 16 and 20 can be seen. The dashed line represents the half of the unit height. As it can be seen, if more section points are applied in the thickness the first and last points gets closer to the surfaces.

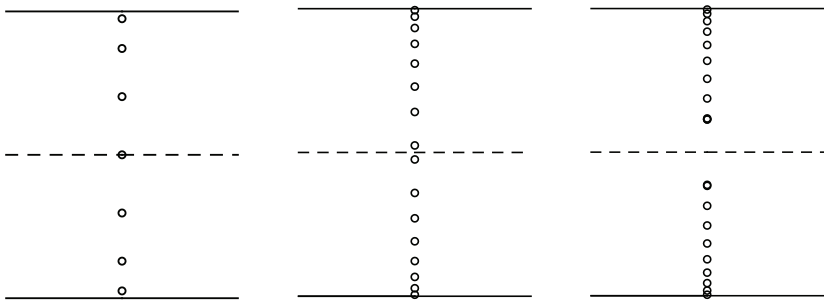

(a) 7 section points.

(b) 16 section points.

(c) 20 section points.

Figure 5.15: Gauss quadrature integration through thickness with section points through a unit height.

In Figure 5.16 the Simpson integration through a unit thickness can be seen, the amount of section points are always given in uneven numbers in *Abaqus/CAE* and are limitless when

compared with Gauss quadrature. With uneven numbers there is always a section point in the middle of the height.

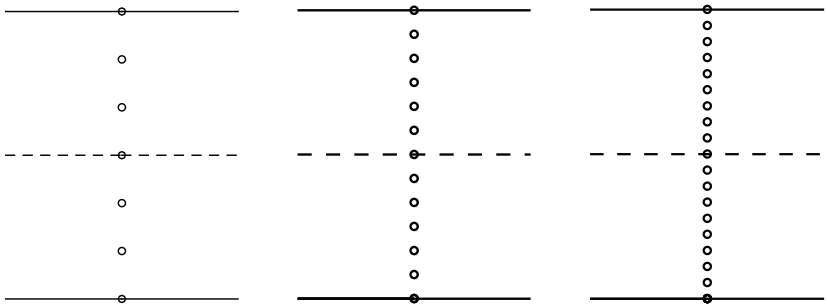

(a) 7 section points. (b) 17 section points. (c) 21 section points.

Figure 5.16: Simpson integration for section points through a unit height.

Integration points in the planar dimension of S8R

When the stress distribution is going to be checked through the thickness of the shell element these will be evaluated from the integration points. The section forces will be found in the midsurface, the neutral axis for the shell element. In *Abaqus/CAE* Gauss quadrature is used.

In Figure 5.17 an example of S8R shell element with four integration points and with four Simpson section points is shown. In Figure 5.17a S8R shell element with four integration points is shown with isoparametric coordinate system with (ξ,η), the node numbers can also be seen. As it can be seen, the distance from the center of the isoparametric coordinate system to the integration point, the distance is always $\frac{1}{\sqrt{3}}$ whenever if the distance is from the ξ or η and regardless if it is in the positive or negative direction. The node numbers are not in sequence due to the fact this is an example how to define the numbering of integration points. The lowest node number is integration point one, and the rest are in sequence

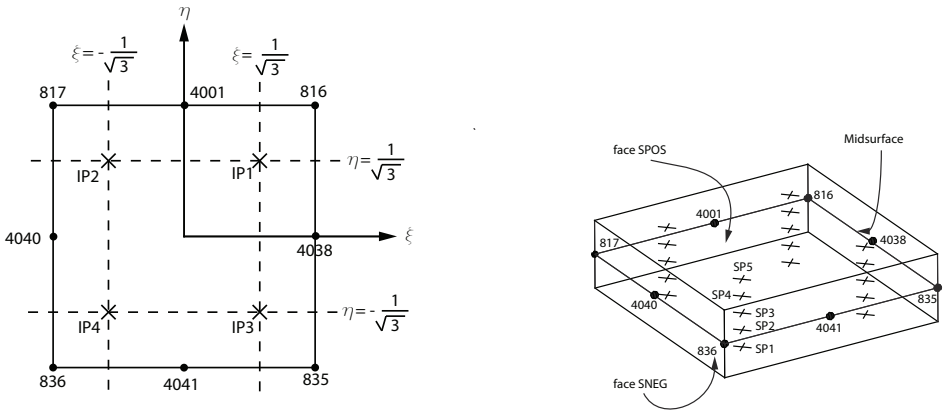

(a) Placement of Gauss points [19].

(b) Integration points and section points throught the thickness.

Figure 5.17: Integration points in four noded shell element.

In Figure 5.17b an example with five section points is shown with the use of Simpson integration rule. The midsurface, SPOS and SNEG can as well be seen.

CHAPTER 6

VERIFICATION STUDY OF PREBUCKLING ANALYSIS OF SHELL STRUCTURES

In the following the analytical solution of the prebuckling load and prebuckling load utilized by FEA of a dome structure, a cylinder and a bucket foundation will be compared to check if the results are in good agreement, when these analysis have been performed a conclusion of the verification study will be described in the end of this chapter. There has only been done a non-linear analysis of the dome with geometric imperfection.

6.1 Prebuckling load of a perfect dome structure

In the following a dome structure will be analysed to find the prebuckling load by an analytical solution and FEA results. These will then be compared to check if there are any differences. First how the analytical prebuckling load is found presented and next the prebuckling load found by means of FEA shown. The load that is going to be applied is a uniform pressure, i.e. load that is normal to the surface and can be seen in Figure 6.1, therefore only compressive forces will be generated in the dome.

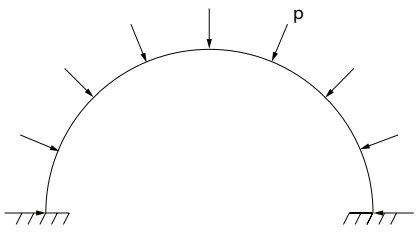

Figure 6.1: Uniform pressure load applied to the dome.

A pure concrete dome structure will be analysed and even though there are no tensile forces in the dome structure there will be analysed a dome with different rebar arrangements in the FEA. This is to check if the linearized prebuckling eigenvalues changes and if the prebuckling modes changes. Afterwards a geometric imperfection will be introduced in one of the reinforced concrete domes, and the response will be analysed when the imperfection is increased.

Forces in a dome

A dome structure is a thin curved shell of revolution, where the generating curve is the meridian. In a thin dome the material is stressed in three-direction, due to the fact that the dome combines structural actions of an arch and a slab. The shape of the dome provides strength against the self-weight. The loads in the dome are carried mainly by compressive and tensile forces and the moment and shear forces are neglicible [22, p. 251-269]. In Figure 6.2 the forces acting in the dome structure can be seen and these are the meridional forces and the hoop/ring forces. The meridional forces are in the generating curve direction, while the hoop forces are in the arbitrary point on the meridian which formes a circle in the dome.

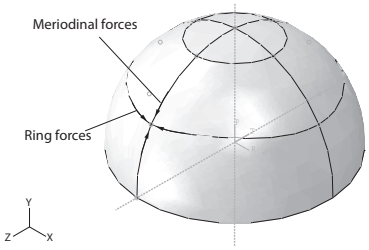

Figure 6.2: Forces in a dome structure.

Dome geometry

The dome that is going to be analysed is a hemi sphere and in Table 6.1 the following geometries can be seen. In Figure 6.3a the geometries can be seen

Table 6.1: Dome geometry parameters [22].

R	t	$\frac{t}{R}$
$[m]$	$[m]$	$[-]$
6	0.04	0.007

where, R, is the radius of the dome and t, is the thickness of the dome. The thickness and radius ratio can as well be seen. And this thickness to radius ratio is close to 200. So the dome can be regarded as an shell structure. In FEA the midsurface is going to be the radius of the dome.

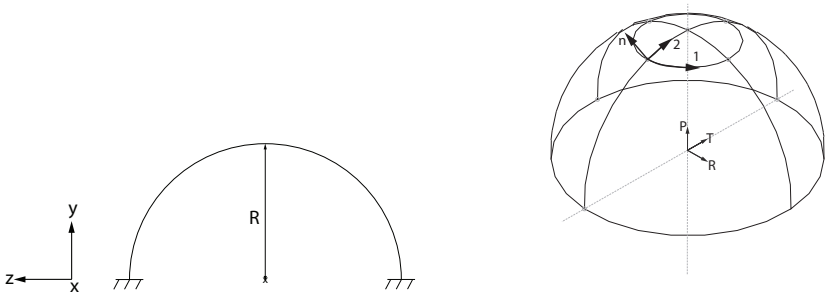

(a) Geometry parameters of the dome.

(b) Coordinate system for the dome.

Figure 6.3: Dome geometry.

The dome will be clamped at the boundary. The spherical coordinate system can be seen in Figure 6.3b with (R, T, P). The spherical coordinate system is places in the center of the hemi sphere and the spherical coordinate system is described in Appendix A. The material local orientation is shown as well (1, 2, n). The rebar directions and the boundary conditions will be assigned in the spherical coordinate system. With these geometries the dome will be analysed to find the prebuckling load.

Material properties of concrete

The following material properties that are going to be applied in the analysis for the concrete can be seen in Table 6.2. First in the linearized prebuckling analysis only the elastic properties will be applied. For the non-linear analysis with geometric imperfection the compressive strength of the concrete of 155 MPa will be applied, but in this particular analysis the material will be considered as isotropic.

Table 6.2: Material properties for the concrete dome and steel for the rebar.

f_{yk}	E_c	ν_c	E_c
$[MPa]$	$[GPa]$	$[-]$	$[GPa]$
155	44	0.23	210

6.1.1 Analytical solution for prebuckling load of dome

The analytical solution for the hemi spherical shell the following critical prebuckling load formula has been applied for a isotropic material [20, p. 369]

$$p_{cr} = \frac{2}{\sqrt{3(1-\nu_c^2)}} E_c \left(\frac{t}{R}\right)^2 \tag{6.1}$$

where R is the radius of the dome, t is the thickness of the dome, ν_c is the Poisson's ratio and E_c is the Young's modulus.

The result for the critical prebuckling load for the concrete, $p_{cr,concrete}$ can be seen in Table 6.3 by using Table 6.1, Table 6.2, and (6.1).

Table 6.3: Result for analytical prebuckling load of dome.

$p_{cr,concrete}$
$[MPa]$
2.32

This result will be used to normalize the results for prebuckling load of the domes found by means of FEA.

6.1.2 FEA for the linearized prebuckling load of dome

In Figure 6.4 the mesh discretization that is used for the dome in FEA can be seen. The elements are kept as quadratic as possible. There have not been peformed convergence analysis for the linearized prebuckling eigenvalue, 2800 elements have been applied to the dome, 5 section points are used, due to the fact this is an linearized prebuckling analysis. Simpson integration rule is applied through the thickness and integration during analysis is

applied. Integration before analysis could not be applied in the analysis because if the this was chosen, the rebar layer could not be defined. Therefore integration during analysis is applied even though this is an linear analysis. S8R-elements are applied.

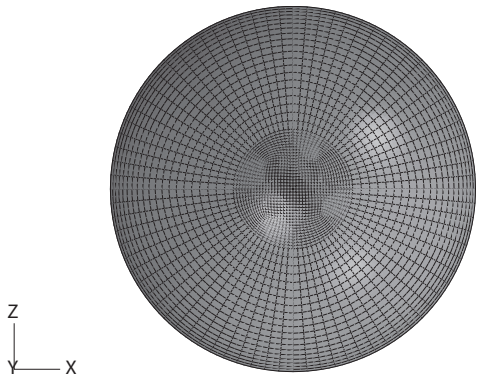

Figure 6.4: Mesh discretization for the dome.

Rebar layer arrangement of different domes

There are three different rebar arrangements that will be checked for the linearized prebuckling load analysis of the domes and these are as follows. A dome with no reinforcement will be defined as dome 1. A dome with reinforcement in local rebar one-direction will be defined as dome 2 and this is shown in Figure 6.6a, these will be defined as ring rebars. A dome with reinforcement in local rebar two-direction will be defined as dome 3 and this is shown in Figure 6.6b, where these will be defined as meridional rebars. The fourth rebar arrangement is the combination of dome 2 and dome 3 and this will be defined as dome 4 as shown in Figure 6.6c. These domes are checked to see if the linearized prebuckling of the domes changes when the rebar has been applied. The distance between the rebars is, $c - c$. The diameter of the rebar is given the parameter, ϕ_{st}. In Table 6.4 the distance of the rebars and the diameter can be seen.

Table 6.4: Rebar distance and diameter of rebar of the dome.

$c - c$	ϕ_{st}
$[mm]$	$[mm]$
200	10

The spacing between the rebars is based on [17, p. 265] where it is recommended for reinforced concrete shell that the minimum nominal reinforcement in compression zone should consists of 10 mm rebars with c-c=200 mm and the maximal spacing of the rebars should be 5 times the thickness of the shell. The cross-section of dome 4 can be seen in Figure 6.5. For dome 2 and 3, the rebars will be placed in the midsurface.

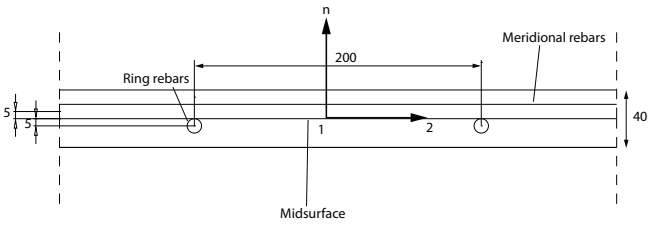

Figure 6.5: Cross-section of the shell dome.

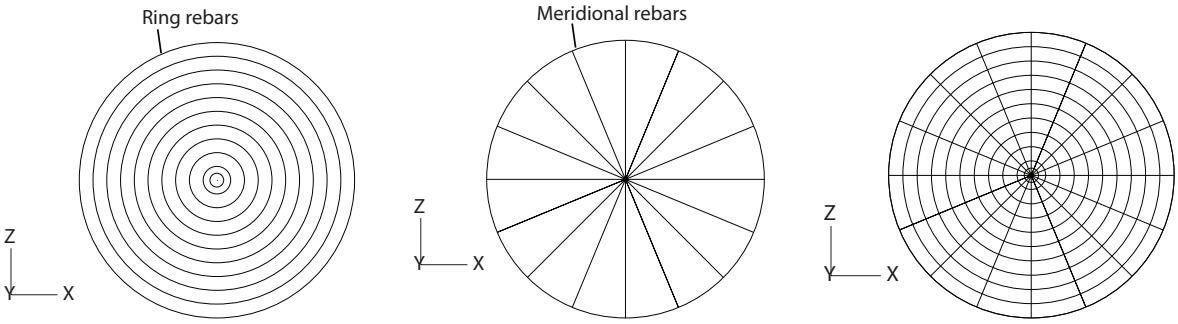

(a) Dome 2. (b) Dome 3 . (c) Dome 4 .

Figure 6.6: Domes with rebar layers.

To find the linearized prebuckling load of the domes, the option *Linear pertubation:Buckle*, has been applied in *Abaqus*. The linearized prebuckling eigenvalue λ_B is found from the analysis. A pressure load, q_l, of 2.06621 MPa is applied at the surface of the dome as shown in Figure 6.1. When the linearized prebuckling eigenvalue has been found the prebuckling load is calculated by multiplying the linearized eigenvalue with the applied pressure load and this is given by

$$p_B = \lambda \cdot q_l \tag{6.2}$$

Linearized prebuckling eigenvalues from FEA

The linearized prebuckling eigenvalues of the concrete domes can be seen in Table 6.5. The 5 lowest linearized eigenvalues are shown for each dome. As it can be seen the eigenvalues are closely spaced, this indicates that the domes are geometric imperfection sensitive. As it can be seen the two first linearized eigenvalues,λ_1 and λ_2, are the same for each dome. This says that they have the same linearized prebuckling mode, thus the second linerized prebuckling mode is rotated. For dome 1, two following linear eigenvalues also are equal ,λ_3 and λ_4, again one of the linearized prebuckling mode is rotated. When comparing the linearized eigenvalues to each dome type, these values are nearly identical. The reason why, is that it's a linear analysis therefore the cross-sectional area of the dome is increased by the factor of $\alpha = \frac{E_s}{E_c}$. Whereas the rebar area is transformed into an equivalent concrete area. But since the rebar layer is defined in the neutral plane, the second moment of inertia will not be increased as if the rebar was distributed in two rebar layers [26]. The prebuckling load is then found by applying (6.2). Only the first linearized eigenvalue is applied.

Table 6.5: The linearized eigenvalues of the domes.

	Dome 1	Dome 2	Dome 3	Dome 4
λ_1	1.1147	1.1234	1.1253	1.2328
λ_2	1.1147	1.1234	1.1253	1.2328
λ_3	1.1159	1.1274	1.1301	1.2339
λ_4	1.1159	1.1234	1.1307	1.2328
λ_5	1.1180	1.1283	1.1307	1.2351

As it can be seen in Table 6.5, the difference between the linearized prebuckling eigenvalues for the domes are very low, so the rebars do not change the linearized prebuckling eigenvalues for the domes. The biggest eigenvalue is for the dome 4, which has the biggest amount of rebar, and the smallest is for dome 1, which has no rebar layers at all. When comparing dome 2 and dome 3, the meridional rebars gives relatively bigger eigenvalue.

Linearized prebuckling load of the domes

The prebuckling load then becomes based on (6.2)

Table 6.6: Buckling load for the first buckling mode in [MPa].

	Dome 1	Dome 2	Dome 3	Dome 4
$p_{cr,FEA}$	2.303	2.321	2.325	2.547

6.1.3 Prebuckling modes of the domes

In the following the first prebuckling modes of the domes are now shown. Even though that the linearized prebuckling eigenvalues are relatively close to each other, the prebuckling modes are different. The first prebuckling mode of dome 1 can be seen in Figure 6.7.

(a) Isometric view. (b) Top view.

Figure 6.7: First prebuckling mode of dome 1.

The first prebuckling mode for dome 2 can be seen in Figure 6.8

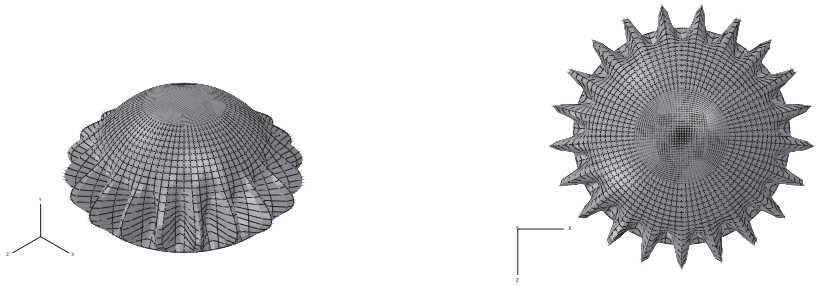

(a) Isometric view. (b) Top view.

Figure 6.8: First prebuckling mode of dome 2.

The first prebuckling mode for dome 3 can be seen in Figure 6.9

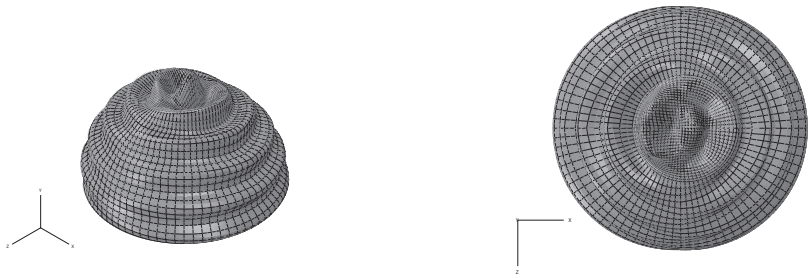

(a) Isometric view. (b) Top view.

Figure 6.9: First prebuckling mode of dome 3.

The first prebuckling mode for dome 4 can be seen in 6.10

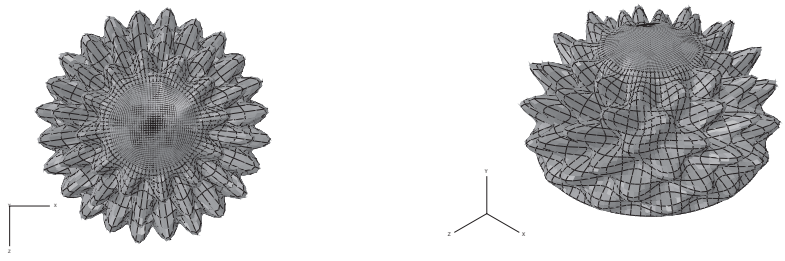

(a) Isometric view. (b) Top view.

Figure 6.10: First prebuckling mode of dome 4.

When comparing the first prebuckling modes of the domes, when looking at Figure 6.7, Figure 6.8 these have the same prebuckling modes and with same amount of ripples. The prebuckling modes of dome 3 and dome 4 differs from the prebuckling mode for dome 2 and dome 3. The prebuckling mode of dome 4 in Figure 6.10 is a combination of prebuckling modes of dome 2 and dome 3.

6.1.4 Comparison of analytical and FEA solution for prebuckling load of domes

These results are then normalized by applying the result from the analytical solution from Table 6.3, and this can be seen in Table 6.7

Table 6.7: Linearized prebuckling load by FEA normalized by analytical prebuckling load.

Dome 1	Dome 2	Dome 3	Dome 4	Dome 5
0.993	1	1.02	1.098	1.062

For the pure concrete without reinforcement, the result from the FEA is a bit lower than the analytical result. This could be because the analytical solution is not exact. And if coarser mesh was applied, the prebuckling eigenvalues would have been much higher and therefore the response of the structure would have been stiffer because it would not describe the real geometry.

6.2 Analysis of dome 4 with geometric imperfection

It is chosen to analyse dome 4 when geometric imperfection is applied and this will now be described. A geometric imperfection that will be applied with using the first prebuckling mode of the dome. Due to the fact that this result is in good agreement with the analytical result for the prebuckling load. The applied load is the prebuckling load $p_{cr} = 2.54714$ MPa. In the analysis the *Static - General* and *Static - Riks* will be used and compared to each other to check if there are any differences. The *Non-linear geometry* function is applied during the analysis. In the analysis with the geometrical imperfection equal to zero, only 62 percent of the prebuckling load could be applied to the model. So the material strength was more critical than the prebuckling load of the structure.

The step increments of 0.01 has been applied for the *Static - General*, for the minimum and maximum increment. If higher increments were applied in the step, there would be negative eigenvalues for much lower load increment and this would not correspond to the expected response of the structure. For the *Static - Riks* analysis the initial and maximal arc length increment of 0.05 and rhe estimated total arc length of 0.5 is used. The reason why these were applied in the *Abaqus* is that the results became similar to the results from *Static - General*.

The normalized maximum displacement for prebuckling mode 1 was found to be $U_{imp} = 1.204$ and this can be seen in Figure 6.11a. In the figure the maximum normalized displacements with the red colour can be seen. The reason why this value is not equal to one, is that the maximum normalized displacement is found in the geometry where the biggest displacement is. It is not in the nodes, but somewhere in the middle of the element, it is illustrated in Figure 6.11b.

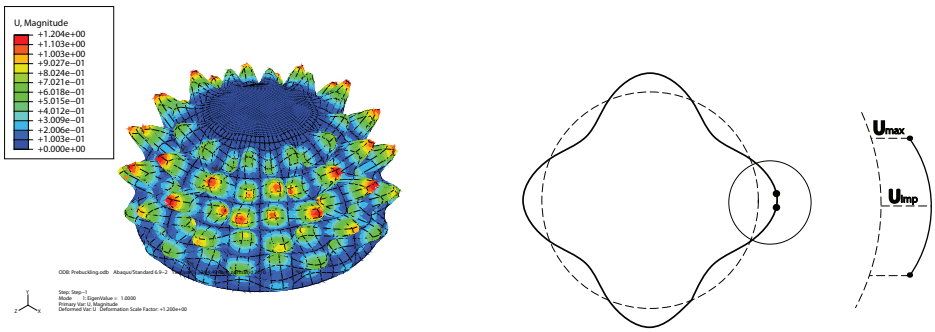

(a) Results from *Abaqus*.

(b) Example of normalized displacement.

Figure 6.11: Normalized maximum displacement in dome 4.

The imperfections that are going to be applied shown in Table 6.8. The associated scaling factor that is going to be applied to the geometric imperfection is found by (4.6).

Table 6.8: Imperfection and scaling factors for dome 4.

Imperfection	Scaling factor
$[mm]$	$[m]$
2	0.00166113
4	0.003322259
8	0.006644518
16	0.013289037
32	0.026578073
64	0.053156146
128	0.106312292
256	0.212624585
512	0.425249169
1024	0.850498339

An example of strain energy development for the imperfection of 2 mm for the *Static - Riks* analysis can be seen in Figure 6.12. As it can be seen, the strain energy increases until the maximum energy is reached, in that point the first negative eigenvalue appears in the message file (.msg). This is due to the fact that the structure becomes instabile. After that the strain energy decreases. If *Static - General* is used, the analysis will stop when the maximum strain energy is reached and this is shown in the figure.

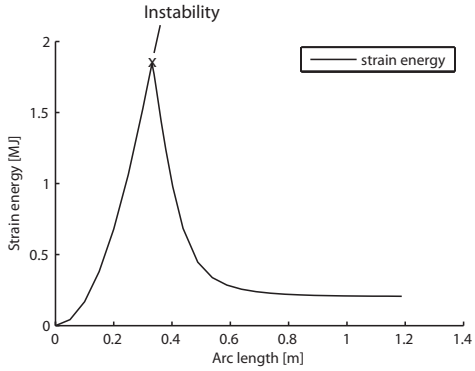

Figure 6.12: strain energy respons from *Static - Riks* analysis.

An example of plastic strains of a dome with imperfection of 256 mm can be seen in Figure 6.13. When the imperfection deformation of dome 4 is compared with the normalized maximum displacement (Figure 6.11a) a good agreement is obtained.

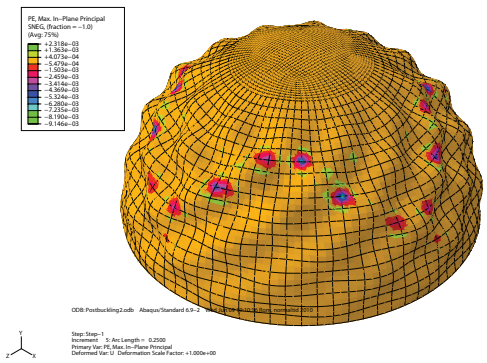

Figure 6.13: Dome 4 with the imperfection of 256 mm.

In the following the computational time of the analysis for the two solvers will be compared. An imperfection of 2 mm was used, because this imperfection was the smallest in this analysis and therefore would take longest in computational time. The results can be seen in Table 6.9.

Table 6.9: Computational time for dome 4 in [s].

Static - General	*Static - Riks*
1620.5	371.8

As it can be seen in the table, the computational time for the *Static - Riks* is about 4.3 faster than the *Static - General*.

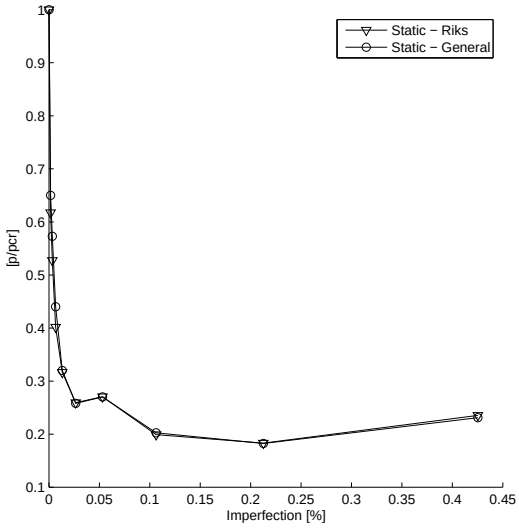

Figure 6.14: Decrease of the load capacity as a function of imperfection of the dome.

As it can be seen in Figure 6.14, the *Static - General* and *Static - Riks* are in good agreement. It is observed that even with small imperfection of geometry, the load capacity of the dome rapidly decreases, it means that the dome is imperfection sensitive. And this can also be confirmed by looking at the linearized eigenvalues in Table 6.5, because they are closely spaced. The largest value of imperfection of 1024 mm from Table 6.8 was checked but the analysis was aborted due to distortion of the element and that the element stiffness was changed.

6.3 Prebuckling load of perfect cylindrical shells

In the following two different sized perfect shape cylinders and cylinders with the lid (bucket foundations) will be analysed to find the prebuckling load. Analytical solution will be compared with FEA. Afterwards the difference between the prebuckling load of a cylinder and a cylinder with the lid will be compared.

Bucket geometry

Two perfect cylindrical shells will be analysed with geometries given in Table 6.10, the geometry set can be seen in Figure 6.15

Table 6.10: Cylinder geometry parameters [28].

Cylinder	L	D	t_s
$[-]$	$[m]$	$[m]$	$[mm]$
A	6	12	30
B	12	12	30

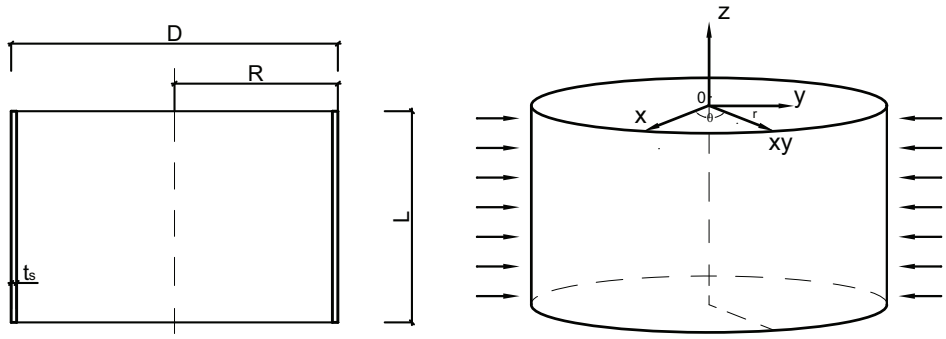

(a) Geometry parameters of cylindrical shells.

(b) Coordinate system of cylindrical shells.

Figure 6.15: Geometry of the cylindrical shells.

As it can be seen in Figure 6.15b the cylindrical coordinate system is used and it is placed in the upper part of the center line. The cylindrical coordinate system is described in Appendix A. The pressure load is applied in radial direction using cylindrical coordinate system. By using these geometry parameters the prebuckling load of the cylinders will be found.

Material properties for steel

The material properties that are going to be used for the cylinder and bucket foundation can be seen in the Table 6.11. The elastic properties are only applied since this is a linearized prebuckling analysis

Table 6.11: Material properties for the cylindrical shells [28].

E_s	ν_s
$[GPa]$	$[-]$
210	0.3

6.3.1 Analytical solution for the prebuckling load of perfect cylindrical shell

The prebuckling load of cylindrical shells loaded with hydrostatic pressure are highly dependent on boundary conditions. As following the prebuckling load for a cylindrical shell will be investigated. The pinned boundary condition at the lower and upper end of the skirt is used. The classical linear prebuckling load expression is [28]:

$$P_{PP} = \alpha P^0_{PP} \tag{6.3}$$

where α is a factor that is dependant on the boundary conditions [34] in this case $\alpha = 1$. Because pinned boundary conditions are applied in both ends. P^0_{PP} is given by

$$P^0_{PP} = \frac{\pi^2 E_s t_s^3}{12(1-\nu_s^2)L^2 R} P^*_{PP} \tag{6.4}$$

where R is the radius of the cylinder, E_s is the modulus of elasticity and ν_s is the Poisson's ratio. P^*_{PP} is a non-dimensional buckling pressure which fits to a cylindrical shell such as bucket foundation, and this is given by

$$P^*_{PP} = 2\sqrt{\frac{8Z}{3\pi^2}} \tag{6.5}$$

where Z is the Batdorf parameter, and this takes the height of the cylinder into account, radius, thickness of the skirt and Poisson's ratio are used to classify the geometry of the cylindrical shell and this is given by

$$Z = \frac{L^2}{Rt_s}\sqrt{1-\nu_s^2} \tag{6.6}$$

By using the analytical formulas the results of prebuckling load of perfect cylinders can be seen in the Table 6.12.

Table 6.12: Analytical solution for prebuckling load of perfect cylindrical shells.

Cylinder A $[kPa]$	Cylinder B $[kPa]$
340.5	170.3

It can be observed from the results that with a higher cylinder, the prebuckling load gets lower because the stiffness of the cylinder gets lower with increasing hight.

6.3.2 Linearized Prebuckling load of a perfect cylindrical shell by FEA

The two cylindrical shells A and B will be analysed by FEA in order to get a prebuckling load. A three dimensional, finite element model was created using *Abaqus* software. The cylinders were created by using S8R shell elements, the uniform pressure of 100 kPa has been applied in polar direction in the cylindrical coordinate system. The boundary conditions are pinned at both ends, so the radial and polar directions are contrainted. In Figure 6.16 the mesh discritization can be seen. The elements are made as quadratic mesh. No convergence analysis of the eigenvalues has been performed, it is assumed that the mesh discretization is enough.

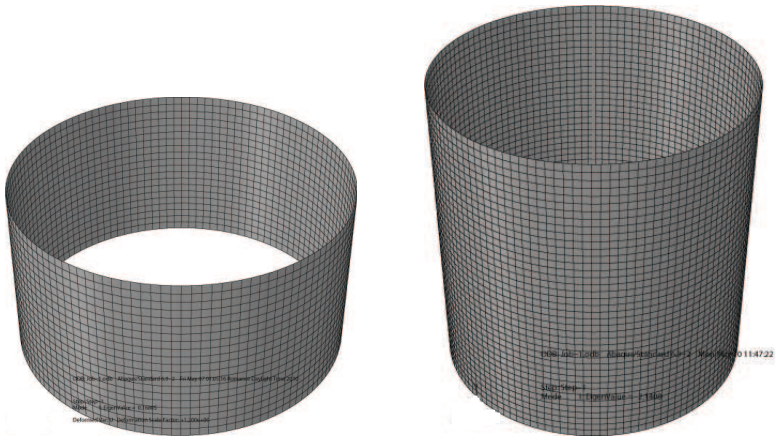

(a) Cylinder A. (b) Cylinder B.

Figure 6.16: Mesh of Cylinders.

Linearized prebuckling eigenvalues for the cylinders by FEA

The most critical results of the first linearized eigenvalues from the cylinders can be seen in Table 6.13.

Table 6.13: The first linearized eigenvalues of the cylinders.

Cylinder A	Cylinder B
3.718	1.777

It can be obtained from Table 6.13, that when the height of a cylinder increases the smaller linearized eigenvalue is obtained.

Linearized prebuckling load of the cylinders

The obtained linearized eigenvalues were multiplied with the applied uniform pressure load, and the results are given in Table 6.14.

Table 6.14: Linearized prebuckling load of the cylinders by FEA in [kPa].

	Cylinder A	Cylinder B
P_{cr1}	371.8	177.7

Linearized prebuckling modes of the cylinders

The first linearized prebuckling modes are shown in Figure 6.17.

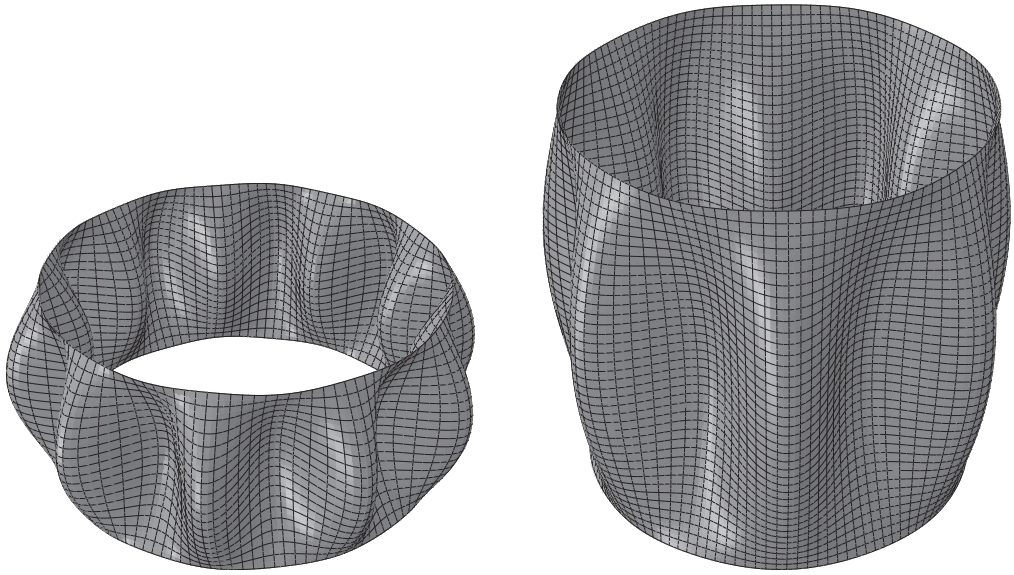

(a) Cylinder A. (b) Cylinder B.

Figure 6.17: Prebuckling of cylinders, first eigen mode.

For cylinder A there are 10 ripples while in cylinder B there are 7 ripples.

6.3.3 Comparison of analytical and FEA solution for prebuckling load of cylinder

In the following the analytical solution for the prebuckling loads and the results from the linearized prebuckling mode will be compared. The FEA results will be normalised by the results from the analytical solution and the result can be seen in Table 6.15.

Table 6.15: Linearized prebuckling load by FEA normalized by analytical prebuckling load.

$Cylinder A$	$Cylinder B$
1.092	1.043

It can be seen from Table 6.15 that the analytical prebuckling load solution and FEA solutions for the cylinder A and B are in a good agreement. There is a slight difference because the analytical solution might be not exact.

6.3.4 Linearized prebuckling analysis of bucket foundation by FEA

The difference between the cylinder and the bucket foundation is that the lid is placed on one end of the skirt. The significance of the applied lid will now be checked to see how much it will change the linearized prebuckling load. The thickness of the lid is chosen to be the same thickness as for the cylinder and is assembled with the cylinder. The material properties are given in Table 6.11. *Tie constraints* are used to assemble the skirt with the lid. Again at the end of the skirt pinned boundary condition is applied.

6.3.5 Tie constraints

In *Tie constraint* the connections become rigid when the rotational degrees of freedom and translational degrees of freedom are tied. In order to apply the tie constraint a master

and slave surfaces has to be defined. An example of a 2 dimensional beam which has to be assembled is shown in Figure 6.18. In a contact place where two parts are connected a master and slave surfaces must be defined. A master surface can be defined by using following criterions, if a bigger surface contacts a smaller surface, the smaller surface should be defined as a slave surface. If this criterion can not be applied then the master surface should be applied to the one with the stiffer body or to the one with the coarser mesh. As it also can be seen in Figure 6.18a, the master surface has a different mesh discretization than the slave part, therefore the connections will not share the same nodes. This is not wishful, if there for example exist a large deformation of the parts then the master surface is forced to deform not in its nodes. If the master surface and the slave surface have the same mesh discretization they will share the same nodes at the connections, see Figure 6.18b [1].

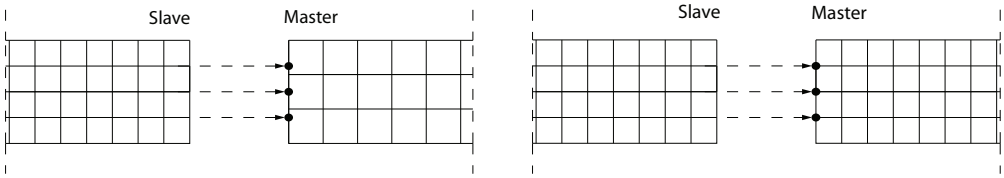

(a) Master surface and slave nodes with different discretization.

(b) Master surface and slave nodes with same discretization.

Figure 6.18: Node-to-surface contact discretization, master surface and slave nodes of a beam.

So the lid is chosen to be the master surface and the skirt as the slave surface. The analysis was performed for a bucket A and B with the lid, these will be defined as the bucket foundation A and the bucket foundation B.

Linearized prebuckling eigenvalues for the bucket foundations by FEA

The results for the linearized prebuckling eigenvalues can be seen in Table 6.16 for the bucket foundations. The lowest linearized eigenvalues are presented so they can be compared with the result for the linearized prebuckling eigenvalues for the cylinders by FEA.

Table 6.16: The first linearized eigenvalues of the cylinder with a lid.

Bucket foundation A	Bucket foundation B
3.769	1.786

Linearized prebuckling loads for the bucket foundations by FEA

The linearized prebuckling loads are given in Table 6.17.

Table 6.17: Linearized prebuckling loads of bucket foundation by FEA in [kPa].

	$BucketA$	$BucketB$
P_{cr1}	376.9	178.6

It can be seen from Table 6.14 and Table 6.17 that the prebuckling load for the first eigenvalue is increased around 1.014 and 1.005 times of cylinders A and B respectively, it is clear that the results are almost the same, it means that instead of using the lid as the part in *Abaqus* it is easier to define pinned boundary condition at each end.

Linearized prebuckling modes of the bucket foundation

The first linearized prebuckling modes are shown in Figure 6.19.

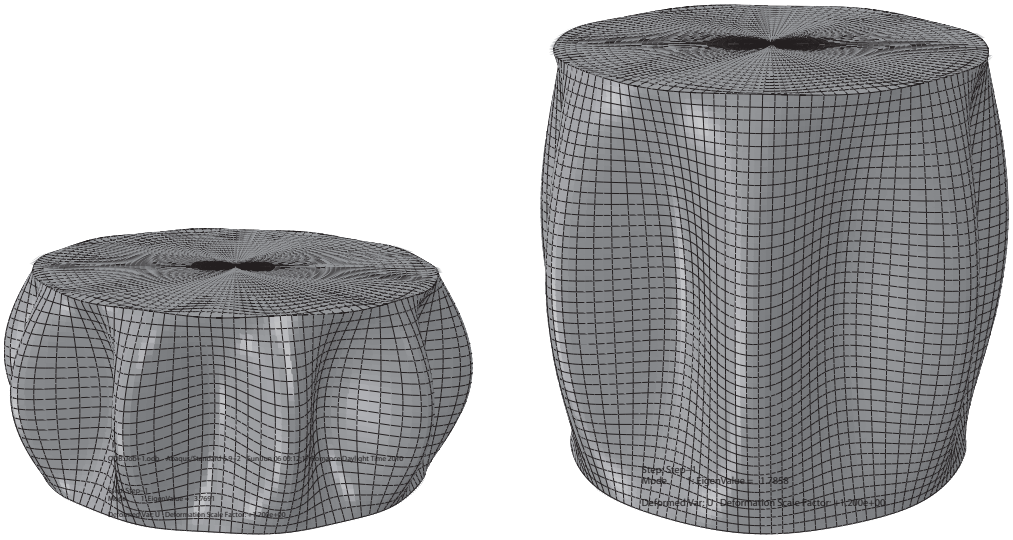

(a) Bucket foundation A. (b) Bucket foundation B.

Figure 6.19: Prebuckling of bucket foundation, first eigen mode.

There has been observed 10 ripples in bucket foundation A and 7 ripples in bucket foundation B, these are the same amount of ripples that was observed for the cylinder shells previously. It can also be seen that there is small deformation of the lid, this is because the same thickness was applied for the skirt and lid.

6.4 Conclusion of verification study

When compared analytical solution and FEA for prebuckling load the differences are small. It has been obtained that with increase of the cylinder height, the prebuckling load decreases. While comparing cylinder prebuckling load and the same cylinder with the lid, the prebuckling load does not increase, because the upper skirt part pinned boundary condition for the cylinder was used and it restrained the skirt in the xy plane the same way as it did the lid.

It has been obtained that the analytical solution and FEA for prebuckling load of a dome has a really good agreement, added reinforcement doesnt have very big influence for the prebuckling load, although prebuckling modes changes dramatically. While analysing dome using static analysis, even a small imperfection has a very big influence on the dome. It is due to the fact that when a dome is as a perfectly shaped structure, only axial forces act, but when even a small imperfection is introduced bending moments occur on the structure and bearing capacity decreases.

CHAPTER 7

HYDRAULIC PRESSURE DISTRIBUTION ON THE SUBSTRUCTURE

The purpose of this chapter is to determine the hydraulic pressure that is going to be applied to the substructure in FEA. The hydraulic pressure is included due to the geometry of the substructure, and also that there might be buckling risk. In this project wind load and the self-weight are given, while the wave data is not given. Therefore when the hydraulic pressure has been defined, the total force from the pressure will be calculated to determine the magnitude and to check if the result are realistic. This total force will give a contribution to the moment at the bucket foundation, while the rest will be from the wind force. Furthermore it will be checked how much forces the hydraulic pressure contributes to the substructure, and this will be done by applying the pressure and comparing it when the pressure is not applied.

The pressure distribution will be based on potential theory and the placement of the seperation points will be assumed in the cylinder. The total force per length will be found from the assumed pressure distribution, and compared with the Morison's equation, this is to check if there is an agreement between those. The velocity potential that is going to be applied is for the undisturbed flow. Following forces are not considered in this project, splashing, wave run-up and short term loading.

7.0.1 Wave motion

To find the wave pressure distribution acting on the substructure that is generated from the waves the following approach has been done. First how the surface variation, horizontal particle velocity and the horizontal particle acceleration have been defined is shown, from these variations, the worst pressure distribution acting to the substructure will be found. First the basic conditions will be presented based on [9]. Long crested waves are considered where the linear wave theory based on Stokes 1st order theory is applied and this is only valid for non-breaking waves with small amplitudes. This wave theory is simplest to implement in *Abaqus* to check if the new substructure has buckling risk from hydraulic pressure combined with the wind force and self-weight of the offshore wind turbine. The Stokes 1st order theory is based on Laplace equation and Bernoulli's equation, they are used to derive the wave motions. The following boundary conditions are used

- The waves are periodic
- A particle at surface remains at surface

- The pressure at the water surface is equal to the atmospheric pressure
- The vertical velocity is zero at the bottom

In the following the assumption that the waves are periodic will be accepted (in reality the waves are not periodic), since this is an invistigation of checking if it is possible to make the substructure by using CRC.

The velocity potential that is going to be applied for the uniform flow and for undisturbed flow is in the limit of $\frac{D}{L} < 5$. Where it is assumed that the wave particle velocity and acceleration are constant in that range.

$$\varphi_o = g_o cos(\omega t - kx) \tag{7.1}$$

where g_o is given by

$$g_o = \frac{ag}{\omega} \frac{cosh(k(z+h))}{sinh(kh)} \tag{7.2}$$

where a is the amplitude of the wave, g is gravity acceleration, k is the wave number, h is the wave height and ω is the cyclic frequency.
This is a simplification of the wave potential because this will be a disturbed flow due to the substructure and furthermore the velocity potential will be found inside the substructure see Figure 7.1. The flow potential is defined in the coordinate system as shown and the flow potential found in this project when $x = 0$.

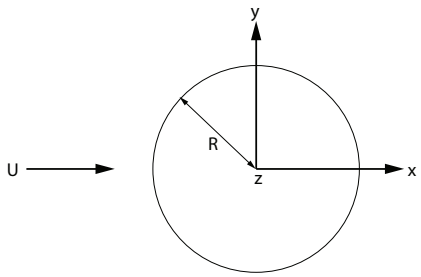

Figure 7.1: Flow potential for the undisturbed flow.

The horizontal particle velocity u_x is defined by

$$\frac{\partial \varphi_o}{\partial x} = u_x = \frac{agk}{\omega} \frac{cosh(k(z+h))}{cosh(kh)} sin(\omega t - kx) \tag{7.3}$$

The surface elevation is given by

$$\eta = \frac{H}{2} sin(\omega t - kx), H = 2a \tag{7.4}$$

The cyclic frequency is given by

$$\omega = \frac{2\pi}{T} \tag{7.5}$$

where T is the wave period. The wave number is given by

$$k = \frac{2\pi}{L} \tag{7.6}$$

The dispersion relationship has been used to find the wavelenght and this is given by

$$L = \frac{gT^2}{2\pi} tanh\left(\frac{2\pi h}{L}\right) \tag{7.7}$$

Due to the fact that there has not been performed extreme data analysis to find the wave height, (H) and wave period (T) these values have been determined based on [25, p. 2913], where it is assumed that the current and wave loads have a magnitude around 2 MN $\pm$ 1 MN for a monopile, and the wave period is assumed to be 10 s.

Table 7.1: Properties of the wave mechanics.

Property		*Value*
T	Wave period	10 s
ω	Cyclic frequency found by (7.5)	0.63
h	Water depth	20 m
γ_w	Density of the salt water	1025 kg/m^3
L	Wavelength according to (7.7)	121.32 m
k	Wave number according to (7.6)	0.052
H	Wave height	12 m
g	Gravity	9.82 m/s^2

The maximum wave height that can occur for a certain water depth is assumed to be given by $H_{max} = 0.6H$ [9]. The variation of the surface by applying (7.4), and the variation of the velocity of the particle by applying (7.3) and the variation of the acceleration by applying (7.36) are depicted in Figure 7.2.

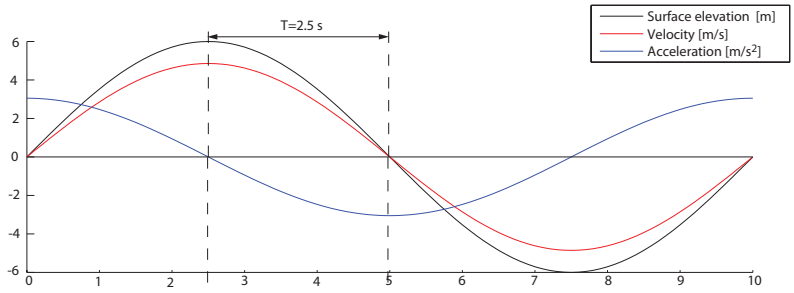

Figure 7.2: Variation of the surface elevation, velocity and the acceleration of a particle.

As it can be seen, the surface variation and the velocity of the particle are in phase of each other, while the acceleration of the particle is out of phase with 2.5 s.

7.0.2 Hydraulic pressure

In the following how the hydraulic pressure is found based on linear wave theory and potential theory will be presented. The hydraulic pressure distribution that is going to be considered in this project is a static pressure. Even though that in reality this is as dynamic pressure

distribution. Again this is an invistigation checking if it is possible to make a substructure made in CRC.

An axample of the hydraulic pressure distribution over the depth for the substructure can be seen in Figure 7.3a, the pressure is normal to the surface of the substructure. In order to have an idea of the magnitude of the total force acting on the substructure in Figure 7.3a the hydraulic pressure distribution acting on the substructure is simplified by partitioning the substructure as cylinder strips per meter over the height z. By doing that the total force can be found. This is a simplification of the hydraulic pressure, but as mentioned, this gives an idea of the total force acting on the substructure.

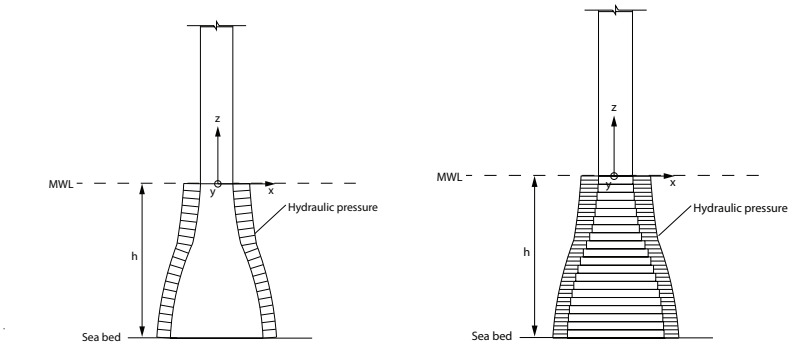

(a) Hydraulic pressure distribution.

(b) Simplification of the substructure.

Figure 7.3: Hydraulic pressure distribution over the height of the substructure.

The total pressure that will act on the substructure consists of the following contributions

$$p_{total} = \overbrace{p_h(z)}^{Hydrostatic} + \overbrace{p_d(R,\theta,z,t,a,\omega,h) + p_M(R,\theta,z,t,a,\omega,h)}^{Dynamic} \tag{7.8}$$

where $p_h(z)$ is the hydrostatic pressure distribution and is a function of the depth. For the dynamic pressure distribution, this consist of two parts and these are the $p_d(R,\theta,z,t,a,\omega,h)$, which is the drag pressure and $p_M(R,\theta,z,t,a,\omega,h)$ - the inertia pressure. The inner part of the substructure will be filled in with salt water so there will be no pressure difference from inside and outside the substructure. So the hydrostatic pressure will not be included in the analysis.

These pressure distributions will be applied into the *Abaqus* model by using the *Analytical field* function. Both hydraulic pressure distributions are based on potential theory. Next how the hydraulic pressure distributions are found described and first how the drag pressure is found presented and afterwards how the inertia pressure is found will be described.

7.1 Drag pressure distribution

Drag pressure distribution from potential theory

In the following the drag pressure distribution that is going to be applied in the substructure in *Abaqus* model will be presented. The drag pressure distribution will be based on potential theory. The pressure distribution p_c' from the potential theory for a cylinder can be seen in Figure 7.4a where the direction of the uniform flow U, the radius of the cylinder R, the cartesian coordinate system is shown (x,y,z), the height of the structure is in the z-direction.

The polar coordinate system (r, θ) is also shown. The positive sign is for compressive pressure and the negative sign is for suction pressure. In potential theory the velocity of the uniform flow has a low velocity. Therefore there are 2 stagnation points, and they are placed in the flow direction in front and back of the cylinder. There are no vortices behind the cylinder because the velocity is slow. The drag pressure distribution is symmetric to x-axis.

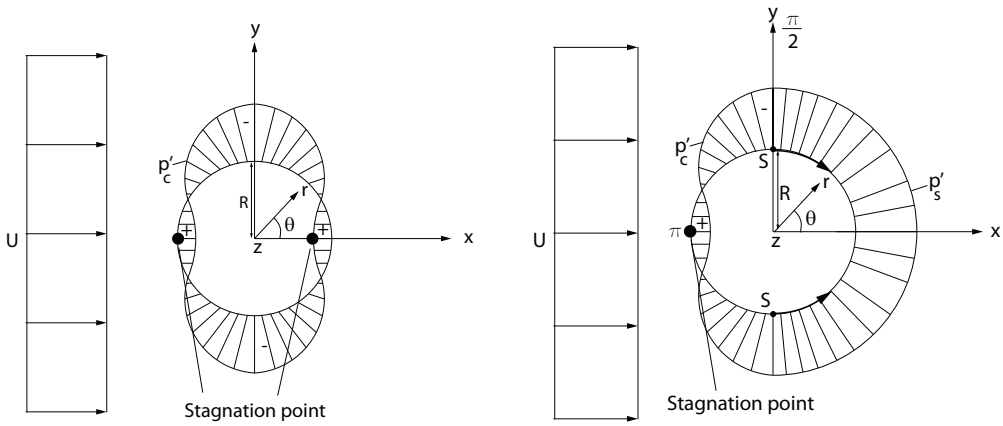

(a) Pressure distribution from potential theory.

(b) Assumed pressure distribution.

Figure 7.4: Pressure distribution around a cylinder.

The drag pressure distribution from Figure 7.4a is given by

$$p_c' = \rho U^2 \left(\frac{1}{2} - 2sin^2(\theta) \right) \tag{7.9}$$

where θ, is the polar angle. The netforce per length from (7.9) is zero due to symmetry in x- and y-axis, and this do not correspond to the real pressure distribution for the cylinder due to the velocity of the particles are relatively fast [15].

Assumed drag pressure distribution

A more realistic pressure distribution for the cylinder is shown in Figure 7.4b. The pressure distribution p_c' is assumed to be identical from the potential theory, but the range will be in $[\frac{\pi}{2}; \frac{3\pi}{2}]$.

In real fluids seperation points S as shown in Figure 7.4b exists, in this project the seperation points are assumed to be placed constantly in $\pm\frac{\pi}{2}$, and this is a conservative assumption. The seperation points will in reality vary over the time as shown with arrows. To describe if any vortex that causes seperation occur, Keulegan-Carpenter (KC) number is used as indication and this is given by

$$KC = \frac{u_{x,max} T}{D} \tag{7.10}$$

If $KC \leq 5$, there are practically no seperation and the potential theory can be applied. If $KC \geq 5$ there are seperation and the semi-empiric Morison's formula should be applied. The KC distribution every $T/8$ is in the range of $T = [0; 5]s$. can be seen in Table 7.2

Table 7.2: KC distribution.

T	KC
$[s]$	$[-]$
0	0
1.25	97
2.5	138
3.75	98
0	0

As it can be seen there will occur seperation points. From the seperation points S it is assumed that the suction pressure distribution p'_s is constant between $\pm\frac{\pi}{2}$ as shown in the figure. The magnitude of the pressure is assumed to be

$$p'_s = -\frac{3}{2}\rho U^2 \tag{7.11}$$

In the assumed pressure distribution there are vortices behind the cylinder and there is only one stagnation point in front of the cylinder. The pressure distribution from the drag that is going to be applied are (7.9) and (7.11).

Comparing the assumed drag pressure to Morison's equation

In the following the assumed pressure distribution will be compared to semi-empirical Morison's equation for the drag force to check if there are any agreement. Since the Morison's equation do not describe the pressure distribution, the assumed drag pressure distribution will be integrated so the netforces per length from the pressures p'_c and p'_s, will be found acting in the x-direction. The integrated drag pressure distribution will then be compared with Morison's equation for drag force. As it can be seen in Figure 7.4b the compressive and suction pressures are symmetric around the x-axis and this will be exploited. And the forces must be positive in the x-direction. The suction netforce per length in x-direction is found by

$$f'_s = 2\int_0^{\pi/2} p'_s R cos(\theta) d\theta = 2\left(\frac{3RU^2\rho}{2}\right) \tag{7.12}$$

the compression netforce per length is found by

$$f'_c = 2\int_{\pi/2}^{\pi} p'_c R cos(\theta) d\theta = 2\left(\frac{1RU^2\rho}{6}\right) \tag{7.13}$$

The total netforce per length that acts on the cylinder based on the assumed drag pressure based on potential theory therefore becomes

$$f'_D = f'_s + f'_c = 2\left(\frac{3RU^2\rho}{2}\right) + 2\left(\frac{1RU^2\rho}{6}\right) = \frac{8}{3}RU^2\rho \tag{7.14}$$

Usually the drag coefficient in Morison's equation for drag force is below one, the reason why the assumed drag coefficient is high is due to the assumed placement of the seperation

points. The drag coefficient and the inertia coefficient from the Morison's equation are usually found from experiments. The assumed drag coefficient will be compared to a more realistic value by comparing with Morison's equation for drag force and this is given by

$$f'_D = \frac{1}{2}\rho C'_D U^2 A \tag{7.15}$$

where A, is the projection perpendular to the current direction of the body and this can be expressed as $A = 2R$, C_D is the drag coefficient that takes the roughness of the surface into account. When comparing (7.14) and (7.15) the drag coefficient gives

$$\frac{8}{3}RU^2\rho = \frac{1}{2}\rho C_D U^2 2R \rightarrow C'_D = \frac{8}{3} \tag{7.16}$$

So the drag coefficient that is going to be applied into (7.14) is adjusted to the semi-empirical Morison's equation for drag force and is given by

$$\gamma = \frac{C_D}{C'_D} = C_D\frac{3}{8} \tag{7.17}$$

So when there is seperation, the drag pressure based on the potential theory will be adjusted to the semi-empirical Morison's equation. Therefore the drag pressure distribution that is going to be applied in the substructure in FEA will be adjusted by (7.17), so the drag pressure distribution will be given by.

$$p_d = p'_c\gamma = \left(\rho U^2\left(\frac{1}{2} - 2sin^2(\theta)\right)\right)\gamma \text{ for } \frac{\pi}{2} \leq \theta \leq \frac{3\pi}{2} \tag{7.18}$$

$$p_d = p'_s\gamma = \left(-\frac{3}{2}\rho U^2\right)\gamma \text{ for } \frac{-\pi}{2} \leq \theta \leq \frac{\pi}{2} \tag{7.19}$$

Where the forces must be positive in x-direction, therefore following polar limit are shown as well.

Variation of the assumed drag pressure distribution

The horizontal particle velocity is in phase with the surface elevation as it is shown in Figure 7.5. When the wave surface is in the crest (1) the drag pressure has a maximum value and the total horizontal force per length of the drag pressure is positive in the x-direction. If the wave surface is in the mean water level (2) the drag pressure is zero and therefore the drag force per length is also equal to zero. If the surface elevation is in the trough, the direction of the drag pressure and therefore the total horizontal force per length of the drag force in (3) is in the opposite direction.

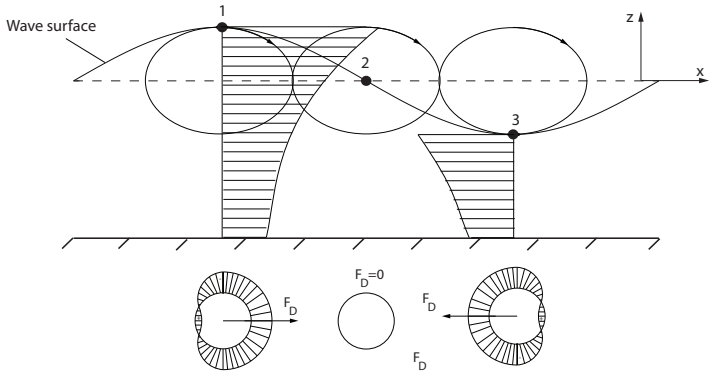

Figure 7.5: Variation of the drag pressure due to the surface elevation.

When the drag pressure distribution is determined, the direction of the flow is in the x-direction, so if there is a shift in the sign, the integration borders for the assumed drag pressure distribution, when determining the total force from the drag contribution, this will change. So to avoid this situation the limit of the time t will be 2.5 s.

7.2 Inertia pressure distribution

In the following the inertia pressure distribution around a cylinder will be defined and this is going to be applied for the substructure in *Abaqus*. It is a fact that the flow will be disturbed due to a cylinder and this has to be taken into account, and therefore the hydrodynamic mass of the water has to be considered. The cylinder diameter has to be smaller when compared to the particle motion amplitude, that is $D < L/5$, and that in the following range $x \leq D/2$ the acceleration and the pressure gradient is assumed to be constant, where $x = rcos(\theta)$.

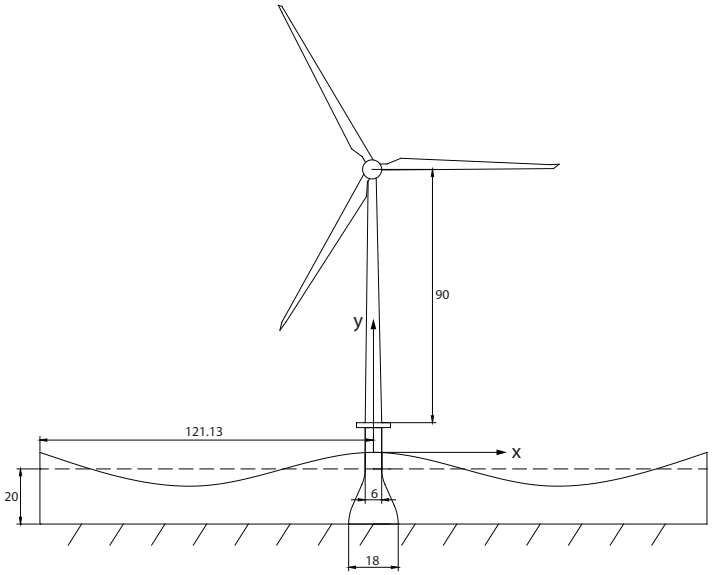

(a) Definition of the coordinate system in offshore windturbine in m.

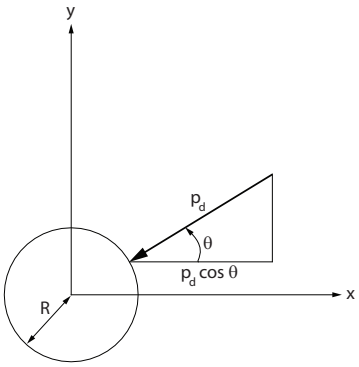

(b) Inertia pressure definition.

Figure 7.6: Inertia pressure coordinate system definition.

The following limit should also be applied $kx = \frac{2\pi}{L}x < \frac{2\pi}{10}$. Since the wave number is small, see Table 7.1, there is no problem. And following is also applied $cos(kx) \approx 1$ because

the wave number is small and $sin(kx) \approx kx = krcos(\theta)$. These limits are rough estimates in the limit of $D \approx \frac{L}{5}$. Due to the fact that this is a disturbed flow this has to be taken into account in the potential flow, therefore the total potential flow will be considered and this consists of the sum of the undisturbed velocity potential, φ_o and the diffraction potential, φ_d and this total potential flow is given by

$$\varphi_t = \varphi_o + \varphi_d \tag{7.20}$$

The overall result for the total potential flow is given by

$$\varphi_t = g_o \left(\overbrace{cos(\omega t)}^{\text{undisturbed flow}} + \overbrace{sin(\omega t)k(r + \frac{R^2}{r})cos(\theta)}^{\text{disturbed flow}} \right) \tag{7.21}$$

This equation satisfy the Laplace equation, where there is no flow through the structure for $r = R$. Far away from the structure the flow is undisturbed and this will then be given by (7.1). That is for $\varphi_t \to \varphi_o$ for $r \to \infty$. The inertia pressure in $r = R$ is then found by

$$p_M(R, \theta, z, t, a, \omega, h) = \left(\rho \frac{\partial \varphi_t}{\partial t} \right) \tag{7.22}$$

where $\frac{\partial \varphi_t}{\partial t}$ is partial differentation of the total potential flow with respect to time.

$$p_M(R, \theta, z, t, a, \omega, h) = \rho g_o \omega (\overbrace{-sin(\omega t)}^{\text{undisturbed flow}} + \overbrace{cos(\omega t) 2kRcos(\theta)}^{\text{disturbed flow}}) \tag{7.23}$$

The contribution from the undisturbed and disturbed flow is marked as shown in (7.23) This inertia pressure distribution is going to be applied for the substructure in *Abaqus*.

Variation of the inertia pressure distribution

In the following the variation of the inertia pressure distribution over time acting on a cylinder will be presented (Figure 7.7), the variation of the drag pressure distribution is shown as well. As presented earlier the surface elevation and the horizontal particle acceleration is out of phase with the time of 2.5 s. When the wave surface is in the MWL in (1), the horizontal particle acceleration is at the maximum, therefore the inertia pressure distribution biggest at that point, while the drag pressure is zero. Furthermore the direction of the total forces are shown for the inertia and drag pressure. When the surface elevation is at the crest (2), the drag pressure is in the maximum magnitude, while the inertia pressure is constant in the cylinder as compressive pressure. Due to the fact that this is symmetric, the total force for the inertia pressure is zero. The contribution from the inertia pressure in this project will be considered as a hydrostatic pressure, with the hight from the MWL to the crest. In (3) the maximum negative acceleration and the inertia pressure direction has changed in the opposite direction as shown. The drag pressure is zero at that point. In the wave trough (4), the drag pressure is maximum but has also changed direction as shown. The inertia pressure has shifted into suction pressure.

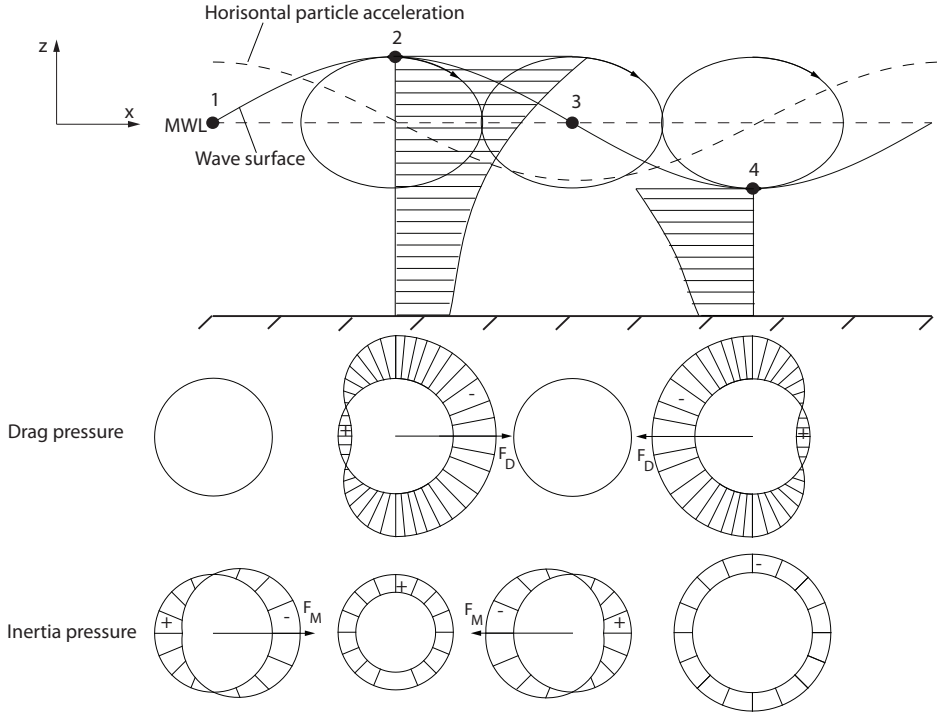

Figure 7.7: Variation of the pressure distributions in the cylinder due to surface elevation and acceleration of a particle.

In this project it is chosen to apply the pressure distribution to the FEA analysis of the substructure when the wave is in the crest (2) from Figure 7.7, this corresponds to a time of $t = 2.5\ s$. In the first the assumed drag pressure distribution is maximum at that point and for the second maximum pressure acting on the substructure is in that time, due to hydrastatic pressure distribution contribution from the inertia pressure. Another possibility is to check the total pressure distribution in the wave trough, but the assumed drag pressure distribution can not be applied in this time. Because of the integration limits found in Section 7.1.

7.2.1 Total pressure distribution to the substructure

The total pressure distribution that will be applied to the substructure in FEA will be given by the drag pressure and inertia pressure.

Drag pressure

When looking at Figure 7.4b, there are two pressure contributions, and these are

$$p_d = p_c'\gamma = \left(\rho U^2 \left(\frac{1}{2} - 2sin^2(\theta)\right)\right)\gamma \text{ for } \frac{\pi}{2} \leq \theta \leq \frac{3\pi}{2} \tag{7.24}$$

$$p_d = p_s'\gamma = \left(-\frac{3}{2}\rho U^2\right)\gamma \text{ for } \frac{-\pi}{2} \leq \theta \leq \frac{\pi}{2} \tag{7.25}$$

Inertia pressure

The inertia pressure is given by

$$p_M(R,\theta,z,t,a,\omega,h) = \rho g_o \omega(-sin(\omega t) + cos(\omega t)2kRcos(\theta)) \tag{7.26}$$

where g_o is given by (7.2). When analysing the pressure distribution the surface elevation will be taken from $z = 0$ due to the fact that the linear wave theory is applied. The contribution from current is disregarded in this project, even though it will contribute to increase the horizontal particle velocity and therefore the drag [23].

The drag coefficient and inertia coeffiecient that is going to be applied are shown in Table 7.3. In reality these values should have been found from experiments because these values vary over time.

Drag coefficient C_D	Inertia coefficient C_M
0.75	2

Table 7.3: Drag coefficient and inertia coefficient.

Inertia force

In the following the inertia force is going to be described, so the total force acting on the substructure can be found, to check if the magnitude is realistic and this will be compared to the wind force. Before defining the final inertia force first a fictious force will be considered for undisturbed flow and this force is called *Froude-Krylof* force, *(f_{FK})*, this force is identical with the force that gives a cylinder fluid element a horizontal acceleration within the wave motion and this is given by

$$f_{FK} = \rho\pi R^2 \dot{u} \tag{7.27}$$

where $\dot{u}$ is the horizontal acceleration and is given by

$$\dot{u} = \omega k g_o cos(\omega t) \tag{7.28}$$

In the following the inertia force per length, f_M is going to be defined in order to determine the total force acting on the substructure, this is the integral of the inertia pressure distribution around the cylinder defined by (7.26)

$$f_M = \int_0^{2\pi} (-p_M(R,\theta,z,t,a,\omega,h)cos(\theta))Rd\theta \tag{7.29}$$

For small arc-length, the arc length is given by $sin(d\theta) \approx d\theta$. And this is given by $d\theta \approx \frac{\Delta}{R}$. This is illustrated in Figure 7.8.

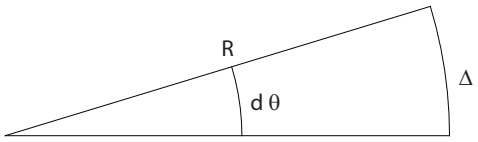

Figure 7.8: Assumption of the arc length.

After some rewriting the netforce per length for the inertia force is found by

$$f_M = 2\rho\pi R^2 \dot{u} \tag{7.30}$$

When this is compared to the fictious force *Froude-Krylof* force, f_{FK} (7.27), this is twice the magnitude. The inertia force per length is for the disturbed flow. There is a mass coefficient C_M that takes the disturbed flow caused by the geometry of the structure into account. If the inertia coefficient has a value of 1, this corresponds to the undisturbed flow around the cylinder. In general the mass coefficient is given by

$$C_M = \overbrace{1}^{f_{FK}} + C_m = 1 + \frac{m_h}{m} \tag{7.31}$$

where C_m is the added mass coefficient, m_h is the added mass per meter and m, is the dispersed mass per meter from a structure, due to the fact that a cylinder strip per meter is calculated, the dispersed mass will be given by $m = \rho\pi R^2 1$. The added mass for the the cylinder according to [35, p. 47] is given by

$$m_h = \rho\pi R^2 \tag{7.32}$$

Therefore the mass coefficent becomes, $C_M = 2$, this is why when comparing with *Froude-Krylof* force (7.27) that the inertia force per length (7.30) is twice the fictious force, due to the fact this is a cylinder.

7.3 Total force acting on the substructure

In the following the total force per length to the substructure is going to be calculated by using Morison's equation. This is to check if the result from the total force from the hydraulic pressure is realistic, due to the fact that the wave period and the wave height are assumed values.

$$f_{total} = f_D + f_M \tag{7.33}$$

Where the drag force per length is given by

$$f_D = \gamma R u_x |u_x| \rho \tag{7.34}$$

and the inertia force per length is given by

$$f_M = C_M \pi R^2 \dot{u} \tag{7.35}$$

where for $x = 0$, the acceleration is given by

$$\dot{u} = \omega k g_o cos(\omega t) \tag{7.36}$$

The variations of the forces per length for the drag and inertia depend on the particle velocity and the acceleration of the particle. The integration over the height is taken per meter as shown in Figure 7.3b. In the theory Morison's equation is the only applicable for two border line cases for pure acceleration and pure drag force [15, p. 33]. But experiences has shown that these two borderlines can be mixed, so larger resultant force is found. The total force is found by integrating over the height by using Simpson integration rule and the variation of the total force over the time can be seen in Figure 7.9. When comparing Figure 7.9 and Figure 7.2, the total force from the drag and inertia are in agreement with the variation of the velocity and acceleration of the particle.

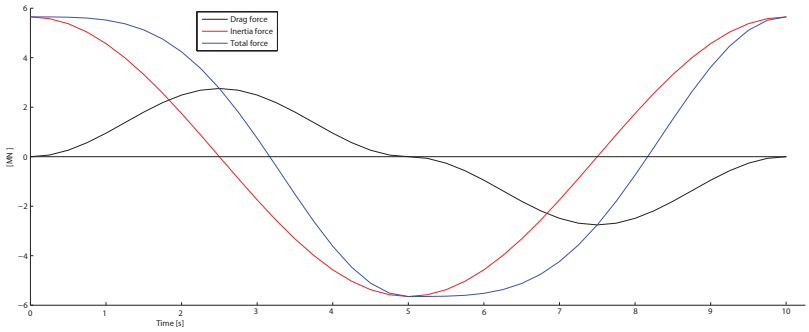

Figure 7.9: Variation of the total force acting on the simplified substructure.

Roughly the inertia force dominates when $KC < 5$ and there is drag dominans when $KC > 20$. As it can be seen when the total force is maximum, this has a value of 5.65 MN and this is about 3 times larger than the wind force. When comparing with the forces of 2 MN $\pm$ 1 MN from the current and waves for the monopile, the result is realistic for the substructure. Because it is expected that the inertia force will be big for the substructure due the geometry.

How much it contributes to the section forces will be checked in Chapter 9.

The preliminary study could have been improved by applying non-linear wave theory, where the stream function could have been applied. CFD study on the substructure and a Boundary Element Model by using *ShipSim* could have been studied. But due to limit of time these have not been invistigated.

CHAPTER 8

FINITE ELEMENT MODELING OF THE SUBSTRUCTURE

In the following the substructure that is going to be modeled by utilizing FEA is presented. The offshore wind turbine can be seen in Figure 8.1. A 3D FEA model is shown in Figure 8.1b and this consists of the soil, bucket foundation with substructure and the tower. The soil is modeled as a axisymetric due to the fact that the substructure has a circular shape. By having this soil geometry, the mesh discritization between the soil and the bucket can be kept as quadratic as possible.

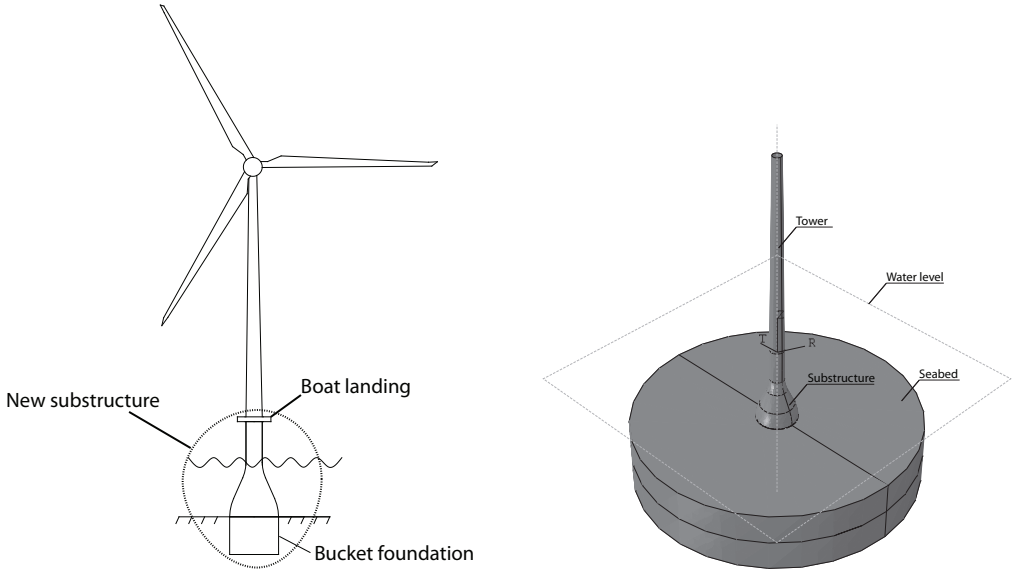

(a) Offshore wind turbine.

(b) A tower, substructure and soil in FEA.

Figure 8.1: A view of the wind turbine and the substructure.

Since the aim of this project is to analyse the response of the substructure when subjected to the hydraulic pressure, self weight and wind force, the tower will be disregarded in this project(Figure 8.2a). To reduce the computational time of the analysis only the half of the substructure, soil and bucket foundation will be modeled and this can be seen in Figure 8.2b. The model can be reduced because it is axisymmetric. This model consists of the following parts: substructure with bucket foundation, soil and a discrete rigid part.

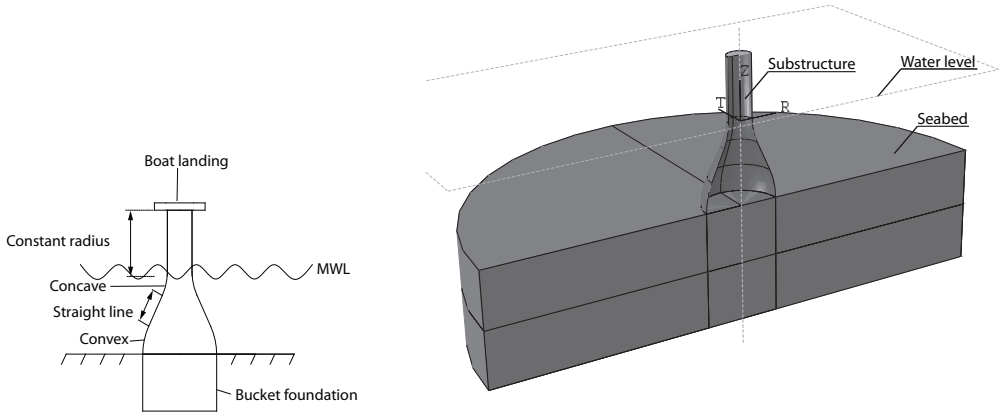

(a) Substructure. (b) Reduced FEA model of substructure.

Figure 8.2: A view of the substructure and soil that is going to be modeled in FEA.

8.1 Dimensions and geometry of the substructure model

In the following the dimensions and geometry of the model that is going to be applied in the FEA model presented. The geometry and dimensions that are going to be used for the soil, bucket foundation and substructure are going to be described in the following.

8.1.1 Geometry of the soil

The geometry that is used for the soil is $3.5 \times D_1$ in radial direction and $2 \times H_1$ in height, where D_1 is the diameter of the bucket foundation and H_1 is the height of the bucket foundation. This geometry is used for avoiding the boundary effects of the stresses. The geometry of the soil can be seen in Figure 8.3. Given H in the figure is for a horizontal lineand V is for a vertical line in *Abaqus*.

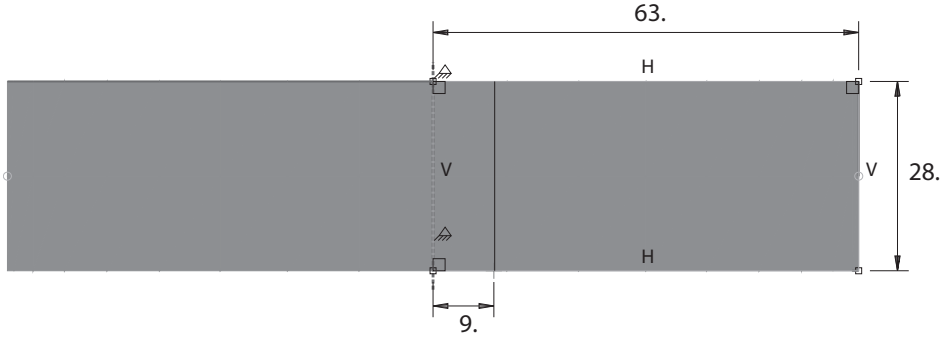

Figure 8.3: Sketch of the soil [m].

8.1.2 Geometry of the bucket foundation

The geometry of the bucket foundation was inspired by [29]. The geometry is given in Figure 8.4 and the dimensions are shown in Table 8.1

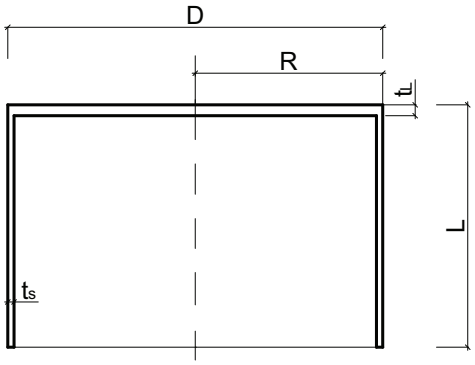

Figure 8.4: Bucket geometry.

Table 8.1: Bucket geometry parameters.

R	L	t_s	t_L
$[m]$	$[m]$	$[m]$	$[m]$
9	14	0.04	0.2

8.1.3 Geometry of the substructure

The geometry used for substructure was inspired by a bottle neck shape, the geometry is given in Figure 8.5 and the dimensions are shown in Table 8.2. The geometry of the substructure will be investigated and optimized in Chapter 9.

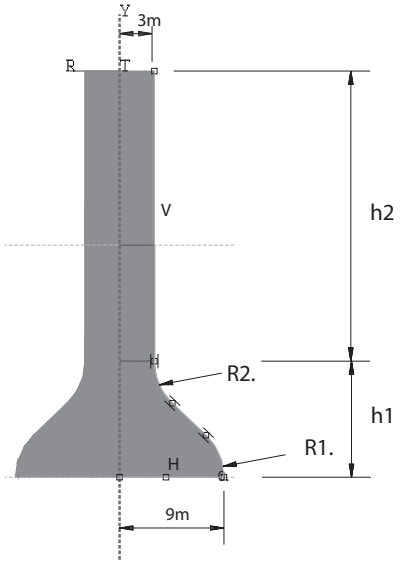

Figure 8.5: Substructure geometry.

Table 8.2: Substructure geometry parameters.

$R1$	$R2$	$h1$	$h2$
$[m]$	$[m]$	$[m]$	$[m]$
5	5	10	25

These dimensions will be applied in Chapter 9 and Chapter 10. But the dimensions of the substructure will be optimized in Chapter 9.

8.2 Parts of the model

In the following different parts that has been applied in the reduced FEA model for the analysis of the substructure will presented. Different parts of the substructure model shown in Figure 8.6 and this consist of following parts: substructure with bucket foundation, rigid discrete body and soil.

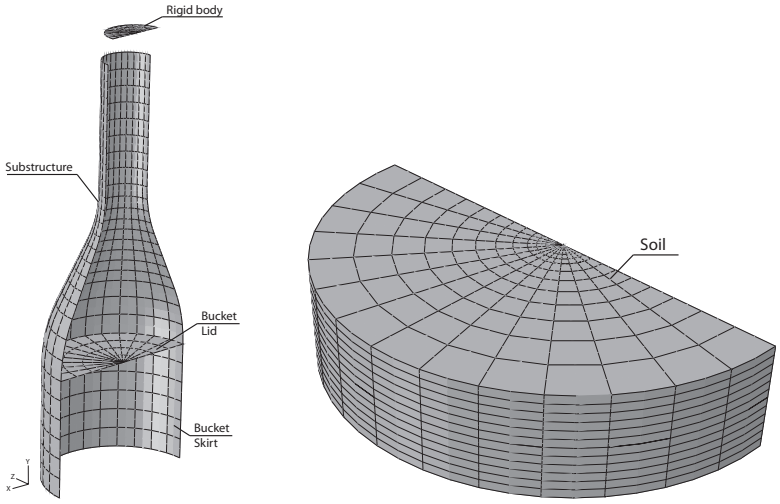

(a) Substructure part. (b) Soil part.

Figure 8.6: Different parts of substructure model.

Part of the substructure

The part, geometry, of the substructure and bucket foundation is created by using the feature of *Shell revolution*. A revolution of 180 degrees was applied, since only half of the model is modeled. For these parts S8R- shell elements are applied. In Chapter 5.2 curve shell elements are presented. A homogenous cross section of concrete with steel rebar is used for the substructure. For the bucket foundation a homogenous cross-section of steel is utilized. For the substructure the material model of Concrete Damaged Plasticity will be applied in the analysis. The mechanical properties of the ultra high performance concrete is applied and these are defined in Section 3.3. For the elastic analysis, only elastic materials will be applied.

Part of discrete rigid body

A discrete rigid body part (*Discrete Rigid*) is used for the upper part of the substructure in order to apply loads which are resultants from the disregard part of the offshore wind turbine.

A discrete rigid body is a rigid part that is used for modeling bodies that can not deform [4]. The discrete rigid body is also applied to avoid singularity when the moment contribution and horizontal load from the wind is going to be applied as a concentrated forces. By applying the rigid discrete body, the concentrated loads are distributed to the substructure. Furthermore the mesh discretization of the parts can as well be seen. The convergence analysis has not been performed in this project regarding the linear prebuckling eigenvalues.

Soil part

The soil part is created as a solid shape, which is revolved 180 degrees. The shape of the soil can be seen in Figure 8.6b, this has been made as a half-circled. For the soil part continuum element type C3D20R is applied and this is presented in Chapter 5.1. An elastic material will be applied for the soil part. The properties of the undrained clay material are used and the mechanical properties are defined in Section 3.4.

Assembly of different parts

The different parts that has been used for the modeling are shown in Figure 8.6, they are assembled together by using the *Tie constraints* function. The definition of *Tie constraints* for the model can be seen in Figure 8.7.

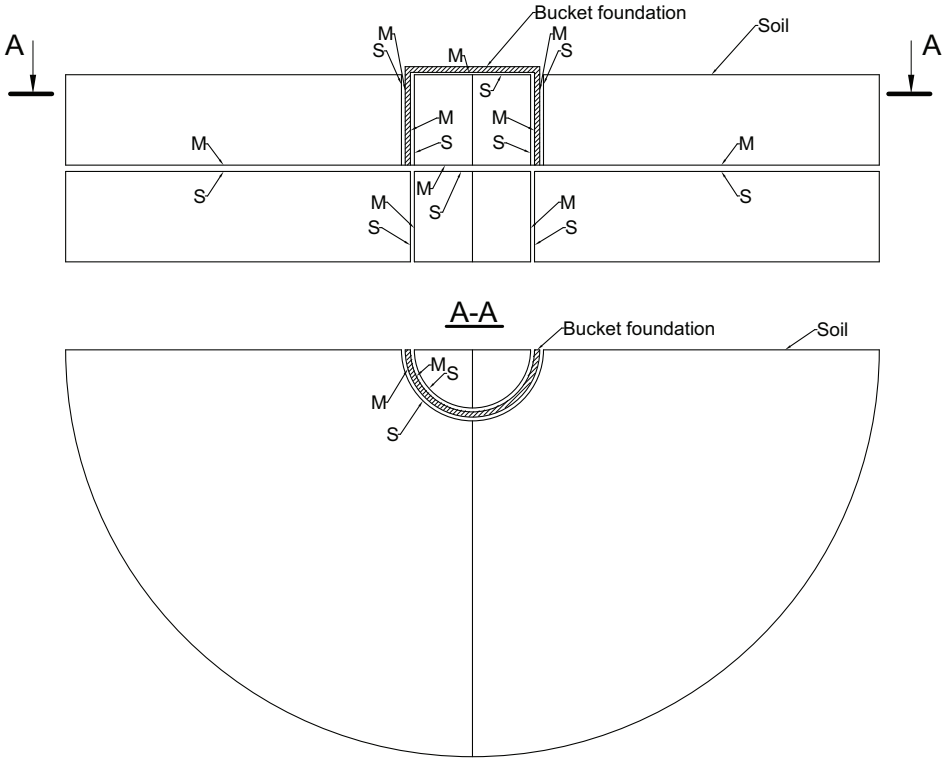

Figure 8.7: Tie constrains for the bucket foundation and the soil.

In Figure 8.7 M stands for *Master surface* and S - *Slave surface*. The much stiffer part is selected as a master surface.

8.3 Boundary condition for the substructure model in FEA

In the following the boundary conditions that has been applied in the substructure model presented. In the model boundary conditions are applied in the symmetry plane of the model, disrete rigid body and at the bottom of the soil.

8.3.1 Symmetric boundary conditions

Since only half of model is created, the symmetric boundary conditions has been applied to the model (for the soil, substructure and bucket foundation). The boundary conditions has been applied in the cylindrical coordinate system with fixed displacement in polar θ direction and rotation around radial direction R.
For the rigid discrete body the symmetric boundary condition has been applied in the reference node for the direction of Z axis and these can be seen in Figure 8.8a.

8.3.2 Fixities

At the base of the soil a fully fixed boundary conditions has been applied.

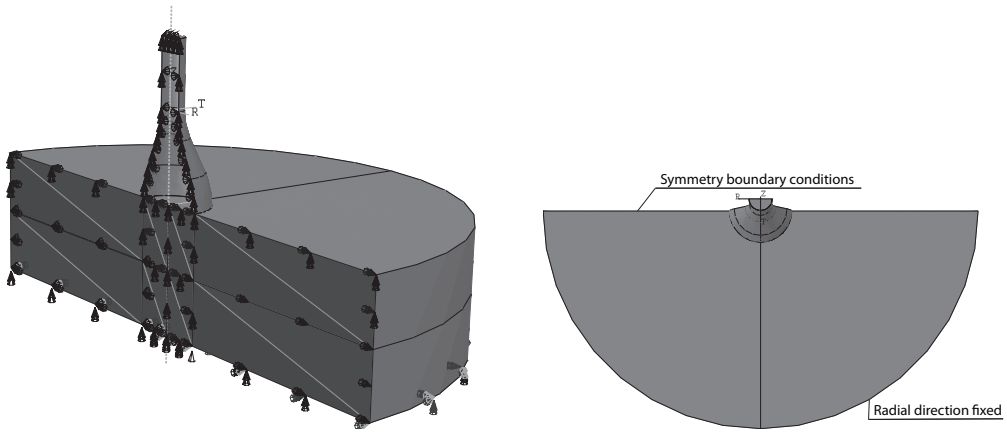

(a) Symmetric boundaries. (b) top view.

Figure 8.8: Symmetric and radial boundary conditions.

8.3.3 Loads on the substructure FEA model

The loads that has been applied to the substructure FEA model are presented in Chapter 1. How the loads has been defined in the FEA model is described in the following, see Figure 8.9.

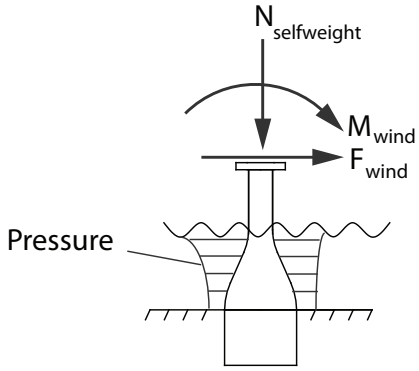

Figure 8.9: Forces in the substructure.

Self weigth

The compound of the self weights that are going to be assigned in this project can be seen in Table 8.3.

Table 8.3: Dead loads.

Property	*Value*
Weight nacelle+rotors	410 t
Weight tower	300 t
Steel	7850 kg/m^3
Concrete	3200 kg/m^3
Clay	1800 kg/m^3

The self weight given as densities are applied as gravity forces in FEA. The gravity acceleration of $g = 9.81m/s^2$ is applied. The self weight from the tower and from nacelle including rotors are applied as pressure on the discrete rigid body.

Hydraulic pressure

The hydraulic pressure that is going to be applied is defined in Chapter 7. How the hydraulic is applied in the FEA model will now be presented. The hydraulic pressure distribution is defined in the cylindrical coordinate system in the height of $20m$ and the cylindrical coordinate system is defined at the mean water level. There are two contributions from the hydraulic pressure, it's the drag pressure and the inertia pressure. The drag pressure is divided into two contributions, the compression pressure (p'_c) and the suction pressure (p'_s). It is shown in Figure 8.10 how they are applied to the substructure. The inertia pressure is applied all over the surface below the mean water level.

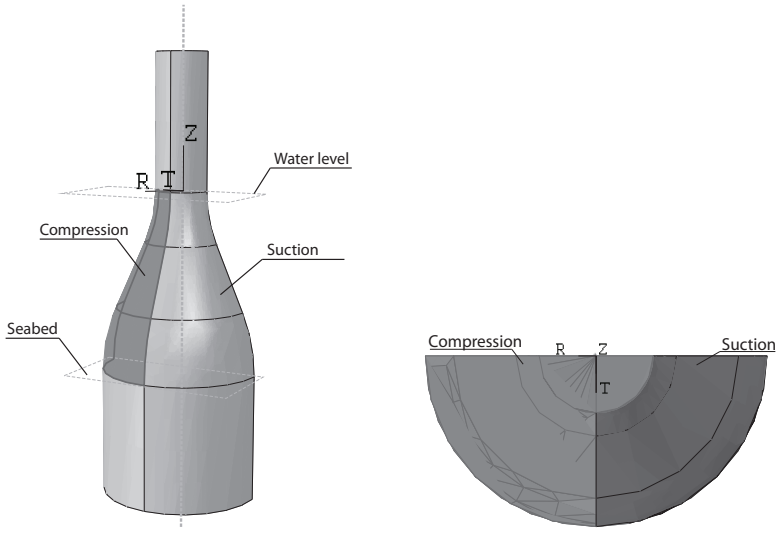

(a) Side view. (b) Top view.

Figure 8.10: Drag pressure.

The properties of the wave mechanics that are going to be applied are shown in Table 7.1.

Wind load

The magnitude of the wind load that is going to be applied can be seen in Table 8.4.

Table 8.4: Wind force based on [25].

Property	*Value*
F_{wind}	2 MN

The horizontal load is applied in the reference node of the discrete rigid body. The moment contribution from the wind load is applied as shown in Figure 8.11. The magnitude of the moment contribution has an arm of 90 m and this is distributed over the diameter of the substructure.

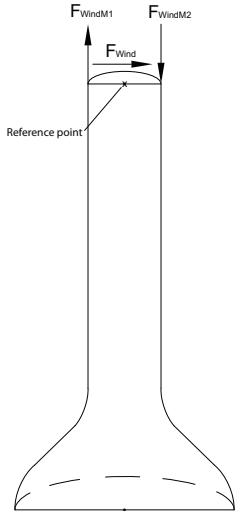

Figure 8.11: Wind load applied in the substructure.

CHAPTER 9

PRELIMINARY DESIGN OF THE SUBSTRUCTURE

In the following the preliminary design of the substructure will be described. In the preliminary design an elastic material will be considered were the elastic properties of the ultra high perfomance concrete from Table 3.1 are applied. It is chosen to invistigate 5 different shapes of the substructure. The hydraulic pressure, self-weight and the wind load will be applied. For the hydraulic pressure the time that will be applied is $t = 2.5\ s$. This time was defined in Chapter 7.2.

The response of the section forces will be focused on whenever there is an improvement when different shapes are checked. The section forces are checked because these forces will be used to find the amount of rebars that should be applied in the substructure. The section forces that will be evaluated are in the circumferential direction 1 and the meridional direction 2 as it is shown in Figure 9.1. These direction corresponds to the material direction of the substructure and the local coordinate system (1, 2, n) and the mesh discretization can be seen aswell. The section forces $SF1$ will be defined in the circumferential direction and section forces $SF2$ - in meridional direction.

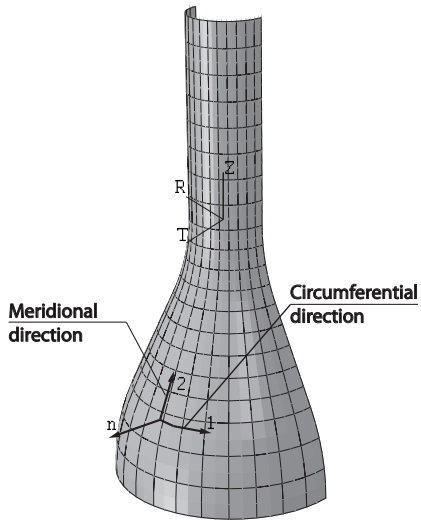

Figure 9.1: Material orientation.

In the preliminary design and final design of the substructure there will be defined two load steps. The self weight of the loads are applied in the substructure model in FEA as the

first load step. In the second load step the nature forces such as the hydraulic pressure and wind force are applied.

In the preliminary design a section thickness of the substructure chosen to be 110 mm. In the thickness direction 21 section points will be applied and Simpson integration is chosen. The only thing that is going to be changed is the shape of the substructure. *Static General* analysis will be performed.

For investigating different shapes of the substructure *Parameter Manager* function will be used. It's a function allowing easy and fast changes in the part sketch.

9.1 The evolution of the substructure shape

The geometry parameters that are going to be optimized are shown in Figure 9.2a. The way this is implemented in *Abaqus* is shown in Figure 9.2b. The concave line is defined as $R2$, the convex line is presented by $R1$, the straight line is indirectly changed by the height $h1$ and $h2$ in *Abaqus*. In the height of $h2$ the radius is constant.

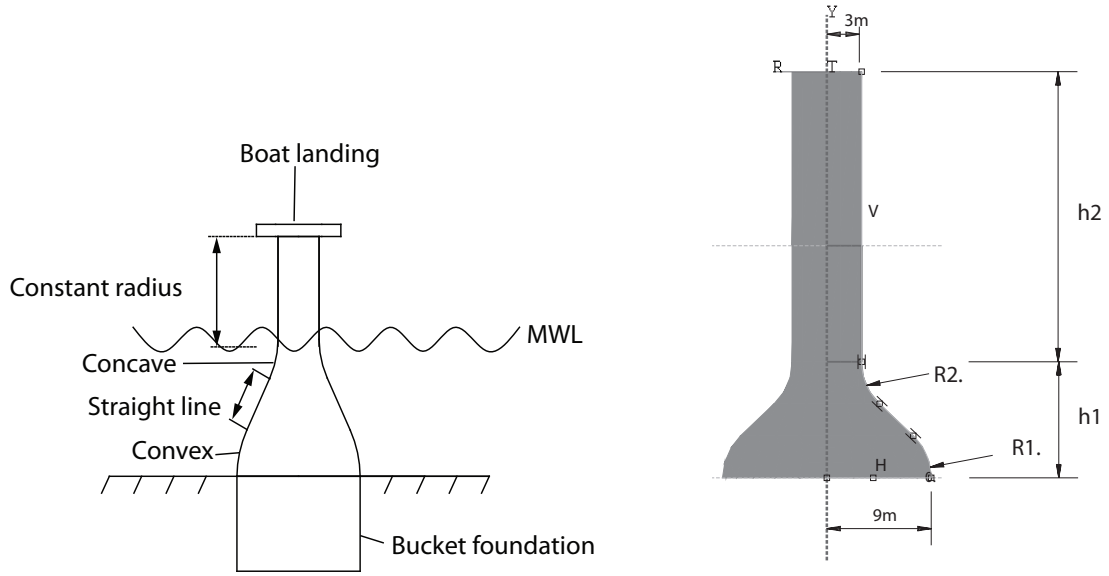

(a) Substructure.

(b) Sketch of the substructure.

Figure 9.2: Implementation of the parameter change of the substructure.

The changes of the substructure geometry can be seen in Figure 9.3. It has been decided that the winding of the optimal shape will only be up to mean water level (20 m) so the boat landing can be placed. The maximum value of $h1$ that can be applied is 20 m.

The initial geometry of the substructure shape was inspired by the shape of bottle neck, it can be seen in Figure 9.2b. This geometry will be investigated in the following by changing the geometries. In Table 9.1 5 different shapes of the substructure with different geometry parameters can be seen.

Table 9.1: Geometry parameters of the substructure.

Shape	$R1$	$R2$	$h1$	$h2$
$[-]$	$[m]$	$[m]$	$[m]$	$[m]$
1	5	5	10	25
2	5	9	13	22
3	5	9	15	20
4	8	12	19	16
5	17	14	20	15

The corresponding shapes of the substructure can be seen in Figure 9.3.

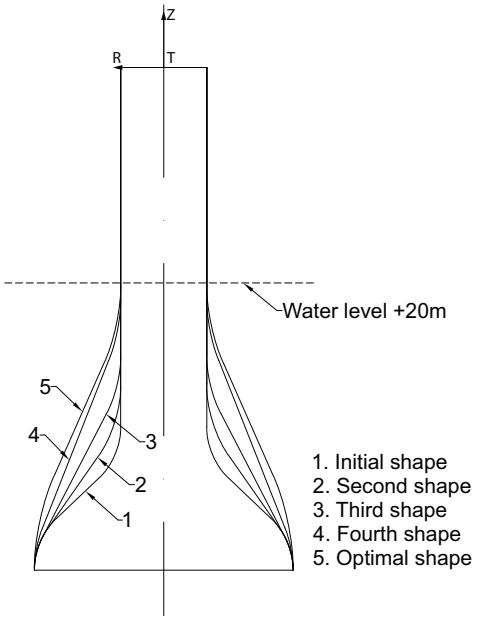

Figure 9.3: Substructure shape improvement.

In the following the response of the section forces for the 5 different shapes of the substructure are presented. Positive values of section forces correspond to tensile forces, while negative values of section forces correspond to compressive forces.

9.2 Initial geometry

The meridional and circumferencial section forces can be seen in Figure 9.4. The meridional section forces distribution can be seen in the substructure (Figure 9.4a). As it can be obtained the tensile forces concentrate in the height $h2$ and in the concave line $R2$. The circumferencial section forces are shown in Figure 9.4b, as it can be seen they concentrate in the concave line $R2$. Tensile surface forces concentrate in the place where the bigest winding of the shape is.

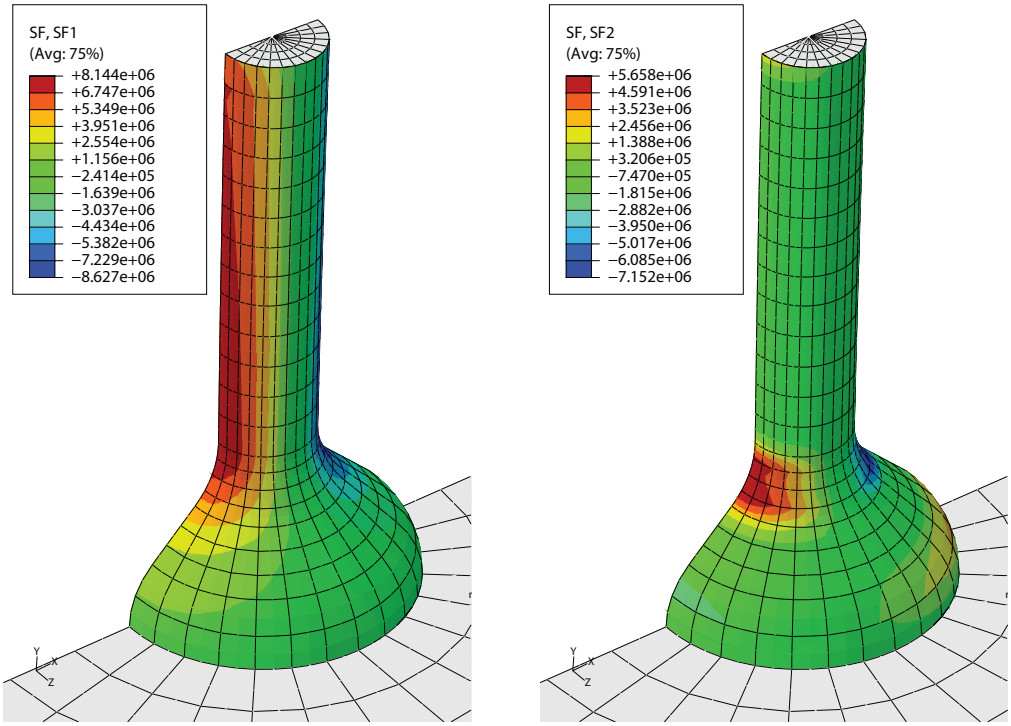

(a) Meridional section forces. (b) Circumferential section forces.

Figure 9.4: Section forces of proposed initial shape of the substructure.

Considering the plots of section forces shown in Figure 9.4 the highest meridional and circumferential section forces are 8.144MN and 5.658MN respectively. A new more optimized shape will be investigated in the following.

9.3 The second proposed shape

A more higher and smoother transition part for the second proposed shape is used.

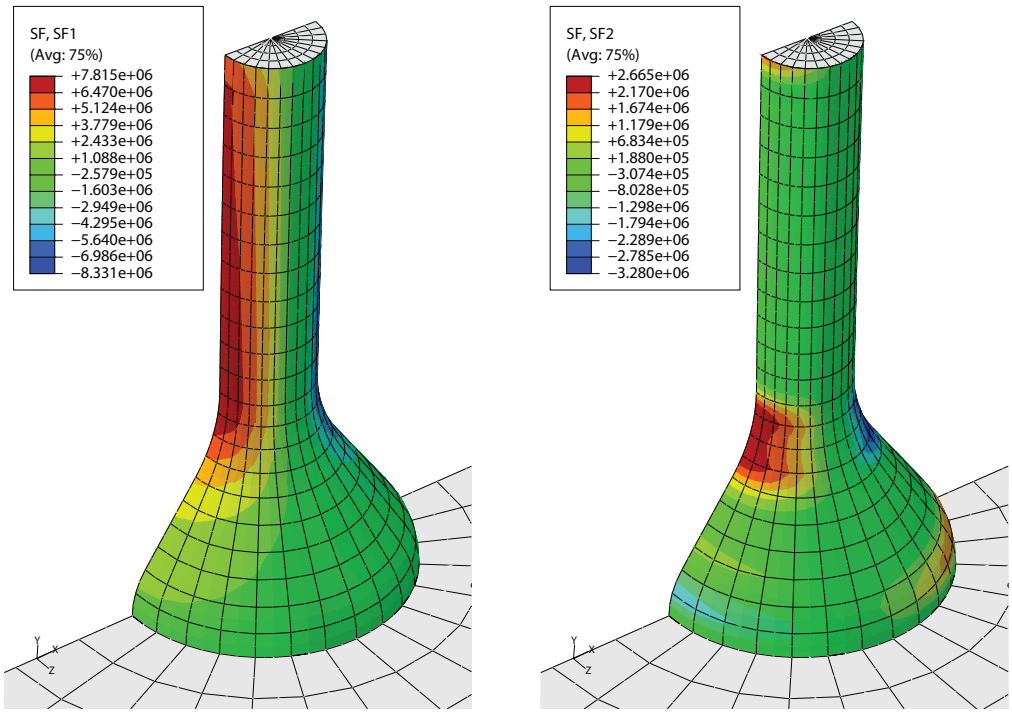

(a) Meridional section forces. (b) Circumferential section forces.

Figure 9.5: Section forces of proposed second shape of the substructure.

The highest meridional and circumferential section forces are 7.815MN and 2.665MN respectively it can be seen in Figure 9.5. The response of the section forces concentration is the same as in initial geometry.

9.4 The third proposed shape

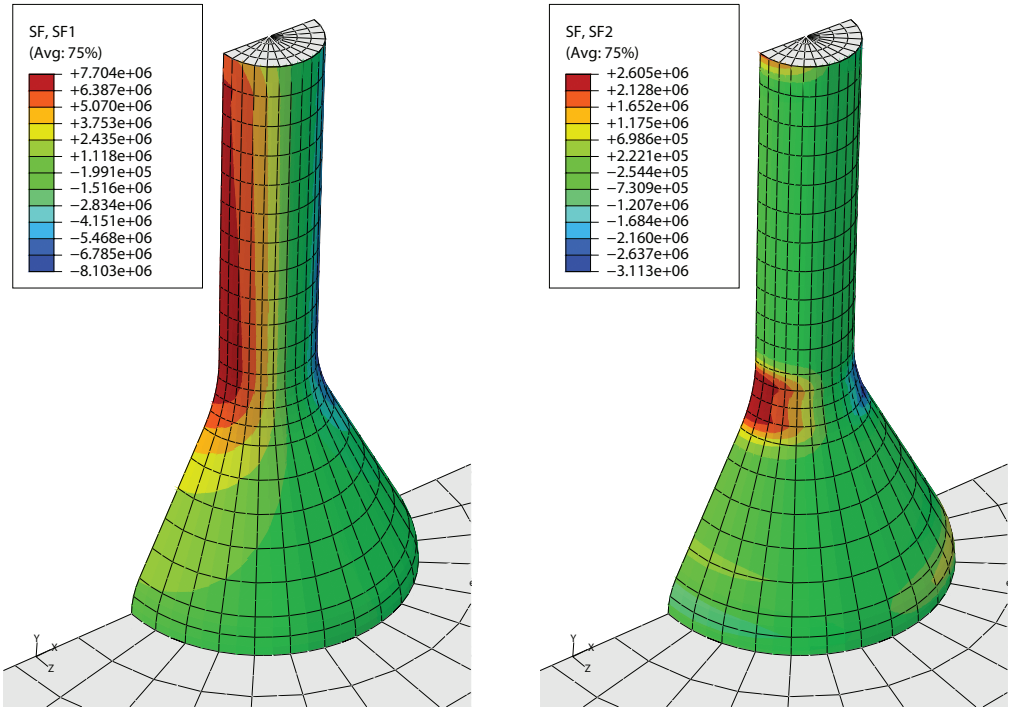

(a) Meridional section forces. (b) Circumferential section forces.

Figure 9.6: Section forces of proposed third shape of the substructure.

The highest meridional and circumferential section forces are 7.704MN and 2.605MN respectively it can be seen in Figure 9.6. The response of the section forces concentration is the same as in second proposed shape geometry.

9.5 The fourth proposed shape

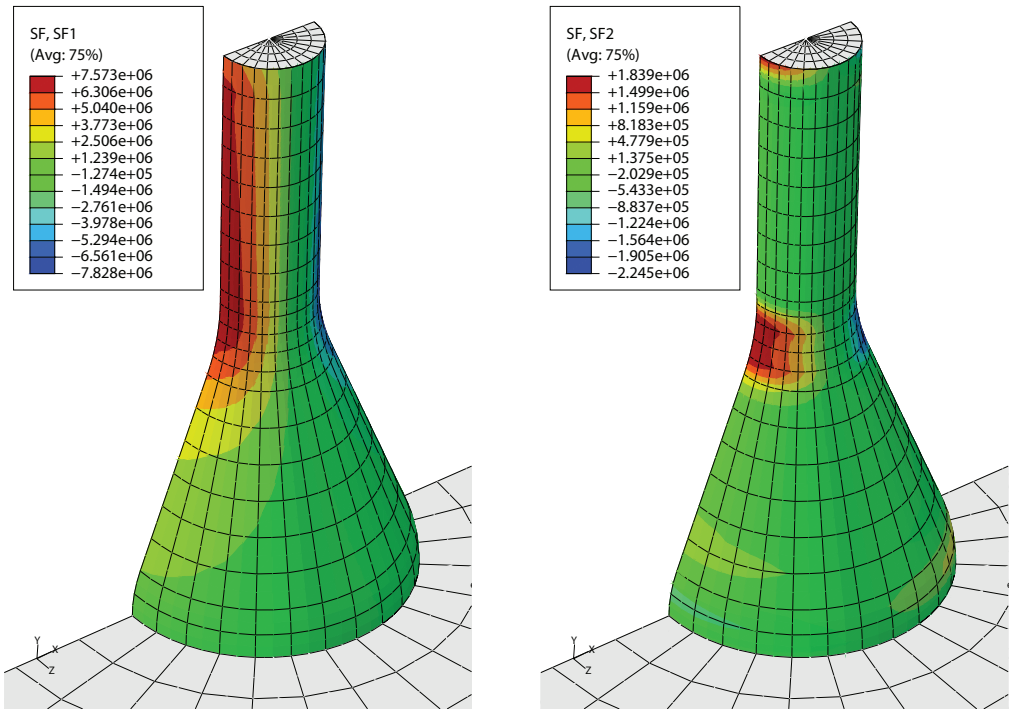

(a) Meridional section forces. (b) Circumferential section forces.

Figure 9.7: Section forces of proposed fourth shape of the substructure.

The highest meridional and circumferential section forces are 7.573MN and 1.839MN respectively it can be seen in Figure 9.7. The response of the section forces concentration is the same as in third proposed shape geometry.

9.6 The fifth proposed shape

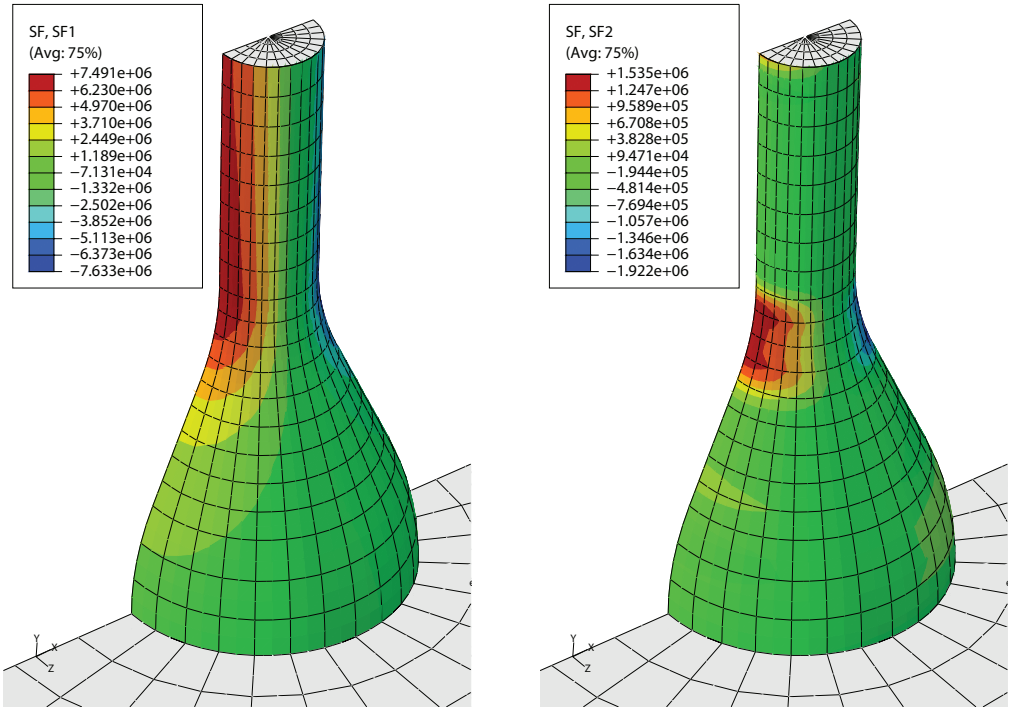

(a) Meridional section forces. (b) Circumferential section forces.

Figure 9.8: Section forces of proposed fifth shape of the substructure.

The highest meridional and circumferential section forces are 7.491MN and 1.535MN respectively it can be seen in Figure 9.8. The response of the section forces concentration is the same as in fourth proposed shape geometry.

9.7 Comparing the response of 5 different shapes

In the following the response of the section forces when changing the shape of the substructure will be presented. The response of section forces for the different shapes of the substructure are shown in Table 9.2. As it can be seen that when the substructure became smoother, the section forces has reduced. The observed tendency regarding the circumferential tensile forces is that the highest force concentration occured in the concave part of the substructure, in $R2$ and this can be seen in Figure 9.2b. For the meridional tensile forces the highest tensile forces were also in the concave part, $R2$ and in the height $h2$, these geometries can be seen in Figure 9.2b.

Table 9.2: Maximum tensile section forces of differently shaped structures.

$Shape$ $[-]$	$SF1$ $[N]$	$SF2$ $[N]$
1	$8.144e+06$	$5.658e+06$
2	$7.815e+06$	$2.665e+06$
3	$7.704e+06$	$2.605e+06$
4	$7.573e+06$	$1.839e+06$
5	$7.491e+06$	$1.535e+06$

When comparing initial and fifth shapes of the substructure, the meridional surface forces

decreased up to 0.653MN, a huge changes can be seen in circumferential surface forces, where it decreased around 4.123MN. The lowest section forces are found in the fifth proposed shape and this is chosen to be utilized in the final design of the substructure. In the following section force contribution from the hydraulic pressure will be checked and the shear force of the substructure will be shown and compared with the expected section forces from the tubular beam discussed in Section 1.5. The effect of the hydraulic pressure will also be checked for the linearized eigenvalue.

9.8 Effect of the hydraulic pressure on section forces and linearized eigenvalues to the substructure

In the following the effect of the hydraulic pressure on the section forces and eigenvalues will be considered. First the section forces can be seen in Figure 9.9 where the hydraulic pressure is excluded. The results can be seen in Table 9.3.

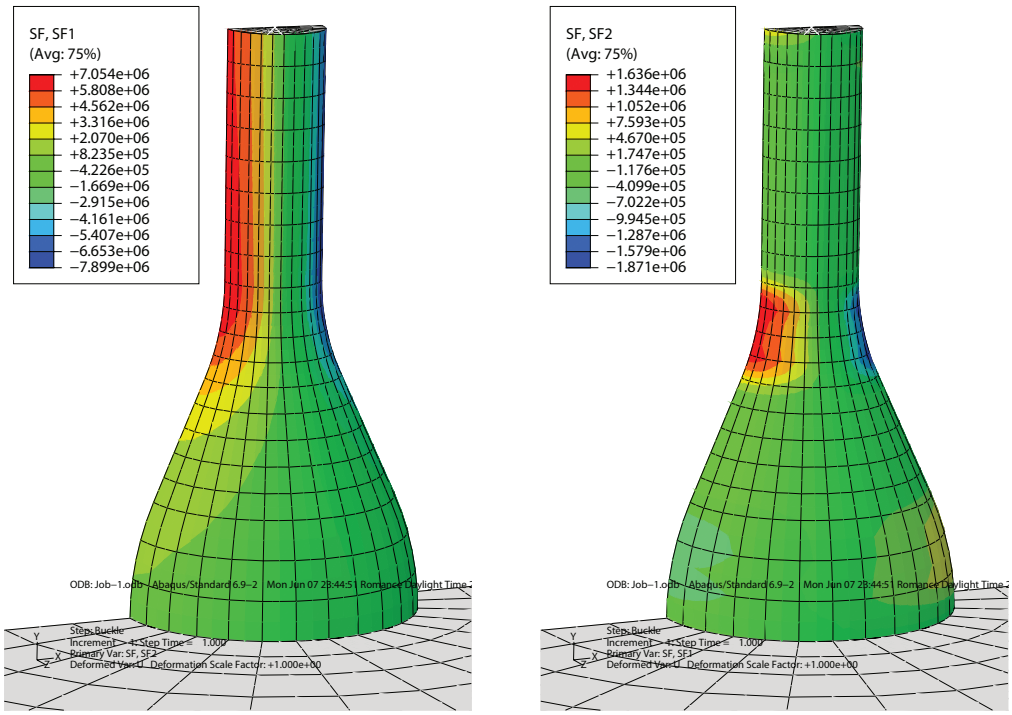

(a) Meridional section forces. (b) Circumferential section forces.

Figure 9.9: Section forces without hydraulic pressure.

Table 9.3: Maximal section forces without hydraulic pressure.

Tensile forces	
$SF1$ $[MN]$	$SF2$ $[MN]$
7.054	1.636

As it can be seen the maximum meridional section force deacrease while the circumferencial section force increase when compared with the result from Table 9.2 for the fifth shape. The differences in both cases are only 5 percent. When looking at Figure 7.7 for the pressure

distribution in the crest (2), compressive pressures are in the stagnation point. When these has been excluded the circumferential section forces became higher. In the case of section forces, the hydraulic pressure does not increase section forces substantially. The result from the linearized eigenvalues with hydraulic pressure can be seen in Table 9.5. The first 3 values of the linearized eigenvalues are shown.

Table 9.4: Linearized eigenvalues with hydraulic pressure.

λ_1	6.7637
λ_2	9.5663
λ_3	11.068

The linearized eigenvalues without hydraulic pressure can be seen in Table 9.5.

Table 9.5: Linearized eigenvalues without hydraulic pressure.

λ_1	7.26
λ_2	10
λ_3	11.791

When comparing the linearized eigenvalues from Table 9.4 and Table 9.5 the difference is small. So the hydraulic pressure is not a critical load for the substructure. The critical load is mainly from the wind. And even though that the total horizontal load from the waves is about 3 times larger than the wind load, the wind load is critical because of the moment contribution. The wind load is 90 m long from the boat landing level. The linearized eigenvalues are not closely spaced and the buckling load is not critical.

9.9 Comparing with the equivalent tubular beam

The substructure was discussed in Section 1.5 to be an equivalent to a clamped tubular beam. The expected section forces were also discussed. In the following the shear force will be checked if it also occur in the web of the substructure as in the clamped tubular beam. The hydraulic pressure, self weight and wind load is applied and the results can be seen In Figure 9.10.

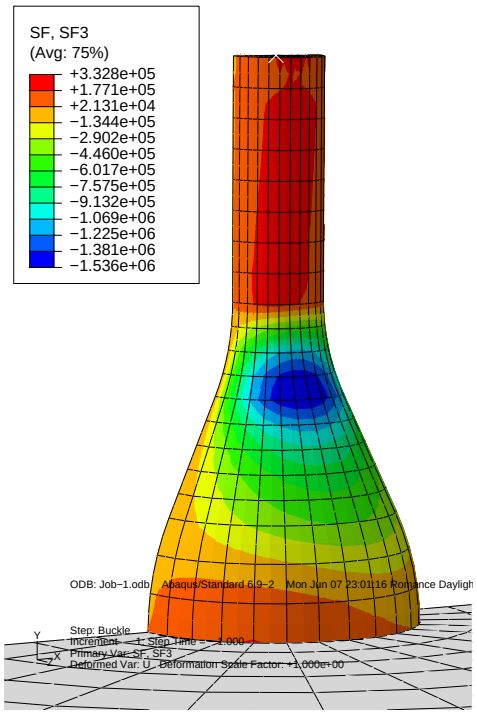

Figure 9.10: Shear forces in the substructure.

As it can be seen in the figure, a concentrated shear forces in the web has been obtained as expected. The meridional section forces are also in a good agreement with the extpected forces.

CHAPTER 10

FINAL DESIGN

In the following the final design of the substructure is going to be described. The fifth shape from the prelimary design is chosen to be the final shape of the substructure. The amount of rebar that is going to be applied is going to be calculated where the section forces are obtained from elastic analysis in Chapter 9.

The mentioned rebar arrangement in Chapter 1.7 is utilized. The substructure with a single and two rebar layers as shown in Figure 10.1 will be investigated in the project. The substructure with two rebar layers will be defined as Substructure 1 and the substructure with two rebar layers will be defined as Substructure 2. When the amount of rebar that should be applied is found, a non-linear analysis will be performed by using the Concrete Damaged Plasticity material model. Afterwards the wind load is going to be increased twice, to see how well the rebar layer is exploited. Then the linear prebuckling analysis will be performed for two substructures with different rebar layers in order to check if these two substructures have a buckling risk. Two substructures with different rebar layers are going to be analysed with geometric imperfection to check if the structures are geometric imperfection sensitive.

10.1 Rebar layers of the substructures

The amount of rebars needed is going to be calculated using the maximal section forces, they are given in Table 10.1. The meridional section forces are going to be used for calculating the needed amount of meriodional rebars. The circumferential section forces are going to be used for the circumferential rebar.

Table 10.1: Maximal section forces found in the substructure.

Tensile forces	
$SF2$ $[MN]$	$SF1$ $[MN]$
7.491	1.535

The amount of rebar that should be applied per meter for the substructure is found by using

$$A_s = \frac{f_{y,k}}{SF} \tag{10.1}$$

where A_s is the area of the rebar, f_{yk} is the tensile strength of steel, SF is the section force. By using this formula the result for the two different rebar layers can be seen in Figure 10.1. The required cover layer and rebar spacing are defined in Table 3.5.

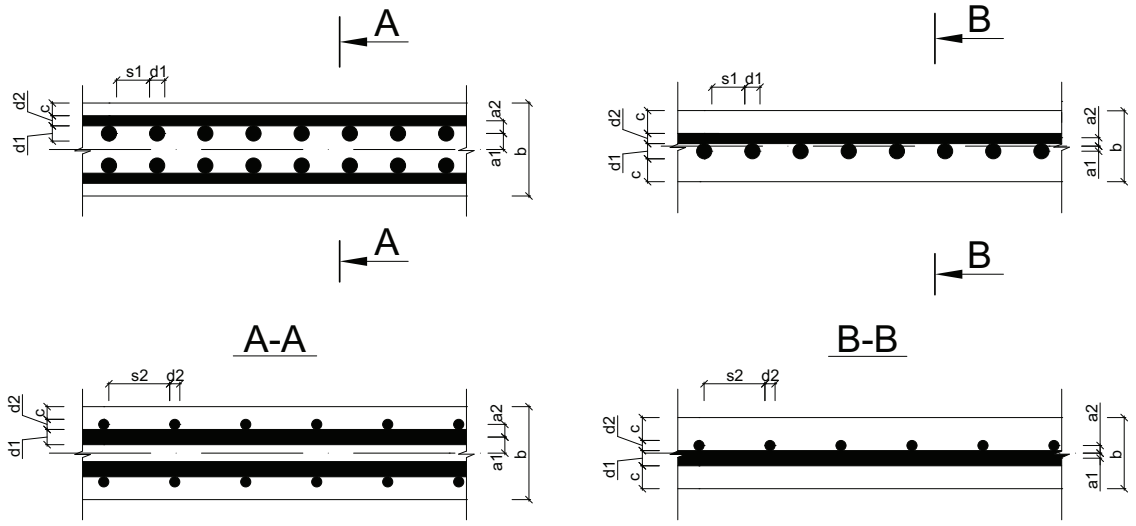

(a) Substructure 1 with two layers of rebar.

(b) Substructure 2 with single layer of rebar.

Figure 10.1: Rebar layers of the substructures.

The reinforcement parameters can be seen in Table 10.2

Table 10.2: Reinforcement geometric parameters.

	$a1$ $[mm]$	$a2$ $[mm]$	b $[mm]$	c $[mm]$	$d1$ $[mm]$	$d2$ $[mm]$	$s1$ $[^o]$	$s2$ $[^o]$
Substructure 1	14	15	110	15	18	12	1.051	1.605
Substructure 2	8	16	90	21	32	16	1.125	0.592

Having all these parameters from Table 10.2 the minimal thickness of the cross-section is found and these can be seen in Table 10.3.

Table 10.3: Cross section thickness.

Substructure 1 $[mm]$	Substructure 2 $[mm]$
100	60

10.2 Non linear analysis of the substructures

In the following a non-linear analysis will be performed for substructure 1 and 2 with the thickness as shown in Table 10.3 and with rebar arrangement as shown in Figure 10.1. For the non linear analysis Concrete Damaged plasticity is applied. The mechanical properties for the UHPC from Table 3.1. The uniaxial tensile and compressive stress-strain relationss from Table 3.4 and Table 3.2 are utilized for the material model. The option *Static - General* is applied and the *Non-linear geometry* function turned on. When the non linear analysis was performed, it didn't complete due to the error. The analysis was aborted because the matrix

material could not resist the shear forces that was concentrated, as shown in Figure 9.10 . A possible way of solving this problem is to increase the thickness at a local place where it is needed as shown in Figure 10.2. But due to limited time of project period, this was not implemented in *Abaqus*.

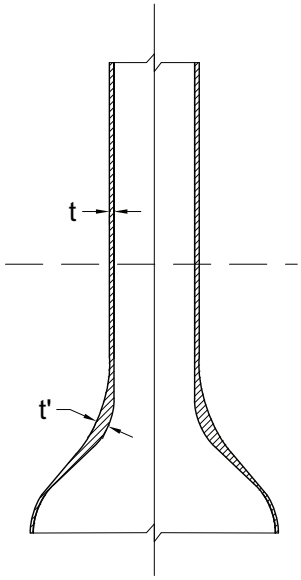

Figure 10.2: Substructure with varying thickness.

Therefore a constant thickness for the whole substructure was increased until the shear forces could be resisted by the cross section. The final result for the cross section thickness of the substructures can be seen in Table 10.4.

Table 10.4: Final cross section thickness of the substructures.

Substructure 1 $[mm]$	Substructure 2 $[mm]$
110	90

With these thickness and rebar layers, the substructures could withstand the self weight, hydraulic pressure and the wind load. In order to properly check if the rebar layers are exploited to the limit, a non-linear analysis has been performed where the wind load is increased with a factor 2. The results can be seen in Table 10.5. For the substructure 1 the analysis had stopped when 56.6 percent of the load was applied. This means that the substructure can withstand 13.2 percent additional wind load. For the substructure 2, 57.4 percent of the load was applied before the analysis stopped so the substructure 2 can withstand 14.8 percent additional wind load.

Table 10.5: Exploitation of the rebar layers.

Exploitation	
Substructure 1 [−]	Substructure 2 [−]
1.132	1.14

From this analysis it can be concluded that the exploitation of the rebar layer is acceptable.

Next the thickness and radius ratio is going to be shown for the substructure and this can be seen in Table 10.6.

Table 10.6: Thickness and radius ratio for the substructures.

Substructure 1 [–]	Substructure 2 [–]
0.012	0.01

As it can be seen from the results, if the convention should be followed that the thickess to radius ratio should be 1/200, the results are not near the convention for shell structures. The substructures are made with Compact Reinforced composite and since the equivalent homogenious thickness is not known the buckling risk will be checked.

10.3 Linearized prebuckling load of the substructures

In the following the linearized prebuckling load is going to be invistigated to check if there are any buckling risk of the substructures. The analysis has been performed for substructure 1 and 2. The linearized prebuckling eigenvalues can be seen in Table 10.7.

Table 10.7: Linearized prebuckling eigenvalues of the substructures.

	Substructure 1	Substructure 2
λ_1	6.7637	4.1456
λ_2	9.576	6.2583
λ_3	11.081	7.215
λ_4	12.135	8.691
λ_5	14.02	9.2243

As it can be seen the linearized eigenvalues are not closely spaced, this indicates that the substructures are not geometric imperfection sensitive. The substructure 2 with elastic materials, without rebar has been analysed for linearized eigenvalues, it can be seen in Table 9.4. The substructure 2 with rebar layer has been analysed for the linearized eigenvalues (Table 10.7). When comparing these two tables the values for substructure 2 with rebars is a bit higher. This is due to the contribution of the stiffness from rebar. When comparing the linearized eigenvalues for the substructure 1 and substructure 2, substructure 1 has higher linearized eigenvalues because this has a higher cross sectional thickness. The first linearized prebuckling mode for the substructures can be seen in Figure 10.3. In the compressive part of both substructures the linearized prebuckling mode appears. So when looking at the substructure the prebuckling occurs locally in the compressive part. When comparing the linearized prebuckling mode for the substructures with the dome structure, cylinder and bucket foundation in Chapter 6. These have different prebuckling modes because they have uniform pressure load at their entire surface, while the applied loads of the substructure is quite different the areas with concentrated tensile forces and compressive forces exist due to the wind load.

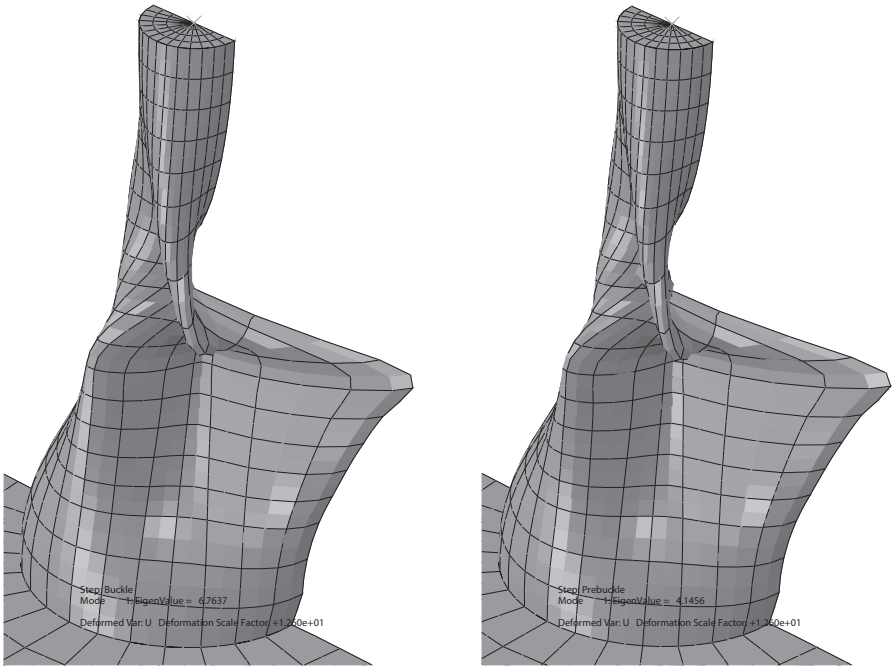

(a) Substructure 1. (b) Substructure 2.

Figure 10.3: First linearized prebuckling mode of the substructures.

10.4 Analysis of the substructures with geometrical imperfection

In the following the analysis of the substructures with geometrical imperfections will be described. Two different load case analysis has been performed and described in the following. Two different load cases can be seen in Table 10.8. This has been done to check if there are any difference. The substructure 2 has been analysed for two different load cases.

Table 10.8: Two different load cases in geometric imperfection analysis of substructures.

	Load case 1	Load case 2
Step 1	G_1	$G_1 + p_h$
Step 2	$F_w + p_h$	F_w

G_1 is defined as self weight, wind load as F_w and hydraulic pressure as p_h. By having these different load steps, different linearized eigenvalues has been found from Step 2.

Table 10.9: Multiplication of the linearized eigenvalues for different load cases.

	Load case 1	Load case 2
Step 2	$(F_w + p_h)\lambda$	$F_w\lambda$

Load case 1 is already defined in previous analysis and the result for linearized eigenvalues can be seen in Table 10.7. The linearized eigenvalues for load case 2 can be seen in Table 10.10. As it can be seen, it has a bit higher linearized eigenvalues than for load case 1. This is because only the wind load has to be multiplied with the linear eigenvalue.

Table 10.10: Linearized prebuckling eigenvalues of substructure 2 for load case 2.

	Substructure 2
λ_1	4.3937
λ_2	6.5482
λ_3	7.5404
λ_4	8.9995
λ_5	9.8973

For the non linear analysis of the substructures with geometrical imperfections *Static - Riks* is chosen as the solver. The first linearized prebuckling mode is applied as the geometrical imperfection. The maximum normalized displacement for substructure 1 is found to be $U_{max} = 1.068$ and for substructure 2 the value is found to be $U_{max} = 1.072$ for both load cases. The associated scale factor is then found by (4.6). The response of the substructures with increasing geometric imperfection can be seen in Figure 10.4. There are several things that are shown in the figure. The load proportionality factor in this case is regarded as a safety factor of the design load. It can be observed that the substructure 1 and 2 are nearly parallel when the safety factor decreases with increasing imperfection. Firstly for the load case 1, it can be seen that the substructure 1 and 2 are not sensitive for geometric imperfection, while it is for the dome. With nearly 1 m of imperfection, when 60 percent of the load is applied there is failure for substructure 1, while for substructure 2 about 45 percent. If there is no imperfection for the substructures the safety factor is about 1.17 for substructue 1 and 1.08 for substructure 2. If the safety factor is 1, the allowance of the imperfection for substructure 1 is about 0.17 m, while for substructure 2 is 0.08 m. When compared these imperfections for the dome, only 22 percent of the load can be applied.

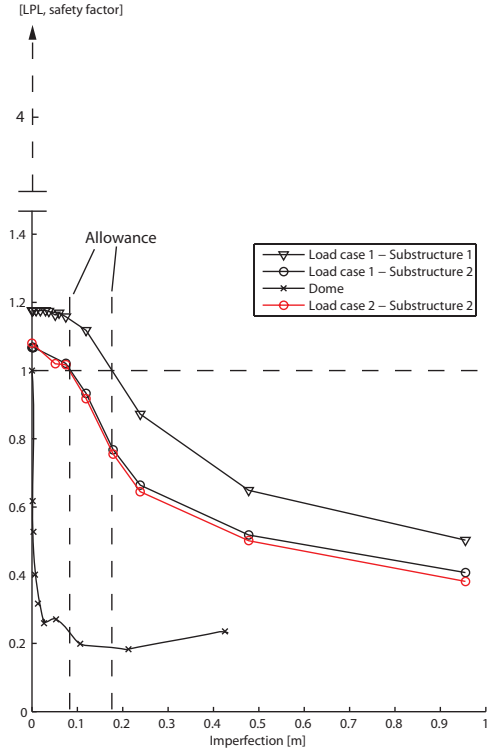

Figure 10.4: Scale factors of the loads with increasing geometrical imperfection of the structures.

For load case 2, as mentioned only substructure 2 has been checked and it can be observed that there is practically no difference between load case 1. This could be because in load case 1 the hydraulic pressure is not critical for the substructure as observed in Section 9.8. In the figure the smallest linearized eigenvalue for substructure 2 is shown and this has a value of 4.2. So when comparing buckling risk and material failure for the substructures, the material failure is the critical one and is the design crition for this case. There is two things in the response of the substructures, there is combined failure mechanism. The substructures were originally designed for collapse load for the perfect structure in a non-linear analysis, where plasticity occured and all material properties was included. The geometric imperfection was introduced based on linearized prebuckling mode, where the material was considered as an elastic. By introducing geometric imperfection, bending mechanism was introduced to the substructure where it was not designed for this case. So the load bearing capacity decreased when the geometric imperfection was introduced.

So in this project the maximum geometric imperfection that is allowed for the substructures can be seen in Table 10.11.

Table 10.11: Maximum allowed geometric imperfections for the substructures.

Substructure 1 $[m]$	Substructure 1 $[m]$
0.17	0.08

CHAPTER 11

CONCLUSION

A new concept of the offshore windturbine transition piece between bucket foundation and the tower has been proposed. Instead of using the steel a good alternative choice to replace the steel is the Compact Reinforced Composite, which has the matrix material of a ultra high performance concrete, mixed with steel fibres, closely spaced rebars and has a cover layer of only 15 mm. Since the substructure was considered as a shell structure, and there was no analytical solution for prebuckling load a verification study was performed for buckling analysis of shell structures such as the dome structure, cylinder shell and a bucket foundation. The results showed that there was a good agreement with the analytical result and FEA result. So the results from the linearized prebuckling analysis of the substructures are believed to be reliable.

Since there was no available extreme data for the determination of the wave height and wave period for the water depth of 20 m, assumed values for the wave height and wave period was applied in this project. So therefore the total horizontal forces acting on the substructure had to be calculated to check if the result was realistic. This was compared to the roughly known magnitude of the horizontal force acting on the monopile. The result showed that the total horizontal force was a bit higher due to the geometry of the substructure. But the result is acceptable.

The assumption of the drag pressure distribution around the substructure has been made. This was adjusted so the total horizontal force from the assumed drag pressure distribution was scaled by comparing with the Morison's equation. The limit of the assumed pressure distribution was, that it could not be applied when the wave surface was in the trough due to the integration limits based on the direction of the particle motion. Therefore it was assumed that the critital hydraulic pressure distribution was on the crest of the wave surface.
In Section 9.8 it was invistigated if the hydraulic pressure had a significant impact on the substructure. When the hydraulic pressure was not applied and only the wind load and self weight were applied it was discovered that the hydraulic pressure actually decreased the circumferencial section forces of about 5 percent. The explanation for this was that the drag pressure decreased the circumferential section forces in the stagnation point of the hydraulic pressure distribution combined with the constant inertia pressure as compressive pressure. In the vicinity of the stagnation point in the cylinder, meridional tensile forces act in the substructure due to the wind load. So another question arised, is the drag pressure distribution more critical if the wave surface was in the trough and combined with inertia pressure that

is constant as suction pressure? For now the question remains unanswered because due to limited time of the project period the question could not be confirmed. Since the hydraulic pressure distribution is based on linear theory, this could have been improved by applying nonlinear wave theory. But since the linear wave theory gives the basic idea of the response of the substructure from hydraulic pressure and it is simple to implement in *Abaqus*, it is assumed that this is adequate for this project.

It was assumed that the substructure could be equivalent to a axisymmetric closed tubular beam and with the given external forces such as the wind load, moment from the wind and self weight. Expected shear forces was confirmed in Section 9.9.

In the final design of two different cross sections, one with single rebar layer and one with two layers of rebar has been investigated using nonlinear analysis, where Concrete Damaged Plasticity material model for concrete and Von Mises material model for steel were applied. To check how much rebar layers were exploited for each substructure a wind load with a twice big magnitude was applied. For both substructures the results showed that around 14 percent additional wind load could be resisted.

A linearized prebuckling analysis was performed for both of the substructures and the result showed that there was no buckling risk and that linearized buckling mode was highly local due to the wind load that gave some part of the substructure a compressive force.

For the final stage of the analysis of the substructures a nonlinear analysis was performed with geometrical imperfections. The results showed that the substructures was not imperfection sensitive. This could also be seen from the linearized eigenvalues, because they were not closely spaced.

The outcome of the master's thesis based on the result of the analysis is that the Compact Reinforced Composite is a highly candidate to replace the natural choice of steel in offshore windturbine.

BIBLIOGRAPHY

[1] Abaqus Version 6.8. Abaqus analysis users manual, volume i, 2008.

[2] Abaqus Version 6.8. Abaqus analysis users manual, volume ii, 2008.

[3] Abaqus Version 6.8. Abaqus analysis users manual volume iv: Elements, 2008.

[4] Abaqus Version 6.8. Abaqus cae users manual, 2008.

[5] Abaqus Version 6.8. Abaqus keywords reference manual, volume ii:i-z, 2008.

[6] Abaqus Version 6.8. Abaqus theory manual, 2008.

[7] Abaqus Version 6.8. Getting started with abaqus interactive edition, 2008.

[8] Bent Aarup. Crc grundlæggende egenskaber. CRC Technology, 2002.

[9] Thomas Lykke Andersen and Peter Friigard. *Lecture Notes For the Course in Water Wave Mechanics*. Water and Soil Department of Civil Engineering. Aalborg University., 1 edition, 2007.

[10] Anja M. Bache. Ny betons form - for kæmper konstruktioner. Published by Arkitektskolen i Aarhus, 2004.

[11] Hans Henrik Bache. *Compact Reinforced Composite Basic Principles*. Aalborg Portland., 1987. CBL Rapport No. 41.

[12] Hans Henrik Bache. *Ny Beton - Ny Teknologi*. Aalborg Portland., 1992.

[13] Hans Henrik Bache. *Concrete and Concrete Technology in a Broad Perspective*. Aalborg Portland., 1995. CBL Reprint No. 27.

[14] Christian Leblanc Bakmar. The monopod bucket foundation. Dong Energy, 2009.

[15] H. F. Burchardt. *Strøm- og bølgekræfter på stive legemer*. Laboratoriet for Hydraulik og Havnebygning. Instituttet for Vand, Jord og Miljøteknik., 2 edition, 2002.

[16] H. F. Burcharth. *Islaster på konstruktioner*. Laboratoriet for Hydraulik og Havnebygning. Instittutet for Vand, Jord og Miljøteknik. AUC, Sohngaardsholmsvej 57, 9000 Aalborg, 4 edition, 2004.

[17] Binoy K. Chatterjee. *Theory and Design of Concrete Shells*. Chapman and Hall Ltd., 3 edition, 1988. ISBN 0 412-31660-9.

[18] Robert D. Cook, David S. Malkus, and Michael E. Plesha. *Concepts and Applications of Finite Element Analysis*. John Wiley and Sons, Inl.., 3 edition, 1989. ISBN 0-471-84788-7.

[19] Robert D. Cook, David S. Malkus, Michael E. Plesha, and Robert J. Witt. *Concepts and Applications of Finite Element Analysis*. John Wiley and Sons, Inl.., 4 edition, 2001. ISBN 978-0-471-35605-9.

[20] Mehdi Farshad. *Design and analysis of shell structures*. Kluwer Academic Publishers., 1992. ISBN 0-7923-1950-8.

[21] E. Fehling, M. Schmidt, and S. Stürwald. *Ultra High Performance Concrete (UHPC)*. University of Kassel., no. 10 edition, 2008. ISBN: 978-3-89958-376-2.

[22] M. L. Gambhir. *Design of reinforced concrete structures*. Prentice-Hall of India Private Limited., 2008. ISBN 978-81-203-3193-8.

[23] Terence S. Hedges. Effects of current on wave drag and inertia loads, 1983.

[24] M. S. Henriksen. *Højstyrke betons trækopførsel. En undersøgelse af tynde fiber- og hovedarmerede skivers trækopførsel, K9 Aalborg Universitetscenter*. Aalborg universitet., 1993.

[25] Guy T. Houlsby and Byron W. Byrne. Suction caisson foundations for offshore wind turbines and anemometer masts, 2000. Wind Engineering Volume 24 No. 4, 2000.

[26] Bjarne Chr. Jensen. *Betonkonstruktioner efter DS/EN 1992-1-1*. Nyt Teknisk Forlag, 1. edition, 2008. ISBN 978-87-571-2668-6.

[27] Kim Andre Larsen. *Static Behaviour of Bucket foundations*. Aalborg University., 2007. Ph. D. Thesis defended in 2007.

[28] Christian LeBlanc. *Design of Offshore Wind Turbine Support Structures*. Aalborg University., dce thesis no. 18 edition, 2009. Ph. D. Thesis defended in 2009.

[29] Martin Liingaard. *Dynamic Behaviour of Suction Caissons*. Aalborg University., 2006. Ph. D. Thesis defended public at Aalborg University October 19, 2006.

[30] J. Lubliner, J. Oliver, and E. Oñate. *International Journal of Solids and Structures*. Elsevier Ltd., volume 25, issue 3 edition, 1989. Pages 299-326.

[31] May Sæderup Mortensen and Hannes Árnason. *Eksperimentel og numerisk bestemmelse af egenskaber for kompositmateriale bestående af stål og højkvalitetsbeton*. ., 2008. Master Thesis in Civil Engineering.

[32] M. P. Nielsen and L. Pilegaard Hansen. *Spændinger og deformationer i rumbjælker*. Den private Ingeniørfond ved Danmarks tekniske Højskole., 1978. ISBN: 87-87245-62-0.

[33] Niels Saabye Ottosen and Matti Ristinmaa. *The Mechanics of Constitutive Modeling*. Elsevier Science., 2005. ISBN 13:9780080446066.

[34] Rodney Pinna and Beverley F. Ronalds. Hydrostatic buckling of shells with various boundary conditions, 1999.

[35] Turgut Sarpkaya and Michael Isaacson. *Mechanics of Wave Forces on Offshore Structures*. Van Nostrand Reinhold Company., 1 edition, 1981. ISBN-13: 978-0442254025.

[36] Sven Thelandersson. *Analysis of thin-walled elastic beams*. Lund University., 1987.

[37] M.S. Williams and J.D. Todd. *Structures theory and analysis*. Palgrave Macmillan. ISBN 0-333-67760-9.

APPENDIX A

COORDINATE SYSTEMS

In the following cylindrical and spherical coordinate systems are going to be described.

Cylindrical Coordinate System

The idea of cylindrical coordinate system is to describe point A(r,θ,z) where r describes the distance from the z-axis to the point A in plane zx; θ - is the azimuth angle from the positive xz-plane to the point; z - is the same as in cartesian coordinate system.

The cylindrical coordinate system is a simplified expression of different paramerters in cartesian coordinate system, such as:

$$r = \sqrt{x^2 + y^2} \tag{A.1}$$

$$x = rcos(\theta) \tag{A.2}$$

$$y = rsin(\theta) \tag{A.3}$$

$$z = z \tag{A.4}$$

$$tan(\theta) = \frac{y}{z} \tag{A.5}$$

Definition of the cylindrical coordinate system over the cartesian is shown in Figure A.1.

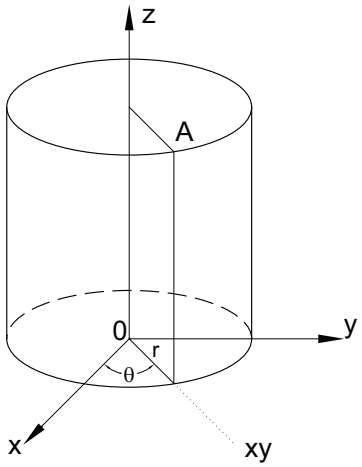

Figure A.1: Cylindrical coordinate system.

In Abaqus software the definition of the coordinate system is the same as it is shown in Figure A.1 where x correspond to R, Y to T and Z to Z.

Spherical Coordinate System

The base idea of spherical coordinate system is to describe a point A (r,θ,ϕ) where r describes the distance from the z-axis to the point A in plane xy; θ - is the azimuth angle from the positive xz-plane to the point; ϕ - is the zenith angle from z axis to the line joining orign 0 to the point A.

The sperical coordinate system is a simplified expression of different paramerters in cartesian coordinate system, such as:

$$r = \sqrt{x^2 + y^2 + z^2} \tag{A.6}$$

$$x = rsin(\phi)cos(\theta) \tag{A.7}$$

$$y = rsin(\phi)sin(\theta) \tag{A.8}$$

$$z = rcos(\theta) \tag{A.9}$$

$$tan(\phi) = \frac{\sqrt{x^2 + y^2}}{z} \tag{A.10}$$

$$tan(\theta) = \frac{y}{z} \tag{A.11}$$

Definition of the spherical coordinate system over the cartesian is shown in Figure A.2.

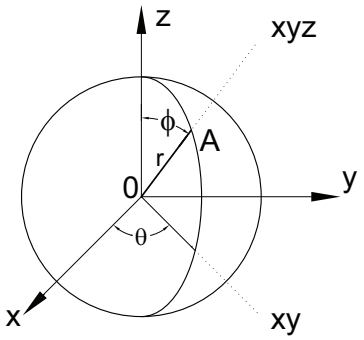

Figure A.2: Spherical coordinate system.

In Abaqus software the definition of the coordinate system is the same as it is shown in Figure A.1 where x correspond to R, Y to T and Z to P.

APPENDIX B

ENCLOSED CD

A pdf-file of the master's thesis can be found in the enclosed CD.

Programs

1. Bucket Foundation A - Abaqus *.cae file for the Bucket Foundation A.
2. Bucket Foundation B - Abaqus *.cae file for the Bucket Foundation B.
3. Cylinder A - Abaqus *.cae file for the Cylinder A.
4. Cylinder B - Abaqus *.cae file for the Cylinder B.
5. Dome 4 - Abaqus *.cae file for the Dome 4.
6. Substructure 1 - Abaqus *.cae file for the Substructure 1.
7. Substructure 2 - Abaqus *.cae file for the Substructure 2.